

**Charles University in Prague
Faculty of Science
Department of Physical and Macromolecular Chemistry**

PhD THESIS



**Composite Systems of π -conjugated Polymers
with Plasmonic Metal Nanoparticles:
Preparation, Morphology and Optical
Properties**

RNDr. Ondřej Dammer

Supervisor: RNDr. Jiří Pflieger, CSc.

Consultant: Prof. RNDr. Blanka Vlčková, CSc.

Prague 2009

Author's statement

This work was elaborated at the Institute of Macromolecular Chemistry, Academy of Sciences of the Czech Republic and at the Department of Physical and Macromolecular Chemistry, Charles University in Prague under the guidance of RNDr. Jiří Pflieger, CSc. and Prof. RNDr. Blanka Vlčková, CSc.

I guarantee that the work is original and only the literature listed in references was used. The results presented in this Thesis have not been used in the submission for the same or for another research degree.

Prague,

.....

Ondřej Dammer

Coauthors' statement

I declare that Mgr. Ondřej Dammer has substantially contributed to all six papers based on this thesis and published till now. He is the first author for most of the listed publications with his major input. He has completed most of the experiments by himself and participated in the experiment planning, interpretation of data and writing the publications.

Prague,

.....

RNDr. Jiří Pflieger, CSc.

1.	INTRODUCTION.....	1
1.1.	Noble metal nanoparticles.....	1
1.1.1.	Synthesis and fabrication of plasmonic nanostructures.....	7
1.1.2.	Morphologies of metal NPs and their assemblies.....	10
1.2.	Polymer-nanoparticle composites.....	11
1.2.1.	π -conjugates polymers.....	12
1.2.2.	Preparation of nanocomposites of CPs and noble metal NPs.....	13
1.2.3.	Morphology and optical properties of CPs nanocomposites with noble metal NPs.....	17
1.2.4.	Electronic properties of CPs nanocomposites with noble metal NPs.....	19
1.2.5.	Photophysical processes on metal NP surface.....	22
1.2.5.1.	Surface-enhanced Raman scattering.....	22
1.2.5.1.1.	Electromagnetic mechanism of SERS.....	23
1.2.5.1.2.	Mechanisms of molecular resonance.....	24
1.2.5.1.3.	SERS of π -conjugated polymers.....	24
1.2.5.2.	Fluorescence.....	25
1.2.5.2.1.	Surface-enhanced fluorescence.....	25
1.2.5.2.2.	Fluorescence quenching.....	26
2.	OBJECTIVES.....	30
3.	EXPERIMENTAL.....	31
3.1.	List of chemicals.....	31
3.2.	Preparation procedures used for respective chapters.....	32
3.3.	Instrumentation and preparation of samples for the measurements.....	35
4.	RESULTS AND DISCUSSION.....	41
4.1.	Interaction of high-power laser pulses with monodisperse Au NPs of various sizes.....	41
4.1.1.	Parent Au hydrosols.....	41
4.1.2.	Effect of laser fluence on fragmentation of Au NPs of various sizes.....	42

4.1.3.	Effect of initial Au NPs sizes on their fragmentation with laser pulses of normalized fluences.....	45
4.1.4.	The effect of laser pulse wavelength on fragmentation of Au NPs of various sizes.....	47
4.1.5.	Discussion of Au NPs fragmentation mechanisms.....	53
4.1.6.	Conclusions.....	54
4.2.	Morphology and optical responses of SERS active π-conjugated poly(N-ethyl-2-ethynylpyridinium iodide)/Ag nanocomposite systems.....	55
4.2.1.	SPE spectra of Ag/PEEP-I hydrosol systems with various polymer concentration.....	55
4.2.2.	TEM imaging of Ag/PEEP-I hydrosol systems and determination of fractal dimension (<i>D</i>).....	58
4.2.3.	Summary of results of the SPE probing and TEM imaging of the Ag/PEEP-I hydrosol systems.....	61
4.2.4.	Raman spectra of Ag/PEEP-I nanocomposite systems.....	62
4.2.5.	Fluorescence spectra of Ag/PEEP-I nanocomposite systems.....	65
4.2.6.	Conclusions.....	69
4.3.	Polymer composites consisting of regioregular poly(3-octylthiophene-2,5-diyl) and plasmonic metal nanoparticles.....	70
4.3.1.	Metal organosols-precursors for composite type M	71
4.3.1.1.	Au organosols.....	71
4.3.1.2.	Ag organosols.....	73
4.3.2.	Characterization of Au/P3OT composites.....	76
4.3.2.1.	UV- Vis spectroscopy.....	76
4.3.2.2.	Transmission electron microscopy (TEM)	77
4.3.2.3.	Dynamic light scattering (DLS)	81
4.3.3.	Characterization of Ag/P3OT composites.....	82
4.3.3.1.	UV-Vis spectroscopy.....	82
4.3.3.2.	Transmission electron microscopy (TEM)	85
4.3.3.3.	Dynamic light scattering (DLS)	90
4.3.4.	Raman spectroscopy.....	91
4.3.4.1.	SERS spectra of Au/P3OT composites.....	91
4.3.4.2.	SERS spectra of Ag/P3OT composites.....	94
4.3.5.	Conclusions.....	101

4.4. Polymer composites containing Au nanoparticles and poly[2-methoxy-5-(2-ethylhexyloxy)-1,4-phenylenevinylene].....	103
4.4.1. Morphologies of Au nanoparticles in organosol and composites with MEH-PPV.....	103
4.4.1.1. Parent Au organosol.....	103
4.4.1.2. Nanocomposites type M	104
4.4.1.3. Nanocomposites type R	105
4.4.2. UV-Vis spectra of Au/MEH-PPV nanocomposites.....	107
4.4.3. Stability of MEH-PPV in reference systems.....	109
4.4.3.1. Stability of MEH-PPV after addition of NaBH ₄	109
4.4.3.2. UV-Vis spectral study of reaction of MEH-PPV with the AuCl ₄ ⁻ /TOAB complex.....	109
4.4.3.3. Cyclic voltammetry.....	111
4.4.3.4. Relation between molecular weight and UV-Vis spectra of MEH-PPV during reaction with AuCl ₄ ⁻ /TOAB complex...	113
4.4.4. Molecular spectra of MEH-PPV and its composites.....	114
4.4.4.1. FT-IR spectra.....	114
4.4.4.2. Raman and fluorescence spectra.....	116
4.4.5. Size-exclusion chromatography (SEC) analyses of dissolved Au/MEH-PPV nanocomposites.....	118
4.4.6. Mechanism of assembling Au NPs in MEH-PPV matrix.....	121
4.4.6.1. Assembling of Au NPs in nanocomposites M	121
4.4.6.2. Discussion of Au NPs aggregates formation in nanocomposites R	121
4.4.7. Conclusions – Comparison of nanoparticle morphology and optical properties of Au/MEH-PPV and Au/P3OT nanocomposites.....	123
5. CONCLUSIONS.....	125
6. ABBREVIATIONS.....	128
7. REFERENCES.....	130
8. PUBLICATIONS.....	137

1. INTRODUCTION

1.1. Noble metal nanoparticles

Nanosized metal particles have gained recently a considerable attention due to their unique optical and electrical properties. They show increased photocatalytic and photophysical activities which are strongly dependent on the size and shape of the particles as well as on their arrangement and mutual interaction in the particle assemblies¹⁻⁵. Such nanoparticles have shown recently use in surface-enhanced (Raman) spectroscopy, catalysis and as biological probes for diagnostic purposes, and they have many other potential applications in electronics and optoelectronics. Nanoparticle size, generally, provides an important control over many of the physical and chemical properties of nanoscale materials including luminescence, conductivity, and catalytic activity.

The unique optical responses of plasmonic metal nanoparticles (NPs) arise from an electrodynamic phenomenon known as surface plasmon. This is connected to the collective oscillations of free electrons in response to a characteristic electromagnetic frequency. Two types of surface plasmons were described^{6, 7}: (i) “propagating” surface plasmon polaritons (SPPs), which propagate tens to hundreds of micrometers along the metal surface, with an associated electric field that decays exponentially with the distance from the exposed metal surface and (ii) “nonpropagating” localized surface plasmon resonances (LSPRs), which are plasmon excitations that can be resonantly excited with electromagnetic irradiation. The coupling of metal NPs with light is accompanied by the local electromagnetic field enhancement which the surface-enhanced phenomena are based on (Chapter 1.2.6.). The growing field of scientific research and applications focused on such light-metal interactions is known as „plasmonics“.

The simplest type of LSPRs is a dipolar LSPR which can be described as follows: when a small metal nanoparticle with the radius R , much smaller than the incident radiation wavelength, is irradiated by an electromagnetic wave of a particular wavelength, the irradiation induces a collective oscillation of free electrons inside the particle, which move with the same frequency as the frequency of the incident wave. It leads to a formation of an induced dipole on the nanoparticle surface (Figure 1-1). Depending on the magnitude of the induced dipole

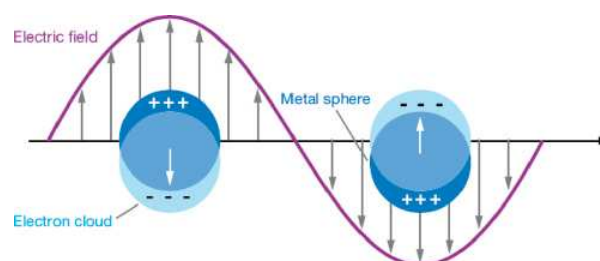


Figure 1-1. Schematic illustration of a localized surface plasmon in a metal sphere, from ref.⁸.

moment and the size of the nanoparticle a resonance oscillation can occur at a specific frequency. The dipolar plasmon resonance of the metal nanoparticle is defined by its induced dipole moment, P , which can be expressed:

$$P = 4\pi\epsilon_0 R^3 \left| \frac{\epsilon(\lambda) - \epsilon_{med}}{\epsilon(\lambda) + 2\epsilon_{med}} \right| E_0 \quad (1)$$

where E_0 is the amplitude of the electric field vector of the incident electromagnetic radiation, R nanoparticle radius, ϵ_0 the vacuum electric permittivity, ϵ_{med} the relative permittivity (dielectric constant) of the local medium; since the nanoparticles are usually embedded in a medium with negligible optical absorption in the visible region, ϵ_{med} is taken as wavelength independent), $\epsilon(\lambda)$ is the relative complex permittivity (dielectric function) of the metal which is wavelength-dependent:

$$\epsilon(\lambda) = \epsilon_r(\lambda) + i\epsilon_i(\lambda) \quad (2)$$

The complex permittivity is bound to the complex refractive index N by a simple relation:

$$\epsilon(\lambda) = N^2(\lambda), \quad (3)$$

where

$$N = n + ik \quad (4)$$

with refractive index n and absorption coefficient k .

The resonance condition, when a maximum of induced dipole moment appears, is fulfilled when

$$\left| \epsilon(\lambda) + 2\epsilon_{med} \right| = 0 \quad (5)$$

that can be achieved when

$$\epsilon_r(\lambda) = -2 \epsilon_{med} \quad (6)$$

and, simultaneously, $\epsilon_i(\lambda)$ is negligible. For an assembly of small, non-interacting Au NPs embedded in water, the wavelength at which the resonance condition is fulfilled is at 520 nm. The resonance wavelength for small non-interacting Ag NPs in aqueous environment is at 390 nm. The plasmonic response is directly measurable by optical extinction as a function of λ , providing a surface plasmon extinction (SPE) spectrum. Extinction includes both absorption and scattering contributions, which have different scaling relationships with the nanoparticle size. The absorption cross section increases linearly with particle volume, whereas the scattering cross section is relatively smaller but scales with volume squared. The characteristics of SPE spectrum such as the bandwidth, position and intensity of the SPE band depend on the nanoparticle material, NP size and shape (geometry), dielectric constant of the surrounding medium and interparticle coupling. The following examples from recent literature will clearly show how the SPE features are influenced by nanoparticle material, size, shape, dielectric constant of medium and interaction between the particles.

Nanoparticle material. Extinction spectra of spherical particles having the diameter 10 nm both in water as a surrounding medium and in vacuum were calculated by Creighton⁹ for 52 different metallic elements. Well resolved extinction bands are observed for colloidal Sc, Ti, V, Y, Cd, Eu, Yb, Hg and Th as well as for colloids of Cu, Ag, Au and the s-block metals. For most of the remaining metals, consisting of most of the metals of the d- and p-blocks, the spectra show a steep rise in extinction at very short wavelengths while in the visible range the extinction is flat and featureless. Therefore, the colloids of most of the d- and p-block metals are grey or brown. Only for Au and Ag the main extinction bands can be interpreted as plasma resonances, whilst for colloids of the other d-block metals the plasmon resonance lies in the UV region, predominantly overlapped by the interband optical transitions. It is thus evident that the Au, Ag or Cu nanoparticle colloids are good candidates for the observation of a surface-enhanced Raman scattering and other photophysical processes occurring on the nanoparticle surface since their extinction bands are close to the wavelengths of conventional laser excitation sources.

Nanoparticle size. For gold particles with $2R < 25$ nm, the size dependence of the plasmon extinction is introduced by assuming a size-dependent material dielectric function $\epsilon(\omega, R)$; for larger NPs (beyond the Rayleigh approximation) the extinction coefficient explicitly depends on the nanoparticle size as the higher-order plasmon modes contribute, which are function of R .

Plasmon bandwidth as well as SPE maximum depends on the nanoparticle size (Figure 1-2). The broadening of the SPE band for Ag and Au NPs becomes evident for nanoparticle size much less than the electron mean free path L_e , a material dependent property that, for example, gives the broadening of SPE band of Au NPs for $2R < 25$ nm. It is caused by the relaxation rate of electron displacement which increases with a $1/R$ relationship due to the scattering processes on the NP's surface. On the other hand, the position of SPE maximum for these small NPs is not significantly influenced by nanoparticle size (e.g. SPE maximum for Au NPs of $2R = 25$ -10 nm is located at 520 nm). For larger metallic NPs ($2D > 30$ nm) the SPE band, attributed to dipolar resonance, red shifts and broadens. The red shift arises from a reduction of the depolarization field caused by the retardation effect of conduction electrons that do not move all in phase. Radiative damping and also nonradiative electronic mechanism such as interband transitions contribute to the plasmon relaxation. It results in a significant broadening of the SPE band. The broadening is also caused by the excitation of higher-order plasmon modes; for example, quadrupole resonance in Ag and Au NPs can be observed in SPE spectra of particles having 60 nm in diameter.

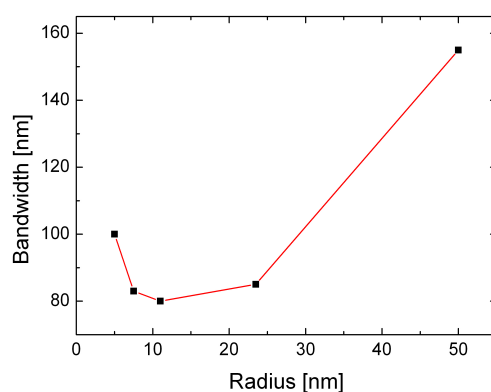


Figure 1-2. Size effect of spherical Au NPs on the SPE bandwidth, from ref.¹⁰.

Nanoparticle shape. Mie theory¹¹, the formulations of which are based on the Maxwell's equations, provides the exact analytical solution for the optical properties of spherical metallic nanoparticles and the obtained SPE spectra are in an excellent agreement with experiments as long as the examined colloids are spherical in shape, dilute in a surrounding medium, and relatively monodisperse. However, current research is focused on the fabrication of anisotropic NPs with well-defined structures other than spheres¹². These include nanoscale rods, disks, triangular prisms, multipods, cubes, and nanoshells. To obtain an analytical solution for the optical characteristics of these anisotropic structures, an electrostatic approximation must be used. A number of theoretical descriptions have been developed based on various approaches, including the discrete dipole approximation (DDA),

T-matrix method, finite difference time domain methods (FDTD), the multiple multipole method or the modified long wavelength approximation (MLWA)^{4, 13-16}.

SPE spectra of metallic nanorods will be discussed in more details. According to Mie-Gans theory (developed for particles much smaller than the wavelength of incident irradiation in which only dipolar excitations occur), the extinction $E(\lambda)$ of a spheroid metallic NP is given by the following equation

$$E(\lambda) \propto \left[\frac{\epsilon_i}{(\epsilon_r + \chi\epsilon_{med})^2 + \epsilon_i^2} \right] \quad (7)$$

where χ is a spheroid geometry dependent factor, proportional to the ratio of major (b) and minor (a) axis of the spheroid, i.e. to its aspect ratio. The resonance condition ($\epsilon_r(\omega) = -\chi\epsilon_{med}$) is similar to that for spheres except that 2 is replaced by the factor χ . It is clearly seen that the aspect ratio strongly influences the plasmon resonance of metallic nanorods which splits into two peaks due to the unevenly distributed SPs around the spheroid axis. The first peak originates in transverse mode and corresponds to the polarization perpendicular to the long axis. The second band corresponds to the longitudinal mode with the polarization parallel to the long axis. It is strongly red-shifted. As the aspect ratio of a nanorod increases, the separation between two plasmon bands becomes more pronounced (Figure 1-3).

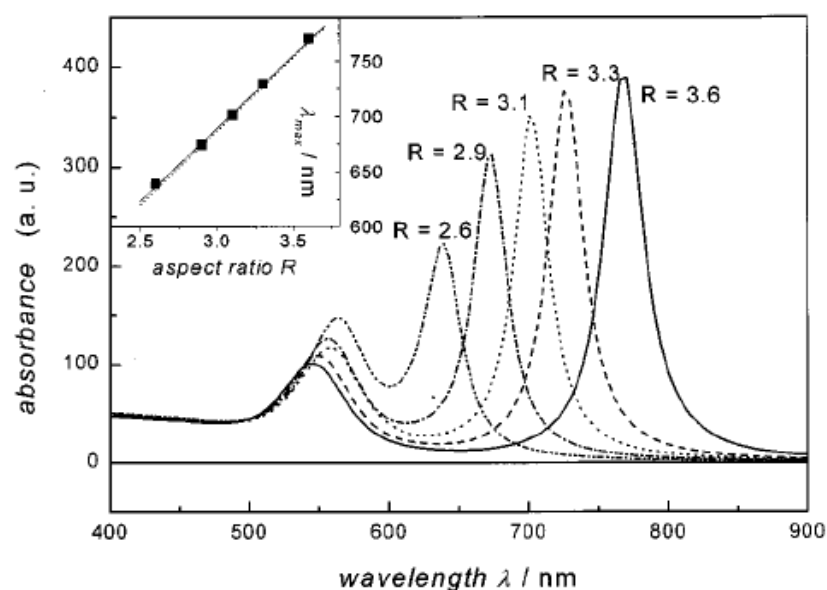


Figure 1-3. Calculated absorption spectra of Au elongated spheroids (nanorods) with varying aspect ratio, from ref.¹⁷.

Dielectric constant. The dependence of the plasmon resonance frequency on dielectric constant of the non-absorbing medium, which is related to its refractive index ($n = (\epsilon_m)^{1/2}$), arises from the resonance condition (5). In the work of Kamat et al.¹⁸ the effect of solvent refractive index on the SPE spectra of Au NPs capped with tetraoctylammonium bromide was investigated. Table 1-1 taken from this work shows the position of SPE maximum of Au NPs in solvents of various refractive indices. The position of SPE maximum was influenced by the refractive index of medium in the case of solvents with no active functional groups with affinity toward NPs (such as cyclohexane, toluene, *o*-xylene, chlorobenzene, and *o*-dichlorobenzene). In these solvents, the SPE maximum gradually shifts toward longer wavelengths with increasing refractive index of the solvent. In contrast, no shift of SPE maxima was observed for polar solvents such as THF, DMF, DMSO, and acetone. It was assigned to a complexation of these polar solvents with the Au NP surface which may override the effects of refractive index since it substantially alters the electron density of the Au NP.

Solvent	refractive index (n)	λ_{\max} [nm]
acetone	1.3590	521
tetrahydrofuran	1.4070	521
cyclohexane	1.4266	526
DMF	1.4310	522
DMSO	1.4758	521
toluene	1.4961	530
<i>o</i> -xylene	1.5016	532
chlorobenzene	1.5240	533
<i>o</i> -dichlorobenzene	1.5509	535

Table 1-1. The position of SPE maximum of Au NPs in solvents of varying refractive indices, from ref.¹⁸.

Interparticle coupling. Mie theory only applies to non-interacting well separated NPs. However, new interesting optical properties were observed for assemblies of interacting particles. Recent progress has been made in fabrication of ordered arrays of interacting NPs¹⁹⁻²¹, and in the calculation of SPE spectra of these assemblies^{22, 23}. In such cases, each NP with a diameter much smaller than the wavelength of exciting light acts as an electric dipole. Two types of electromagnetic interaction between the NPs were considered in the literature⁶, depending on the spacing d between adjacent NPs: (i) near-field coupling with a distance dependence of d^{-3} and (ii) far-field dipolar interactions with the d^{-1} distance dependence. Far-field dipolar interactions dominate at interparticle spacing of the order of the wavelength (λ)

of the exciting light, while near-field dipolar interactions dominate for the spacing much smaller than λ . Electromagnetic coupling plays a key role in the plasmonic properties of NP assemblies, and can enhance their optical responses by many orders of magnitude. For example, many of the early SERS observations were performed on fractal nanoparticle aggregates containing “hot spots” which were found to produce a great enhancement of Raman scattering signal^{24, 25}. Experimental and calculated SPE spectra of fractal aggregates from ref.²⁶ are shown in Figure 1-4.

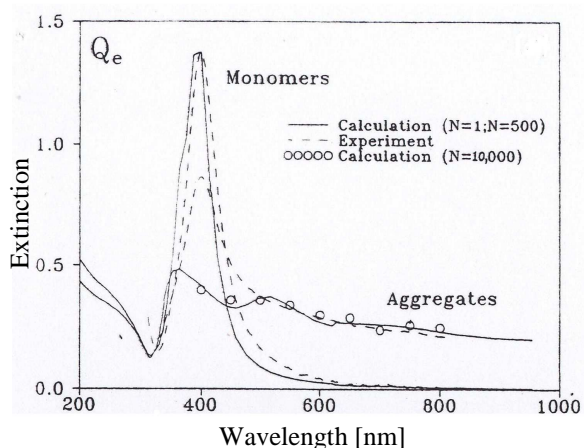


Figure 1-4. Experimental and calculated SPE spectra for fractal aggregates containing 500 and 10000 NPs.

1.1.1. Synthesis and fabrication of plasmonic nanostructures

Nanostructures are typically formed using either lithographic techniques²⁰ or solution-phase synthesis. Lithography is used for fabrication of reproducible substrates with tunable optical properties for SERS studies and plasmon-enhanced fluorescence²⁷. Solution phase synthesis is a versatile approach to the preparation of metal NPs that allows to control their size, shape, composition and structure (e.g. solid or shell-like). This approach generally involves the reduction of metal salts (Ag NO₃, HAuCl₄.3H₂O) with chemical reductants such as citrate²⁸, hydride²⁹ (NaBH₄), alcohols³⁰, hydroxylamine³¹ or hydrazine³². The reduction can be also carried out electrochemically^{33, 34}, photochemically^{35, 36} or sonochemically^{37, 38}. Addition of an appropriate stabilizer to the solution of metal salt in the course of the reduction allows to control the NP growth and to suppress the aggregation of NPs. The stabilizer^{39, 40} – commonly ligands, surfactants, ions, organic acids, or polymers having an affinity to the metal surface – adsorbs or coordinates to the nanoparticle surface and inhibits the aggregation by Coulombic repulsion and/or steric hindrance. The specific choice of the reductant, stabilizer, temperature of the reaction mixture, and concentration of the reagents can affect the size and shape of the resulting NPs. Solution-phase synthesis mostly yield approximately spherical NPs since the spherical shape possesses the lowest surface energy. In fact, these particles have crystallographic facets and their real shapes are higher polyhedrons such as

icosahedrons or dodecahedrons. In this work they will be referred to as spherical particles for simplicity.

Well established method of synthesis of Au NPs is a reduction of HAuCl_4 with sodium citrate in an aqueous environment, which was introduced by Turkevitch²⁸ in 1951. The citrate ions act as both a reducing agent and an electrostatic stabilizer. Citrate salts can be also employed for the preparation of Ag NPs.

Another widely adopted solution-phase synthesis of Au NPs is a Brust-Schiffrin method⁴¹, published in 1994. This method has had a considerable impact on nanotechnology in the last decade, because it allowed the facile synthesis of stable Au NPs with controlled size (diameter ranging between 1.5 and 5.2 nm). Indeed, these Au NPs can be repeatedly isolated and redissolved in common organic solvents without irreversible aggregation, and they can be easily handled and functionalized by many molecular compounds. This method is based on a two-phase reaction system (containing an aqueous and organic phase) with tetraoctylammonium bromide as a phase-transfer agent. Phase-transferred Au ions are reduced with NaBH_4 in the presence of alkanethiols or other ligands such as amines and phosphines to stabilize and control the nanoparticle size. Recently published single-phase adaptations of the Brust method have eliminated the need of the phase-transfer agent⁴².

Well-defined NPs can be fabricated by seed-mediated growth techniques^{37, 43, 44}. In seed-mediated syntheses the „seeds“, playing the role of the nucleating agent, are added into a metal salt solution. The metal salt is reduced directly on the surface of the seeds with a minimal concurrent nucleation in the solution. The size, morphology, and aspect ratio of the resulted metal NPs are controlled by the composition and concentration of the seeds, metal salts, reducing agents and by various additives (e.g., cetyl-trimethylammonium bromide) which are present in the solution^{31, 45}.

Another versatile method of the metal nanoparticle preparation is a laser ablation of a metal target in liquid ambient which was firstly introduced by Henglein et al.⁴⁶ in 1993. The intensive laser irradiation induced a size reduction of growing NPs simultaneously with the process of laser ablation⁴⁷. Recently, the interaction of pulsed laser light with chemically prepared metal NPs has become a subject of focused research interest⁴⁸⁻⁵⁴. The intense laser light can induce size reduction^{48-51, 55}, size enlargement^{52, 56}, and morphological changes (reshaping) of NPs^{52, 53, 57, 58}. The parameters of the laser pulses, including laser pulse duration, wavelength, energy per pulse and beam focusation, as well as the chemical parameters such as the presence of chemical species in the liquid medium^{59, 60} in course of the laser radiation influence the size and morphology of the resulting NPs. A detailed analysis of

the laser-induced shape transformation and size reduction of Au NPs has been carried out^{51, 53, 61}. The changes in NP shape and size were considered to occur through melting and vaporization of Au NPs upon laser pulse impact. The estimated temperature of Au NPs after a nanosecond single-shot impact exceeds the boiling point of gold and suggests that the size-reduction is a photothermal process⁴⁸. Another mechanism of laser-induced size reduction suggested by Kamat et al.⁴⁹ is based on a Coulomb explosion induced by an electron ejection from particles upon illumination. The repulsion between the charges then leads to their fragmentation. In previous studies of Link et al.^{53, 57, 61} a laser-induced transformation of Au nanorods into spherical particles in a colloidal solution was investigated using both femtosecond (fs) and nanosecond (ns) laser pulses of 800 nm wavelength at various pulse energy. Since the laser light of the used wavelength selectively excites the SP longitudinal mode in Au nanorods, the nanoparticles undergo structural changes. At low pulse energies, melting of Au nanorods occurred instead of the fragmentation. However, the energy threshold for melting induced by fs laser pulses was on the order of 100 times lower when compared with ns pulses. It can be explained by the huge difference in the peak power delivered by fs and ns pulses and by the fact that, in the case of fs laser pulses, the absorption of photons by electrons, electron-phonon relaxation (heating of the lattice < 10 ps), melting (30 – 35 ps) and phonon-phonon relaxation (cooling of the lattice > 100 ps) are well separated in the time scale. On the other hand, phonon-phonon relaxation can effectively compete with the rate of photon absorption within the nanosecond pulse duration. Thus, laser-induced melting was more efficient in inducing a complete shape transformation of Au nanorods with femtosecond laser pulses (100 fs) than with the longer nanosecond pulses (7 ns) at the same pulse energy. At high fs pulse energies, nanoparticle fragmentation took place through multiphoton ionization of the Au nanorods (the repulsion of the accumulated positive charges on the particles leads to the fragmentation shortly after or even during the laser pulse). Au nanorods were fragmented by ns laser pulses of high energy because of the absorption of additional photons by the hot lattice.

Laser ablation and nanoparticle fragmentation appear to be a promising tool for obtaining NPs of desired size distribution which provide the largest LSPR in their functional assemblies, e.g. dimers can be prepared by this method. One of the fields of plasmonics which could immediately benefit from these targeted preparations is SERS spectroscopy.

1.1.2. Morphologies of metal NPs and their assemblies

Transmission electron microscopy (TEM) is the most common technique for observation of morphology of metal NPs because of their high electron density. From the morphological point of view, the following types of the NPs arrangement can be recognized in TEM images:

- I. *non-interacting NPs* – are isolated from each other due to the presence of stabilizer molecules on NP surface.
- II. *interacting NPs* – are closely packed, and can form 1-, 2- or 3-dimensional space arrangements. Regularly (hexagonally) packed NP array can be given as an example of 2-D space arrangement of NPs.

One of the most important characteristics of objects such as metal colloidal assemblies is their fractal (Hausdorff) dimension. Fractal dimension can be determined from the TEM images using the mass-radius relation:

$$M(R) \approx R^D \quad (8)$$

where D is the fractal dimension and M is the mass of the object of size R . For the determination of the fractal dimension of NPs assemblies from TEM images (Figure 1-5) it is important that the collapse of the originally 3-D colloidal aggregates into 2-D object on microscopic grid does not affect the value of their fractal dimension D assumed that $D < 2$ as it was theoretically postulated and proved experimentally²⁵. According to the fractal theory of aggregation, we can predict the type of aggregation from the values of the fractal dimension of aggregated colloids:

$D = 1.75$ and $D = 2.08$ were calculated for a diffusion-limited and reaction-limited cluster-cluster aggregation in 3-D space

without rearrangement, respectively, and the value 2.4 for a reaction-limited cluster-cluster aggregation with a subsequent rearrangement. For the 2-D cluster-cluster aggregation the value $D = 1.42$ was obtained⁶².

- III. *interpenetrating (intergrowing and/or sintered) NPs* – are arranged in distance in which the diffusion of metal atoms occurs. It may be caused by a disturbance of the

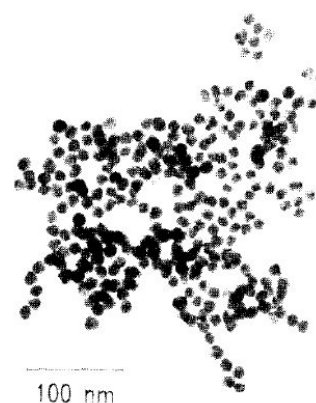


Figure 1-5. TEM image of monomer-aggregated Au nanoparticle fractal aggregate from ref.²⁵.

stabilizing electrostatic double-layer on the NP surface, e.g. by addition of chloride ions of a proper concentration⁶³. Ag NP sintering, induced growth and interpenetration induced by adsorption of small ions and its implications for the formation of surface-adsorbate complexes as well as for large SERRS enhancement of biologically important chromophoric molecules has been reported^{63, 64}.

1.2. Polymer-nanoparticle composites

Polymer composites containing metal nanoparticles have gained increasing attention for emerging applications as sensors, energy storage devices and in biomedical imaging as well as catalysis in biotechnology and microelectronics⁶⁵⁻⁶⁷. Embedding inorganic NPs into polymer matrices provides means for introducing a variety of properties to the polymer-based materials, including the mechanical, thermal and electroactive properties⁶⁸. Nanoparticle “fillers” such as clay are known to bring significant improvement in thermal and mechanical properties of polymer materials⁶⁹. They exhibit improvements in tensile strength, modulus, barrier to permeation of small molecules and fire retardation. In order to predict properties of composites, the understanding how the chemistry and morphology of the polymer matrix synergize with the surface chemistry, size and shape of a nanoscale filler is necessary⁶⁸.

Another class of nanoparticle-polymer composites is based on magnetic particles such as Fe, Co and iron oxide. Many composites have been investigated which combine different polymers and magnetic nanoparticle colloids⁶⁵. However, the preparation of materials possessing high magnetic moments and susceptibilities comparable to inorganic materials remains a challenge.

Carbon nanotubes can also be integrated into composites with polymers⁶⁶. The utility of carbon nanotubes in a wide range of applications relies on one or more of their unique fundamental properties including a high aspect ratio, high mechanical strength, excellent thermal conductivity, and the ability to conduct electrons as a semiconductor or a metal. The lack of solubility poses a significant impediment to their exploitation in many potential commercial applications. Therefore, the chemistry of carbon nanotubes has become an area of intense research since chemical derivatization is the only way how to modify properties of these materials.

The extensive range of unique size-dependent optoelectronic properties inherent to noble metal NPs makes them very attractive candidates for the integration into composites with π -conjugated polymers. In such nanocomposites (NCs), the interaction of delocalized

π -electron states of polymer chain with LSPR is expected. It can be assumed that π - π^* absorption band of the polymer will be, at least to some extent, affected by an interaction with plasmonic metal NPs and, at the same time, the optical properties of the metal NPs will be affected by the presence of the conjugated polymer. It can be expected that the key role will be played by the actual morphological characteristics of the NCs. Understanding and tuning such effects, which have become a subject of debate recently, could lead to hybrid optical devices with improved optical properties. Embedding metal NPs into host polymers provides a means for introducing a variety of new properties to composite materials, including increase in conductivity, fluorescence quenching, and catalytic activity. The possible use of such nanocomposites of metal NPs and π -conjugated polymers in optoelectronic devices such as solar cells, light emitting diodes, sensors, electronic memories, etc. is being explored intensively.

1.2.1. π -conjugated polymers

π -conjugated polymers (CPs) have special electronic and optical properties due to the delocalization of π -electrons. They are dubbed as conductive polymers or organic semiconductors. The π -conjugated polymer consists of carbon atoms bound by alternating single and double bonds, called conjugated double bonds. In polyacetylene, the simplest conjugated polymer $(\text{CH})_x$, atomic orbitals of carbon atoms are sp^2 - hybridized. Three equivalent σ orbitals lie in plane at angles of 120° between each other. The fourth carbon orbital is an unhybridized p_z orbital perpendicular to the sp^2 plane. Each carbon atom forms two σ bonds with neighboring carbon atoms by head-on overlap of their sp^2 orbitals, one σ bond with hydrogen atom by overlap of its sp^2 and hydrogen s orbitals and π bond by sideways overlap of p_z orbitals. The delocalization of π -electrons along the polymer chain gives these polymers special properties. Although polyacetylene is a semiconductor, it can be doped to become electrically conductive. The doping process, which results in an increase of free charge concentration, involves oxidation (removal of electrons) or reduction (addition of electrons) of a neutral polymer. There are two methods of doping a conductive polymer. The first method is a chemical doping and involves exposure of polymer to an oxidant (p -doping, i.e. iodine or bromine) or reductant (n -doping, less common, i.e. alkali metals such as Na). The second method is an electrochemical doping in which a polymer-coated, working electrode is suspended in an electrolyte solution in which the polymer is insoluble along with separate counter and reference electrodes. The potential difference between the electrodes

causes electron addition or electron removal from the polymer. The charged polymer is compensated by the appropriate counter ions from the electrolyte.

In *trans*-polyacetylene charged solitons are formed when the polymer is doped by acceptors or donors at low concentration. In *trans*-polyacetylene at higher polymer concentration and in all other π -conjugated polymers, oxidative doping results in a formation of positive polarons – cation radicals that induce an electronic polarization and spatial chain deformation of surrounding polymer chain. From quantum mechanical point of view polarons are quasiparticles that move along the chain together with their charge. Oxidation of the polymer, mainly at higher dopant concentration, can lead to the formation of bipolarons - dications that move as units along the chain. Polarons, bipolarons and solitons contribute to the electrical conductivity in π -conjugated polymers. The fundamental information about theory, synthesis, properties and characterization of π -conjugated polymers can be found e.g. in the book of Skotheim and Reynolds⁷⁰.

Beside a simple π -conjugated chain as in polyacetylenes, conductive polymers can consist of aromatic cycles as in poly(*p*-phenylene)s, poly(*p*-phenylenevinylene)s, poly(fluorene)s, or heterocycles containing heteroatoms such as sulfur or nitrogen (polypyrroles, polythiophenes). A special example is polyaniline in which the electrical properties depend also on the protonation, additionally to its oxidation state.

Conductive polymers are currently used in a number of devices, such as electrodes in batteries, field effect transistors (organic FET or OFET), and sensors. Recent studies of photon emission by conductive polymers may lead to new technologies for polymer-based flat-panel light emitting displays (OLEDs) and polymer solar cells. Conductive polymers also show promises as molecular wires that can be incorporated into nanometre-size electronic devices.

1.2.2. Preparation of nanocomposites of CPs and noble metal NPs

Several chemical approaches have been developed to prepare π -conjugated polymer nanocomposites with noble metal NPs. Generally, these follow one of two routes: (i) a “one-pot” approach where the metal salt is reduced with a common reductant such as NaBH₄ in the presence of the π -conjugated polymers, or the monomer or polymer acts directly as a reductant for the metal salt, or (ii) a separate preparation of NPs followed by either chemical polymerization of added monomers around the particles or dispersion of the NPs in a polymer

matrix. Both approaches can be utilized effectively in the preparation of dispersed NPs in a polymer matrix.

Nanocomposites of Au NPs and regioregular poly(3-hexylthiophene) were prepared using “one-pot” approach by McCullough et al., who performed the reduction of HAuCl_4 with sodium borohydride in the presence of polythiophene⁷¹. Among the thiophene class of compounds, terthiophene and 3,4-ethylenedioxythiophene (EDOT) can be used as a reductant for gold salt. This approach has been utilized by Advincula to prepare sexithiophene linked Au NPs. In his works a tetraalkylammonium functionalized terthiophene⁷² or terthiophene-functionalized poly(4-vinylpyridine) (PVP3T)⁷³ were used as reductants of HAuCl_4 to Au NPs. In the first case, the ammonium salt formed a polyelectrolyte complex with polystyrene sulfonate, and subsequent addition of the HAuCl_4 resulted in a formation of Au NPs⁷². In the case of PVP3T, Au NPs were prepared within hydrogen-bonded multilayer thin films of PVP3T and poly(acrylic acid). Similarly, Li et al. prepared composite materials using 3,4-ethylenedioxythiophene (EDOT) as a reductant of Au salt in THF solutions with alkylamines as stabilizers^{74, 75}. The Au NPs in the resulting PEDOT/Au NPs composite was found to self-assemble via π - π interactions giving spherical aggregates. In order to obtain aqueous dispersion of PEDOT/Au NPs composite, polystyrene sulfonate was used as a dopant for PEDOT and nanoparticle stabilizer⁷⁶. Au, Pd and Pt NPs of narrow size distributions were prepared via reduction of the metal ions by a π -conjugated poly(dithiafulvene), facilitated by its strong electron-donating properties^{77, 78}. Photopolymerization was also used for the nanocomposite preparation. Breimer et al. prepared films of polypyrrole with metal NPs by photopolymerization (UV-Vis lamp set at 254 nm) of pyrrole solution in the presence of copper, silver and gold salts⁷⁹. The exposure of mixture of 10,12-pentacosadiynoic acid and AgNO_3 to UV irradiation of high-pressure mercury lamp caused the photopolymerization of the diacetylene and photoreduction of silver ions⁸⁰. The Au NPs formation by reduction of HAuCl_4 in aqueous solution of amphiphilic dendrimer molecules with oligo(p-phenylene) core under laboratory ambient white light was described by Chang et al.⁸¹. The disadvantage of this approach is the consumption of the π -conjugated oligomers due to their photodegradation.

The second chemical route to π -conjugated/nanoparticle composites is based on the synthesis of NPs in the first step, followed by either a chemical polymerization of monomer units around these NPs, or dispersion of NPs in a separately prepared polymer solution. For example Oliveira^{82, 83} and Zhang⁸⁴ synthesized composites of metal NPs and CPs by chemical

polymerization of monomers on Ag NP surface. The synthesis of dodecanethiol-capped silver NPs/polyaniline nanocomposite was based on a two-phase polymerization route, in which aniline was dissolved in a Ag NP organosol in toluene and then mixed with an aqueous solution of ammonium persulfate⁸². The polymerization took place at the water/toluene interface where the Ag NPs were incorporated, too. As a result, a layer of polyaniline matrix was obtained with the homogeneously dispersed Ag NPs. In another work they showed that different structures of the nanocomposites can be obtained, such as a thin shell of polyaniline around the Ag NPs or a polymer matrix with embedded NPs⁸³. Polythiophene coated Au NPs were prepared in two-step process by Zhang et al.⁸⁴. First, 3-(10-mercaptodecyl)thiophene stabilized Au NPs were formed by modified Brust's method, followed by a polymerization of thiophene, catalysed by anhydrous ferric chloride.

Feldheim et al. used pre-prepared NPs in his elegant template synthesis of one-dimensional poly(pyrrole)/Au NP arrays⁸⁵. In this method Au NPs are trapped into pores of Al₂O₃ membrane and aligned along the direction of the pore axis. Then the membrane is exposed to pyrrole vapor in one side and to solution of Fe(ClO₄)₃ on the opposite side. Iron(III) salts are known to oxidatively polymerize pyrrole to form polymers doped with the corresponding anion. Finally, the Al₂O₃ membrane is dissolved with aqueous solution of KOH to yield a suspension of 1D colloid/polypyrrole composite structures. This method was also used for the preparation of thioacetyl functionalized phenylacetylene-bridged Au and Ag NP dimers and trimers^{86, 87}.

The preparation of nanocomposites by dispersing pre-prepared metal NPs in a polymer matrix is not a trivial task. In particular, blending of NPs with most polymers is hindered by the phase separation that results in particles clustering or aggregation within the polymer matrix. To avoid this problematic issue, an appropriate NP surface modification has to be introduced⁴⁰. Surface modification with organic and polymer ligands brings the desired stability of the NPs dispersion. A ligand exchange approach is mostly used that typically begins with well-developed strategies for the preparation of NPs of controlled size, shape, and surface functionality using small-molecule ligands. These ligands are then exchanged for the polymer (typically end-capped or side-groups functionalized polymers are used, as with thiol-groups) during mixing the stabilized NPs with the polymer. The amount of added polymer depends on the affinity of small-molecule ligands and of the polymer to the nanoparticle surface. As the molecular weight of the incoming ligand (polymer) increases, it is likely that steric effects slow down the rate of ligand exchange⁴⁰. Studies with small-molecule ligands have shown that the rate of the exchange reaction is also slowed down as the length of the

ligand molecule and the thickness of the ligand shell increases⁸⁸. So, once a polymer ligand shell is in place, the nanoparticle stability is likely to be increased (and surface accessibility decreased). For example, Herrikhuyzen et al. obtained the assembly of oligo(*p*-phenylene vinylene), (OPV), capped Au NPs by ligand exchange method⁸⁹, in which the original tetraoctylammonium bromide stabilizer was replaced by strongly attached OPV derivatized with disulfide moieties.

Electrochemical synthesis is a well-established technique for the preparation of π -conjugated polymer films of polypyrrole, polyaniline or polythiophene. Resulting polymers are usually doped with incorporated electrolyte anions and can be neutralized afterwards by reversing the electrochemical potential. Similarly, the electropolymerization also provides equally efficient technique for incorporating insoluble metal NPs into the growing polymer films, giving birth to a number of composite materials. Depending on the metal, the desired metal NP size and the type of polymer, different techniques have been developed.

The simplest electrochemical process of obtaining composites of a conjugated polymer and metal NPs is based on the electrochemical reduction of metal ions in an electropolymerized polymer immersed in a proper electrolyte system. The electrochemical reduction yields metal NPs embedded in the polymer matrix. Kost et al.⁹⁰ prepared polyaniline films containing Pt particles: in the first step, polyaniline was deposited on a supporting electrode by the electrochemical oxidative polymerization of aniline in the presence of sulfuric acid. Then the polymer coated electrode, in which the polymer is in the conductive protonated form, was immersed into a solution containing PtCl_6^{2-} ions. The penetration of the hexachloroplatinate into the polymer was feasible due to its fibrillar structure. Electrochemical reduction of the salt yielded Pt particles or clusters embedded in the polyaniline matrix. The main disadvantage of this procedure is an inhomogeneous distribution of NPs in the polymer matrix. NPs generally form clusters larger than 100 nm.

Au NPs functionalized with 2-mercapto-3-*n*-octylthiophene were synthesized and then electrochemically co-polymerized with the 3-octylthiophene leading to polyoctylthiophene/Au NP composite films⁹¹. The NP stabilizer was incorporated into the growing polymer chain, yielding a random copolymer with randomly distributed Au NPs in the polymer matrix.

In order to obtain homogeneously distributed Au NPs in a polythiophene matrix, Au NPs were bridged with oligothiophene linkers by electrodeposition⁹². At first, Au NPs were capped with oligothiophenes via phosphine groups. Electrochemical oxidation of

oligothiophenes bound to Au NPs results in the deposition of thin films consisting of isolated Au NPs linked by oligothiophene moieties.

Interesting behaviour was observed in the case of layers of polyaniline deposited on gold electrodes in the presence of chloride ions. The chloroaurate anion was generated at the Au electrode surface. In addition, chloroaurate anion formed a complex with polyaniline at the nitrogen linkages. Then, the chloroaurate complex was reduced to form metallic Au clusters in the polyaniline film⁹³.

1.2.3. Morphology and optical properties of CPs nanocomposites with noble metal NPs

The effect of the interaction between excited state of CP and SPs excitations in metal NPs was studied in model systems where NPs were linked by short π -conjugated linkers^{89, 94-97}. Table 1-2 shows various linker molecules used by Wessels et al. for his investigation of optical properties of films of Au NPs interlinked by these molecules. It was found that SPE maxima of such films are red-shifted compared to those of films of Au-NPs interlinked by non-conjugated molecules of the same length. The most pronounced changes were observed for the bis-dithiocarbamate interlinked Au-NP assemblies. In this case of π -conjugated linker (PBDT), the SPE band which had been observed at 589 and 573 nm for BDMT and DMAAB (for chemical structures see Table 1-2), respectively, disappeared and only a strong metallic absorption was observed in the near-IR. Non-conjugated linker (cHBDT) also exhibited an increase of absorbance in the near-IR, however SPE band still occurred with the maximum at 626 nm. The metallic absorption for the NP assemblies with π -conjugated linker was explained by an overlap of the molecular orbitals of the linkers and metal electron wave functions causing the formation of a resonant state that affects the absorption of the film.

Kim et al.⁹⁵ investigated the adsorption characteristics of 1,4-phenylene diisocyanide on Au NPs. Addition of a small amount of conjugated molecules into the Au sol caused a substantial decrease of SPE band at 520 nm and, simultaneously, a new band around 700 nm was observed with increasing linker concentration, assigned to the formation of highly aggregated structures. This result confirmed the interaction between Au NPs and conjugated linker molecule via lone-pair electrons of isocyanide groups. At low adsorbate concentrations, small-sized aggregates and isolated particles were observed because of the effect of the repulsive barrier between Au NPs covered by citrate ions. Upon the increasing adsorbate concentration, large aggregates were formed since the repulsive barrier had been broken by a

strong adsorption of 1,4-phenylene diisocyanide on the Au NP surface. Novak and Feldheim⁸⁷ used rigid thiol-functionalized oligophenylacetylenes of different length as linkers for Ag and Au NPs to form dimers and trimers. The observed changes in SPE spectrum of Ag NPs were attributed to the bridging of nanoparticles by linker molecules.

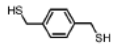
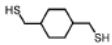
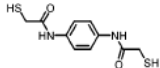
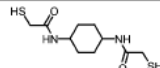
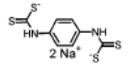
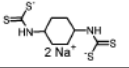
Linker	Length (Å)	$\Delta(E_{\text{HOMO-LUMO}})$	
(1a) BDMT 	7.7 ^a	4.0	bis-mercaptomethylenes
(1b) cHDMT 	8.2 ^a	5.0	
(2a) DMAAB 	14.8 ^a	3.5	bis-acetamidothiols
(2b) DMAAcH 	14.9 ^a	4.7	
(3a) PBDT 	10.7 ^b	2.7	bis-dithiocarbamates
(3b) cHBDT 	9.6 ^b	3.2	

Table 1-2. Overview of linker molecules used in ref.⁹⁴.

Among the papers which report the investigation of the role of oligomers on the optical properties of metal NPs the study of Zotti et al.⁹⁷ should be mentioned. In this work the interaction between Au NPs and several thiophene and pyrrole oligomers was investigated. The main outcome of this study was that polyconjugated heterocyclic oligomers can aggregate Au NPs. The aggregation kinetics of Au NPs was dependent on the oligomer type and concentration. Some interesting results have been found: (i) the critical concentration, at which the aggregation occurs, decreases as the oligomer length increases (longer oligomers provide multiple coordination sites), (ii) a higher polarity of the heteroaromatic molecule and the presence of additional coordinating atoms favour adsorption to gold, (iii) the hindrance of aggregation is provided by alkyl substitution of the oligomer. Depending on the oligomer type used for aggregation of Au NPs, various types of structures were observed, changing from spherical aggregates with the size around 300 nm to irregular dendritic superstructures. Self-assemblies of Au NPs functionalized by oligo(*p*-phenylene vinylene) (OPV) into fractal-like aggregates were also observed by Herrikhuyzen et al.⁸⁹. The originally isolated OPV-functionalised Au NPs were transferred into 1-butanol in which organization of particles into spherical aggregates occurred. The formation of these structures was reversible and took place below 80 °C, above this temperature the organized structures

disappeared. SPE spectra confirmed the occurrence of these structures. The aggregation was found to be dependent on the nature of the used solvent, the OPV-Au concentration and nanoparticle size. On the other hand, the various organization of nanoparticles could be also assigned to the morphological changes of the oligomer on Au NPs which could act as nucleation centres for a possible crystallization of the oligomer.

The optical properties of the above listed composites confirmed the mutual interaction between π -electrons and SPs of metal NPs. In the UV-Vis spectra of composites with CPs, the changes in π - π^* absorption band of the polymer, which mostly dominates in the spectrum of nanocomposite, are connected with its interaction with LSPR of NPs and *vice versa*. For example, a red shift of SPE band of Au NPs embedded in oxidized π -conjugated poly(dithiafulvane) was ascribed to a decrease of the work function of Au NPs, which lowers the energy of the surface resonance state⁷⁸.

Moreover, the energy of the π - π^* absorption band can be used for an estimation of the effective conjugation length of the polymer: red-shifts in the π - π^* absorption band indicate an increase in the conjugation length. Red shift of the absorption band of diacetylene monomers indicated the polymerization of diacetylenes which occurred under UV irradiation. Simultaneously, Ag ions present in the solution of monomer were photoreduced. As a result Ag coated polydiacetylene composite particles are formed⁹⁸.

The spectral blue shift mostly indicates the degradation of the CPs⁹⁹. Low stability against degradation is a common problem associated with CPs which limits the performance in devices such as light emitting diodes. The blue shift of the bipolaron absorption band (from 826 to 780 nm) and that of the polaron band (from 420 to 383 nm) were observed after ultrasonic treatment of spherical Au aggregates embedded in poly(3,4-ethylenedioxythiophene) by Li et al¹⁰⁰. This was assigned to the decrease of the antiparallel dipole interaction between the conjugated backbones of PEDOT molecules in adjacent Au NPs.

1.2.4. Electronic properties of CPs nanocomposites with noble metal NPs

Research in electronic properties of nanocomposites is a rapidly emerging field of great fundamental and practical interest owing to their potential to serve as building blocks in nanoelectronic devices. The charge transport phenomena between individual particles⁹², monolayers¹⁰¹⁻¹⁰³, multilayers¹⁰⁴ as well as in two- and three-dimensional structures^{92, 94} have been investigated. Generally, it was found that the electrical conductivity of nanocomposites

depends on nanoparticle size and aspect ratio, homogeneity of NPs spatial distribution and on the mean interparticle distance.

When the particles are linked by nonconjugated linkers, electron tunneling is the predominant mechanism for the electrical conduction. Murray et al.¹⁰⁵ used an Arrhenius-type activated tunneling model to describe the electron transport through a three-dimensional network of Au NPs covered with a monolayer of various organic materials as arene- as well as alkanethiolate molecules. The electrical conductivity (σ) depends on the electronic coupling term (β) and the energy barrier (E_A) to the electron transfer:

$$\sigma = \sigma_0 \exp[-\beta\delta] \exp[-E_A/k_B T] \quad (9)$$

where δ is the average interparticle distance, k_B is Boltzmann constant, T is the temperature and σ_0 includes the charge carrier concentration and mobility of the charge carriers in conjugated linkers. Thus, the electrical conductivity decreases as the length of the linker increases due to electronic coupling term. Therefore, it is interesting to prepare systems with fixed interparticle distance and varying β and E_A .

In order to vary activation energy for electron transfer between NPs many different ligand molecules have been used. Torma et al.¹⁰⁶ used linkers covalently or non-covalently bound to Au NPs. In the case of noncovalently linked Au NPs a linear relation between NPs distances and activation energy indicates that only the distance between the nanoparticles determines the energy of the hopping processes. This can be explained by the fact that there is no direct electronic interaction between the Au NPs and the stabilizing ligand molecules. On the other hand, the activation energies are characteristically lower and do not depend linearly on the NP spacing for covalently bound linkers. This suggests an electron-transport mechanism, where bonding and/or antibonding molecular orbitals of the ligand are involved in the conductivity process. Similar results were obtained by Bourgoin et al.¹⁰² for monolayers of Au NPs prepared by Langmuir-Blodgett technique. The electrical conductivity of a monolayer of dodecanethiol-capped Au NPs is compared with that obtained after the subsequent interconnection of NPs by a displacement of the dodecanethiol by 2,5''-bis(acetylthio)-5,2',5',2''-terthienyl. Electrical measurements showed a three orders of magnitude increase of the conductivity and a decrease of activation energy upon the displacement. These studies suggest that it would be of significant interest to link NPs using

fully conjugated molecules in three dimensions, thus improving the interparticle charge transfer.

Recent efforts were focused on three-dimensional structures in which NPs are linked by molecules possessing an extended π -conjugated electron system or by π -conjugated polymers. It is assumed that a π -conjugated linker serves as a “molecular wire” that enhances the electronic coupling between adjacent particles. In the paper by Sih et al.⁹², the electrical conductivity of dry films of Au NPs capped with terthiophenes moieties containing phosphine groups were compared with those obtained by electrochemical oxidation of these particles. It was found that unlinked terthiophene-capped Au NPs have the conductivity three orders of magnitude lower compared to the linked particles. The substantial increase in the electrical conductivity was assigned to a better charge propagation through the conjugated bridge.

Wessels et al.⁹⁴ showed that the replacement of the benzene ring in conjugated linkers with the cyclohexane ring (Table 1-2) led to a one order of magnitude decrease in conductivity. The authors suggested that the electron transport is a partially nonresonant tunneling process along the parts of a molecule with saturated electron system and partially resonant tunneling through the π -conjugated parts of a molecule. In other words, the molecules can be viewed as consisting of two electrically insulating (the nonconjugated) parts in series with conductive (the conjugated) parts. Interestingly, the conductivity increased with decreasing temperature for the films of conjugated bis-dithiocarbamate (PBDT) interlinked Au NPs. This was in agreement with the optical properties of this film showing the metallic behavior and indicated the high degree of conjugation of PBDT and good Au-NP/PBDT contact with overlapping adjacent NP electronic wavefunctions.

The conductivities of composites consisting of Au NPs and π -conjugated polymers such as polythiophene⁷¹, polyaniline¹⁰⁷ or polypyrrole⁷⁹ were measured and the values were more than two orders of magnitude higher than the conductivities of the films of pure polymer. For example, the electrical conductivity of the Au nanoparticle–polyaniline composite^{107, 108} was found to be 0.3 S cm^{-1} upon incorporation of Au NPs (Au content: 0.04 vol %) whereas that of neat polyaniline was $2.4 \times 10^{-3} \text{ S cm}^{-1}$. Nevertheless, there has been no study published yet concerning percolation behavior of the conductivity in the presence of Au NPs. The conductivity mechanism has not been elucidated as well.

1.2.5. Photophysical processes on metal NP surface

LSPRs of metal NPs are able to markedly enhance Raman scattering and locally influence fluorescence of surrounding molecules. These techniques provide specific information about molecules adsorbed on metal surface. Raman spectroscopy, for example, is able to probe molecular vibrations, but the method usually suffers from relatively weak signal intensity. The number of inelastically scattered photons is extremely small (about 1 in 10^7 of the incident photons). Plasmonic NPs provide a general method for enhancing Raman signals to levels that can make many analytical applications possible. The chapters below are focused on the background of these phenomena, that are also demonstrated on several examples of composites of CPs with metal NPs emerging from recent research.

1.2.5.1. Surface-enhanced Raman scattering

The discovery of surface-enhanced Raman scattering (SERS)^{24, 109, 110} showed that it was possible to enhance the intensity of Raman scattering by a roughened noble metal surface on which the analyte molecules are located. The ability to enhance the Raman signal via SERS is fundamentally connected with the morphology of the nanostructured surface as well as with the choice of the metal. The materials used for SERS are mainly, but not exclusively, Ag, Au, Pt and Cu. New methods to create nanostructured metals are constantly evolving, and SERS targeted research follows the trendwork of increased sensitivity to the levels required for advanced sensing applications⁶. Recently, the interest moved to novel microscopic techniques such as Raman confocal and near-field microscopies and to the ability to detect and characterize a single molecule. Signal enhancements up to 10^{14} over normal Raman scattering have been observed in these special cases. The extraordinary high enhancement is connected with “hot spots”, i.e. nanoscale localized strong optical fields, and only molecules adsorbed in these “hot spots” are able to produce Raman signal high enough to make detection of a single molecule possible¹¹¹⁻¹¹⁴.

Briefly, the intensity I_{RS} of Raman scattering (RS) is proportional to the square of the dipole moment $\vec{\mu}$ light-induced in the molecule, which is given as the product of the molecular polarizability tensor $\vec{\alpha}$ and the electric field intensity \vec{E} :

$$I_{RS} \approx |\vec{\mu}|^2, \quad (10)$$

$$\vec{\mu} = \vec{\alpha}\vec{E}. \quad (11)$$

Hence, there are two possibilities how the RS can be enhanced: either an increase of α or \vec{E} . Also the combination of both enhancements is possible. Accordingly, SERS enhancement can be explained by two mechanisms: the electromagnetic (EM) and the molecular resonance mechanism.

1.2.5.1.1. Electromagnetic mechanism of SERS

The EM mechanism of SERS is the principal mechanism of SERS that operates independently on the nature of the studied molecule^{24, 115-117}. It is based on the enhancement effect achieved through resonance Mie scattering. The theory of the electromagnetic enhancement of RS of molecules adsorbed on spherical metal NPs predicts that strong enhancement will be achieved when: (i) the particle size is much smaller than the wavelength of the incident radiation, (ii) the frequency of exciting and/or scattered radiation is close to LSP resonance of metal NPs, and (iii) the molecule is in a close distance to the nanoparticle surface.

The extreme enhancement of SERS stems from the fact that the optical wave is enhanced twice. The incident as well as Raman scattered radiation is enhanced by excitation of dipolar surface plasmon and by the resulting dipole emission i.e. by the resonance Mie scattering. SERS enhancement factor (G_{EM}) can be expressed as:

$$G_{EM} = \frac{I_{SERS}}{I_{RS}} = k \left(\frac{\varepsilon(\lambda_0) - \varepsilon_{med}}{\varepsilon(\lambda_0) + 2\varepsilon_{med}} \right)^2 \left(\frac{\varepsilon(\lambda_s) - \varepsilon_{med}}{\varepsilon(\lambda_s) + 2\varepsilon_{med}} \right)^2, \quad (12)$$

where k is empirical constant, $\varepsilon(\lambda_0)$ and $\varepsilon(\lambda_s)$ are complex permittivity for the metal at the wavelength of incident and scattered radiation (by a Stokes process), respectively, and ε_{med} is relative permittivity of the local medium. The EM mechanism enhancement can range between 4 and 11 orders of magnitude, in dependence on the morphology of the metal nanostructure, localization of a molecule within the assemblies, the excitation wavelength and light polarization selected for the SERS experiment.

The choice of metal substrate is determined by its LSPR frequency. Visible and near-infrared radiation (NIR) is used in SERS spectroscopy. Silver and gold are typical metals for SERS experiments because their LSPR frequency falls within these wavelength ranges, providing maximal enhancement for visible and NIR light.

1.2.5.1.2. Mechanisms of molecular resonance

Molecular resonances contribute to the overall enhancement of Raman scattering provided that their resonance condition is fulfilled simultaneously with the EM resonance. Molecular resonance is similar to that in the resonance Raman spectroscopy. This technique modifies the basic Raman experiment by using incident radiation that nearly coincides with the frequency of an electronic transition within the molecule.

Two types of molecular resonance contributions in SERS are considered in the literature.

- (i) SERRS: A molecule itself is a chromophore with respect to the excitation wavelength used in the SERS experiment. The molecular resonance contribution has to be evaluated for the actual adsorbed species^{118, 119}.
- (ii) Chemical mechanism: A molecule itself is non-chromophoric with respect to the excitation wavelength, but forms a chromophoric surface complex. The exciting radiation is in resonance with a charge-transfer transition of a newly formed surface-adsorbate complex^{120, 121}.

1.2.5.1.3. SERS of π -conjugated polymers

The use of SERS spectroscopy to characterize conducting polymers has attracted increasing interest during the last ten years and many papers have been published recently¹²²⁻¹²⁶. SERS spectroscopy has appeared to be an efficient tool for the study of polymer films, since it allows obtaining not only a selective insight into the polymeric structure but also information concerning the orientation and binding of the conjugated chains on the metal surface. Moreover, it suppresses a strong fluorescence emitted by many π -conjugated polymers.

For example, SERS spectra of polythiophene (PT) and its derivatives recorded on roughened Ag, Au, Pt and Cu electrodes as well as in Ag colloid allowed the vibrational analysis of PTs^{123, 126}. The vibrational modes are different for the polymer in the neutral and doped forms, thus providing a way for evaluating the oxidation level of PT films. SERS spectroscopy also provided a detailed molecular structure analysis of PT films during the doping-dedoping process¹²⁴.

The deposition of strongly fluorescent π -conjugated polymer, poly(2-pyridinium hydrochloride-2-pyridylacetylene) (P2EPH, Figure 1-6), on rough silver surface led to the substantial fluorescence quenching which allowed the observation of Raman spectra with excitation in the visible region¹²⁷. The SERS spectra of P2EPH measured on Ag electrode, in Ag pellet and in Ag sol were similar, regardless of which form of silver was used. Furthermore, it was demonstrated that the enhancement mechanism is essentially electromagnetic and the vibrational modes are not affected by the metal surface. The frequencies of some vibrational modes assigned to polyacetylenic chain vibrations showed a dependence on the energy of the exciting radiation; this phenomenon which was firstly described for polyacetylenes is known as Raman dispersion¹²⁸. However, the observed dependence of the position of these bands on the excitation wavelength is much smaller than that reported for polyacetylenes, which probably indicates a limited range of the delocalization of π -electrons in P2EPH.

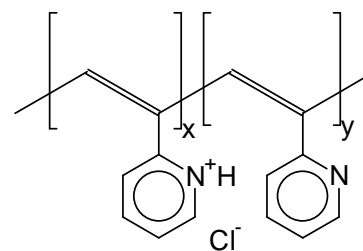


Figure 1-6. Chemical structure of P2EPH.

1.2.5.2. Fluorescence

In the vicinity of a metal surface, both the radiative processes and/or non-radiative deactivation pathways of the excited chromophore molecule change due to the interaction with LSPR of metal NPs. The chromophore emission intensity depends on the distance between the metal nanoparticle and the chromophore^{6, 129}, mutual orientation of molecular orbitals and surface plasmon associated dipoles, and wavelengths of the SP resonance and excitation and emission maxima of the chromophore. At a very close distance, less than several nm, the chromophore experiences significant non-radiative decay and, consequently, the emission is strongly quenched. At intermediate distances, around 5 nm for silver, the non-radiative decay process subsides and the enhancement effect begins to dominate. A variety of effects such as increased fluorescence intensities, increased photostability, and increased range of fluorescence resonance energy transfer (FRET) was observed due to the presence of metal NPs¹³⁰⁻¹³⁴.

1.2.5.2.1. Surface-enhanced fluorescence

Fluorescence enhancement arises from the enhanced chromophore absorption through Mie resonance scattering. The effect of fluorescence enhancement has been intensively

studied^{129, 131, 132} and the enhancement factor was found to reach values in the order of 10, depending on the quantum yield of the fluorescence of the chromophore¹¹⁸ and its distance from the metal surface. The fluorescence of a chromophore in the vicinity of a nanostructured metal can be described by the following relationships

$$Q_m = \frac{\Gamma + \Gamma_m}{\Gamma + \Gamma_m + k_{nr}} \quad (13)$$

$$\tau_m = \frac{1}{\Gamma + \Gamma_m + k_{nr}} \quad (14)$$

where Q_m is the fluorescence quantum yield and τ_m is the chromophore lifetime modified by the nanostructure, k_{nr} is the non-radiative rate, Γ is the radiative rate of the isolated chromophore and Γ_m is the additional rate induced by the nanostructure¹²⁹.

The combined use of plasmonic structures and fluorescence molecules bring new abilities to the fluorescence techniques. These possibilities include: the ability to measure distances between biomolecules, metallic structures that selectively enhance excitation or emission at desired wavelengths without enhancing background emission, probes that provide localized multiphoton excitation or emission with low-intensity wide-fields illumination or ultrabright photostable probes for single-molecule detection and imaging¹³².

1.2.5.2.2. Fluorescence quenching

The close vicinity of a metal nanoparticle surface may alter the nonradiative deactivation pathways of the excited state of the chromophore molecules. Chromophore quenching occurs when the chromophore is located in close proximity to metallic surface (typically < 5 nm). Both energy-transfer and electron-transfer¹³⁵⁻¹³⁸ processes are considered to be the major deactivation pathways for excited chromophore on metal surface.

Fluorescence (Förster) resonance energy transfer (FRET) is a photo-physical process through which an electronically excited donor molecule transfers its excitation energy nonradiatively to an acceptor molecule. Energy conservation requires that the energy gaps between the ground and the excited states of participating donor and acceptor molecules are nearly the same. This in turn implies that the fluorescence emission spectrum of the donor must overlap with the absorption spectrum of the acceptor. The rate of the energy transfer (k_{DA}) is given by:

$$k_{DA} = k_{rad} (R_F/R)^6 \quad (15)$$

where k_{rad} is the donor radiative transition rate, R the center to center separation distance between the donor and the acceptor and R_F is the Förster radius, which is a function of the oscillator strengths of the donor and acceptor molecules, their mutual energy resonance, and summation of their dipole vectors.

A number of theoretical and experimental studies exist on the rate of non-radiative energy transfer from a dye to both a flat metallic surface¹³⁹ and a metal nanoparticle¹⁴⁰⁻¹⁴². The energy transfer in the hybrid composites or assemblies containing metal NPs depends critically on the nanoparticle size and shape, the distance between the dye molecule and the nanoparticle, the orientation of the molecular dipole with respect to the dye-nanoparticle axis, and the overlap of the chromophore emission with the nanoparticle absorption¹⁴³. Saini et al.¹⁴⁴ examined the distance dependence of resonance-energy transfer between a fluorescent dye and a Au NP and between two NPs. They found that the rate of the resonance-energy transfer followed a distance dependence of $1/d^\sigma$ where exponent σ approaches 6 at large distances ($d \gg R$, R is nanoparticle radius) whereas at short distances ($d < 20R$) a value varied from 3 to 4. The authors suggested that the difference may be understood in terms of energy transfer on the NP. Furthermore, this energy transfer occurs at distances that are two times longer than it is usual for the dipole-dipole energy transfer. Thus, the energy transfer from a molecular excited state to the nanostructured metal surface plasmons shows a very different distance trend¹⁴².

Photoinduced electron transfer. Au NPs have a unique ability to accommodate electrons from multiple charge-transfer processes from attached organic molecules¹⁴³. Their ability to display quantized (single electron) charging has been demonstrated by Murray¹⁴⁵. Control of charging of Au NP thus becomes an important factor if one is interested in modulating the interaction between the Au NP and a surface-bound chromophore. Such a photoinduced electron-transfer process was observed only for small NPs with the diameter lower than 5 nm.

Electron transfer was experimentally confirmed between pyrene thiol chromophore and Au NP suspended in THF solutions^{135, 136}. The suppression of the intersystem crossing and/or total quenching of the triplet excited state in pyrene as well as the formation of pyrene cation in this system confirmed that the main deactivation channel of the singlet excited state of pyrene linked to Au NPs is an electron transfer between the chromophore excited state and the surface plasmon state of Au NPs. Interestingly, the charge separation was sustained for several microsecond before undergoing recombination. The electron storage ability of Au NPs

might improve the charge separation in light harvesting energy conversion systems. Au NPs functionalized with two different thiols, one contained a chromophore (pyrene) and the other a carboxylic acid (sulfanylpropionic acid) which served as a linker between Au NPs and TiO₂ surface, were also reported¹³⁸. The spectroelectrochemical experiments were performed on a thin-layer of TiO₂ with adsorbed Au NPs and pyrene chromophores in an electrochemical cell and emission spectra were measured at various applied potentials. At a neutral or positive potential of the electrode, the photoinduced charge transfer takes place upon the photoexcitation of pyrene and the fluorescence is quenched. As the electrode is biased to negative potentials, the electron transfer from excited pyrene molecules to Au NPs experiences a barrier since they are negatively charged. Therefore, the charge transfer between the chromophore and Au NPs is suppressed, and the light emission from the photoexcited pyrene molecules occurs.

Fluorescence quenching observed for composites of CPs and metal NPs was discussed in a few papers but the mechanisms remain unclear. Heeger and coworkers¹⁴⁶ published the efficient fluorescence quenching of cationic poly- and oligofluorenes by citrate stabilized Au NPs (Figure 1-7). Three factors were taken into account for the discussion of this efficient quenching:

(i) electrostatic interaction between cationic oligomers and anionic Au NPs; (ii) the ability of Au NPs to quench fluorescence via highly efficient, relatively long-range resonance energy transfer, rather than electron transfer; and (iii) amplification of the quenching efficiency by exciton transfer or electron transfer within the conjugated polymer. Unfortunately, the morphology of nanoparticles, which could play the important role in fluorescence quenching, in oligomer or polymer composites containing Au NPs is not discussed in the paper.

Wu et al.¹⁴⁷ reported the preparation of the silica-coated fluorescent conjugated polymer (polyfluorene and polyphenylenevinylene derivatives) nanoparticles. Functionalization of the nanoparticles shell with amine groups followed by the addition of Au NPs (prepared by citrate reduction) resulted in the formation of nanoparticle assemblies. Efficient fluorescence quenching of the encapsulated polymer nanoparticles by Au NPs was

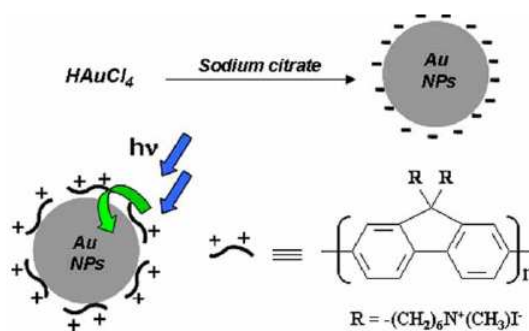


Figure 1-7. Superquenching observed in ref.¹⁴⁶ for polyfluorene-Au NPs composite material. Cationic polymer is adsorbed on the anionic Au NPs via electrostatic interaction.

observed and it was assigned to the resonance energy transfer; since the electron transfer is likely blocked by the silica shell in this case. Interestingly, in a reference system composed of a mixture of the same polymer with Au NPs no fluorescence quenching was observed, except of a small inner filter effect.

2. OBJECTIVES

- Testing the possibility of preparation of monodisperse nanoparticles using treatment by high energy laser pulses. Understanding of the mechanism as well as optimization of the process of laser fragmentation of chemically prepared Au hydrosols. In particular, control of the process by the parameters of the laser pulse radiation used for NP fragmentation: laser pulse energy, its wavelength and characteristics of the parent hydrosols, namely, the nanoparticle size will be explored.
- Development of preparative strategies for nanocomposites containing π -conjugated polymers and noble metal nanoparticles. Refinement of the existing and development of new methods of metal nanoparticle preparation will be pursued. Novel π -conjugated polymers as well as common available π -conjugated polymers having both the functional groups and molecular units enabling their anchoring to the metal nanoparticle surface will be designed and tested.
- Fabrication of nanocomposites with well defined morphologies of metal nanoparticles exhibiting the surface-enhanced optical phenomena, e.g. surface-enhanced Raman scattering. A special attention will be focused on exploitation how the morphology of metal nanostructures (nanoparticle sizes, shapes, aggregation, and mutual distances) influences these phenomena.
- Investigation of the Raman scattering and luminescence in “hot spots” generated by the exciting external optical fields in 3-dimensional arrays of metal nanostructures in polymer nanocomposites.

3. EXPERIMENTAL

3.1. List of chemicals

NaBH_4	sodium borohydride (Merck)
$\text{HAuCl}_4 \cdot 3\text{H}_2\text{O}$	hydrogen tetrachloroaurate(III) trihydrate (Sigma-Aldrich)
AgNO_3	silver nitrate (Merck)
$(\text{C}_8\text{H}_{17})_4\text{N}^+\text{Br}^-$	tetraoctylammonium bromide, TOAB, (Aldrich)
$(\text{C}_{12}\text{H}_{25})_4\text{N}^+\text{Br}^-$	tetradodecylammonium bromide, TDAB, (Fluka)
$(\text{C}_4\text{H}_9)_4\text{N}^+\text{ClO}_4^-$	tetrabutylammoniumperchlorate, TBAPC, (Fluka)
CH_3OH	methanol (Lach:ner)
CH_2Cl_2	dichloromethane, DCM, (Lach:ner)
$\text{C}_7\text{H}_9\text{O}$	toluene (Aldrich, A. C. S. Reagents)
$(\text{CH}_3)_2\text{SO}$	dimethylsulfoxide, DMSO, (Sigma-Aldrich, A. C. S. spectrometric grade)
H_2O	deionized distilled water, specific resistance: 18 M Ω cm (Elgastat UHQII purification system (Elga, UK))
HNO_3	nitric acid (Lach:ner)
H_2SO_4	sulfuric acid (Lach:ner)
HCl	hydrochlorid acid (Lach:ner)
H_2O_2	hydrogen peroxide (Lach:ner)
$(\text{C}_9\text{H}_{10}\text{N}^+\text{I}^-)_n$	poly(N-ethyl-2-ethynylpyridinium iodide), PEEP-I (kindly provided by Dr. Sedláček, Charles University in Prague)
$(\text{C}_{12}\text{H}_{18}\text{S})_n$	poly(3-octylthiophene-2,5-diyl), P3OT, regioregularity > 98.5 % (Sigma-Aldrich)
$(\text{C}_{18}\text{H}_{28}\text{O}_2)_n$	poly[2-methoxy-5-(2-ethylhexyloxy)-1,4-phenylenevinylene], MEH-PPV (Sigma-Aldrich)

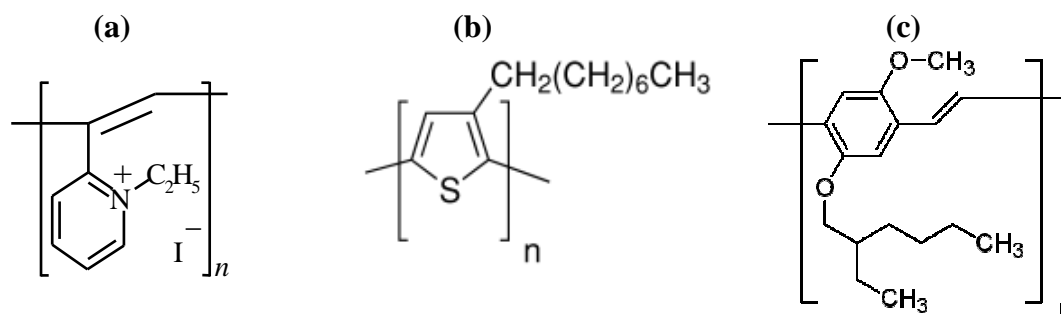


Figure 3-1. Chemical structures of polymers used in the experiments described in respective chapters: (a) poly(N-ethyl-2-ethynylpyridinium iodide), PEEP-I, Chapter 4.2., (b) poly(3-octylthiophene-2,5-diyl), P3OT, Chapter 4.3., (c) poly[2-methoxy-5-(2-ethylhexyloxy)-1,4-phenylenevinylene], MEH-PPV, Chapter 4.4.

PEEP-I was synthesized by Dr. Sedláček (Charles University in Prague, Faculty of Science, Department of Physical and Macromolecular Chemistry) by reacting 2-ethynylpyridine with iodoethane in bulk that lead to a formation of conjugated ionic PEEP-I through a spontaneous polymerization of the intermediate N-ethyl-2-ethynylpyridinium iodide^{148, 149}. Number-average molecular weight for PEEP-I determined by SEC analysis (DMF, PMMA calibration) was $M_n = 31\ 000$.

P3OT and MEH-PPV were purchased from Sigma-Aldrich and used as received. According to the liquid chromatography acquired on HP 1100 apparatus, using polystyrene calibration standards, molar weights were determined as $M_n = 18\ 700$ g/mol and 63 800 g/mol for P3OT and MEH-PPV, respectively.

Glassware

All glassware was cleaned by the mixture of sulphuric acid and hydrogen peroxide dubbed “piranha” solution (3 parts of concentrated H_2SO_4 and 1 part of concentrated H_2O_2) in order to remove residual organics. Then, it was washed with freshly prepared aqua regia (three parts HCl, one part HNO_3) to remove Au or with diluted HNO_3 (1 part of concentrated HNO_3 and 1 part of H_2O) to remove Ag contamination from previous experiments. It was followed by extensive rinsing with distilled and, subsequently, with deionized water. In Chapter 4.1., deionized redistilled water was used for rinsing to avoid residual ionic species.

3.2. Preparation procedures used for respective chapters

to Chapter 4.1.

Au nanoparticle hydrosols (Au1 – Au4) were received from Dr. Šlouf (Institute of Macromolecular Chemistry ASCR, v.v.i.). Size-controlled preparation procedure described in details in ref.³¹ and based on a modification of an earlier reported procedure²⁸ was employed to yield hydrosols with pre-calculated mean Au NPs sizes of 4.5 nm (Au1), 11.7 nm (Au2), 35.0 nm (Au3) and 105.8 nm (Au4), respectively. Briefly, the hydrosols were prepared by reduction of $HAuCl_4$ by hydroxylamine hydrochloride in the presence of small Au NPs previously prepared by reduction of $HAuCl_4$ by $NaBH_4$, acting as seeds. Since in the size-controlled preparation, the amounts of the reactants, and, consequently, the size of the particles varied, the resulting concentrations of Au NPs were 6×10^{13} , 1×10^{12} , 3×10^{10} and 8×10^9 NPs/mL, for Au1 - Au4 hydrosols, respectively.

to Chapter 4.2.

Ag nanoparticle hydrosol was prepared by reduction of AgNO_3 with NaBH_4 following the procedures described in ref.^{29, 150}. Briefly, 3.5 mg of NaBH_4 was dissolved in 75 mL of deionized water and cooled down to 2 °C. After reaching this temperature, 9 mL of 2.2×10^{-3} M aqueous solution of AgNO_3 (precooled to ~ 8 °C) was dropwise added under vigorous stirring. Stirring was continued for 45 min. The resulted colloid was bright yellow with the maximum of SPE band at 396 nm.

The Ag/PEEP-I SERS-active systems of various Ag to polymer ratios were prepared by adding a measured volume of PEEP-I stock solution in DMSO to 2 mL of the Ag hydrosol. Several batches were prepared with the resulting PEEP-I concentrations in the nanocomposite systems between 5×10^{-8} M and 1×10^{-4} M.

to Chapter 4.3.

Preparation of Au organosols in toluene. Au organosols were prepared by adopting the procedure originally developed by Brust et al. for thiol-derivatised Au NPs dispersed in toluene⁴¹. An aqueous solution of HAuCl_4 (30 mM, 6 mL) was added to 16 mL of 50 mM toluene solution of phase-transfer agent, tetraoctylammonium bromide (TOAB) or tetradodecylammonium bromide (TDAB), to form a two-phase system which was then vigorously stirred for 20 min in order to transfer metal ions into the organic phase. The originally yellow aqueous phase became colourless and the initially colourless toluene phase turned red as a result of the optical absorption of AuCl_4^- ions transferred into this phase. In the next step, the aqueous phase was removed in a separatory funnel and a freshly prepared solution of reducing agent (NaBH_4) in deionized water (0.5 M, 2.5 mL) was slowly added to the toluene phase containing AuCl_4^- ions. The mixture was stirred for two hours and, after phase separation, the toluene phase was collected and three times washed with redistilled deionized water to remove side products. The synthesis was performed at room temperature in the case of using TOAB while elevated temperature ($T \approx 37$ °C) was used for the preparation of organosol with TDAB because of its worse solubility at room temperature.

Preparation of Ag organosols in toluene. First, the same procedure as for Au organosols was used for Ag organosol preparation, using TOAB as a phase-transfer reagent. However, in comparison to Au organosols, a higher tendency to NPs sedimentation was observed after the reducing agent was added and during the subsequent three-hour stirring of the reaction mixture. In case of using TDAB as a phase transfer reagent, the stirring was limited only for 5 min to avoid NPs aggregation. After the stirring, the aqueous phase

containing reductant was removed and the resulted Ag organosol was left to stay overnight at laboratory temperature. It should be noticed that both solutions of the phase transfer reagent and AgNO_3 are colourless. The transfer of Ag ions from the aqueous into the organic phase is accompanied by the color change of aqueous phase from colourless to milky colour which corresponds to the formation of AgBr precipitate.

Ag/P3OT and Au/P3OT nanocomposites of a type M were prepared by mixing the Au or Ag organosols prepared as described above with a P3OT solution, which was prepared by dissolution of 35 mg P3OT in case of composites with Au NPs or 19 mg P3OT in case of composites containing Ag NPs in 6 mL of toluene. Then 6 mL of the polymer solution was added to 16 mL of the metal organosol to prepare nanocomposites type **M**, followed by vigorous stirring for two hours. Then cca 200 mL methanol was added and after the precipitation the nanocomposite **M** was isolated by centrifugation, two times washed with methanol and finally dried in vacuum oven at 65 °C for four hours. Au/P3OT and Ag/P3OT weight ratios in the resulting composites **M** were 1/1.

Ag/P3OT and Au/P3OT nanocomposites of a type R were prepared by an *in situ* reduction of metal ions with NaBH_4 in P3OT solution. At the first stage, a solution of metal ions was prepared using the procedure described above for the preparation of metal organosols (until addition of NaBH_4). Then 6 mL of the polymer solution, containing 35 mg P3OT in case of Au/P3OT nanocomposites and 19 mg P3OT in case of Ag/P3OT composites, was admixed. Finally, an aqueous solution of NaBH_4 (0.5 M, 2.5 mL) was stepwise added under vigorous stirring. The reaction mixture was stirred for two hours, then poured into a separatory funnel to remove the aqueous phase. The nanocomposite **R** was purified according to the same procedure described above for the nanocomposites type **M**. Au/P3OT and Ag/P3OT weight ratios in the resulted composites **R** were 1/1.

to Chapter 4.4.

Preparation of Au organosols in dichloromethane (DCM). Au organosol in DCM was prepared by the same pathways as Au organosol in toluene since the phase transfer reagent (TOAB) is also well soluble in DCM.

Au/MEH-PPV nanocomposites type M and R. The procedures described above to Chapter 4.3. for the preparation of Au/P3OT composites type **M** and **R** were used for the preparation of Au/MEH-PPV composites. The polymer (MEH-PPV) was dissolved in DCM (5 or 35 mg in 6 mL of DCM in case of preparation of composites type **M**; 5, 15, 25 or 35 mg in 6 mL of DCM in case of preparation of composites type **R**). The corresponding Au/P3OT

weight ratios in composites type **M** were 7/1 and 1/1 which are hereafter denoted as **M₇** and **M₁**. Au/P3OT weights ratios in composites type **R** were 7/1, 2.3/1, 1.4/1 and 1/1 which are hereafter denoted as **R₇**, **R_{2,3}**, **R_{1,4}** and **R₁**, respectively.

Preparation of reference systems. (i) MEH-PPV/NaBH₄. Reference system containing the reducing agent and the polymer, without the metal salt, was prepared by mixing an aqueous solution of NaBH₄ (2.5 mL, 0.5 M) with the MEH-PPV solution in DCM (5, 15, 25 and 35 mg in 6 mL of DCM).

(ii) MEH-PPV/AuCl₄⁻(TOAB). The laboratory protocol described above for a preparation of nanocomposites **R₁** - **R₇** was followed up only until the polymer addition, i.e., NaBH₄ was not added. Samples (each 5 mL) were gradually taken from the reaction mixture at various reaction times, isolated as described above and subjected to SEC analyses.

3.3. Instrumentation and preparation of samples for the measurements

Generally, measurements of UV-Vis spectra and transmission electron microscopy (TEM) imaging were used for characterization of NPs sols and nanocomposites containing metal NPs in all chapters.

UV-Vis absorption spectra were recorded using a double beam Perkin Elmer Lambda 950 UV-Vis spectrometer. Samples in solutions were measured in a 1 cm quartz cuvette. A special holder with a 2 mm circular aperture was used for measurements of UV-Vis spectra of thin films of composites with P3OT (in Chapter 4.3.4). The polymer composite films containing metal NPs were prepared by spin-coating from the composite solutions in toluene (P3OT concentration: 0.3 wt %) on glass substrates.

Transmission electron microscopy (TEM) imaging was performed by a JEOL JEM200CX or TECNAI G2 SPIRIT (FEI, Czech Republic) transmission electron microscopes.

In the experiments described in Chapters 4.1. and 4.2., a small drop of hydrosols or composite systems in a particular stages of fragmentation (Chapter 4.1.) or aggregation process (Chapter 4.2.) was transferred onto a copper-mesh grid covered with a carbon foil and left to dry on air.

In Chapters 4.3. and 4.4., a small drop of metal organosols or composite solutions was transferred onto a copper grid covered by a carbon foil and after 15 s the drop was sucked off by a filtration paper.

Statistical evaluation of the NPs size distribution was performed by a commercial image processing and analysis computer program LUCIA 32 G Version 4.6, Laboratory Imaging Ltd.

Particle size distributions were calculated from the binary data image by a standard procedure using the *EqDiameter* (equivalent diameter) feature. The equivalent diameter is a size feature derived from the area of the object. It determines the diameter of circle having the same area as the corresponding object:

$$EqDiameter = \sqrt{\frac{4 \times Area}{\pi}}. \quad (16)$$

An exact separation of the particles in a binary image was necessary before using *EqDiameter* feature. Equivalent nanoparticle diameters obtained by TEM image analysis were statistically evaluated as mean value, standard deviation and median (in Chapter 4.3.2.2.) in Program Origin 8.

Fractal dimensions (D) of Ag NP aggregates were also determined from binary images of their TEM images according to the procedure published by Siiman et al.¹⁵¹: Fractal dimension D was calculated using the mass-radius relation:

$$M \sim R^D, \quad (17)$$

where M is the mass of the object of the size R . TEM micrographs used for the determination of the parameter D were covered by systems of centered squares. Assuming that all Ag particles have the same size, the number of particles in one square can be taken as the mass of the fractal object confined by the square of a particular size. The slope of the dependence of the number of particles versus the side-length of the square in double logarithmic plot thus represents the fractal dimension D of the Ag NPs assembly.

to Chapter 4.1.

The experimental arrangement used for the *in situ* monitoring of the laser fragmentation process is shown in Figure 3-2. The hydrosol containing Au NPs was placed in a four-sided quartz cuvette. An active Q-switched NdYAG laser system (Continuum Surelite I) equipped with a KDP crystal frequency doubler or tripler, respectively, was used as a light source for the fragmentation, providing pulses of 3 – 6 ns duration (FWHM) in a

repetition rate 10 Hz and yielding a maximum energy 170 mJ (532 nm) and 90 mJ (355 nm) per pulse, respectively, in the beam of a Gaussian shape with a cross section 66 mm^2 . The laser pulse energy was measured using power detector (Gentec PSV-103) equipped with a volume absorber. In order to achieve a homogeneous irradiation of the whole volume of the hydrosol in the cuvette, a quartz cylindrical lens was employed to produce the beam profile of an elliptical shape. The optical absorption of the hydrosol was measured *in situ* in the perpendicular direction to the fragmentation laser beam using a CCD fiber optics spectrophotometer Ocean Optics MC2000 equipped with two measuring UV-Vis and NIR channels and one reference channel and a combined deuterium-halogen light source DH2000. This experimental arrangement allowed to measure SPE spectra of Au hydrosols after each particular pulse.

TEM imaging was used for the *ex situ* characterization of Au hydrosols.

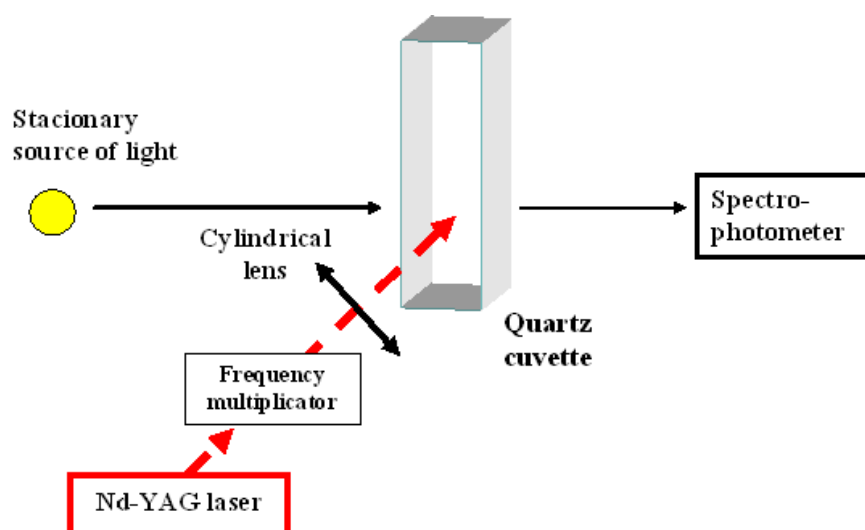


Figure 3-2. Experimental setup used for the laser fragmentation process. This arrangement allowed to measure SPE spectra of Au hydrosols after each particular pulse.

to Chapter 4.2.

SERS spectra of Ag/PEEP-I systems were measured from hydrosol systems placed in a 1 cm quartz five-window cuvette as well as from the Ag aggregates drop-cast on glass substrates. They were recorded with a Raman spectrometer equipped with a monochromator (1600 gr/mm grating, Jobin-Yvon-Spex 270M) and CCD detector (100x1340 pixels, Princeton Instruments). 90° scattering geometry was used. Excitation was provided with 441.6 nm line of a He-Cd laser (Liconix 4230N) or with 488.0 and 514.5 nm lines of an Ar^+ ion laser (Coherent, Innova 300). The average laser power at the sample was about

10 mW for a He-Cd laser line and about 150 mW for Ar⁺ ion laser lines. The spectra acquisition time was 150 s. A necessary post-acquisition spectra treatment was done by the SPECTRACALC program (Galalactic Industries Corp.). All preparations and measurements were made at room temperature.

Fluorescence spectra of the Ag/PEEP-I systems were measured in a 1 cm quartz cuvette using steady state fluorimeter SPEX Fluorolog 3-11.

to Chapter 4.3.

Scanning electron microscopy (SEM). SEM images were taken on thin films prepared by spin coating of nanocomposite solutions on a glass substrate. Images were obtained using SEM microscope Quanta 200 FEG (FEI, Czech Republic) equipped with a field emission gun, using a secondary electron detector. The accelerating voltage varied between 15 - 30 kV, spot size 1 - 3 μm and working distance between a sample and detector was about 10 mm. Exact values are given below each SEM image.

The elemental *energy dispersive analysis of X-rays (EDAX)* was performed on the same films as used for SEM with a Quanta 200 FEG microscope equipped with an EDAX detector.

Dynamic light scattering (DLS). The time correlation functions were measured at the scattering angle 173° on a Nano-ZS, Model ZEN3600 (Malvern, UK) zetasizer. The DTS(Nano) program was used for the data evaluation. The mean values of the positions of the size distribution peaks were taken to represent the data. Samples were measured in a 1 cm four-sided square quartz cuvette. Toluene was used as a dispersant in all measurements. The polymer concentration of the composite samples was below 0.1 wt %. Prior to the measurements, all samples were filtered through 0.45 μm PTFE filter except Ag(TDAB)/P3OT composite type **M** in which the presence of large aggregates was evident from TEM observation and using small filter pores would influence experimental results.

Raman spectra of Au/P3OT and Ag/P3OT composites were measured on thin films prepared as described above for UV-Vis spectroscopy. Raman confocal microscope (LABRAM HR-800, Horiba Jobin-Yvon) equipped with a CCD detector was used for measurements with 632.8 and 514.5 nm excitation wavelengths under the following experimental conditions: laser powers 0.2 mW for 514.5 nm excitation and between 0.1 – 2 mW for 632.8 nm excitation, entrance slit 100 μm , confocal aperture 400 μm . The spectral acquisition times were 60 s and 150 s for Au/P3OT and Ag/P3OT composites,

respectively. The spectra obtained with 441.6 nm excitation line of a He-Cd laser (Liconix 4230N) were recorded with a Raman spectrometer equipped with a monochromator (1600 gr/mm grating, Jobin-Yvon-Spex 270M) and CCD detector (100x1340 pixels, Princeton Instruments). 90° scattering geometry was used. The average laser power at the sample surface was about 3 mW. The spectral acquisition time was 300 s. All necessary mathematical spectra treatment was done using the SPECTRACALC program (Galalactic Industries Corp.). All preparations and measurements were made at room temperature.

to Chapter 4.4.

Raman spectra of Au/MEH-PPV composites were measured with Raman confocal microscope at 632.8 nm excitation wavelength under the same experimental conditions as written above in the Instrumentation to Chapter 4.3. (the spectra acquisition time was 150 s). The samples were prepared by a drop-casting of composite solutions onto a glass substrate.

Infrared spectra were recorded on powder samples using a Perkin-Elmer Paragon 1000 PC FTIR spectrometer equipped with a Specac MKII Golden Gate Single Reflection Diamond ATR System in the range 400 – 3600 cm^{-1} . IR spectra were obtained from 16 accumulated scans with a resolution 4 cm^{-1} .

Size-exclusion chromatography (SEC) analyses of Au/MEH-PPV composite solutions as well as neat polymer solutions were done using an HP 1100 Series HPLC instrument equipped with a diode-array UV-Vis detector (DAD) and a refractive index detector, a series mixed B, mixed C and mixed E columns (Polymer Laboratories, Bristol, UK) and THF as eluent (flow rate 0.7 mL/min). The system was calibrated using polystyrene standards with molecular weights (MWs) in the range from 365 to 2×10^6 (Polymer Laboratories, Bristol, UK).

Cyclic voltammetry was performed with a potentiostat (AMEL instruments, model 7050), using Pt working electrode, Pt counter electrode, and a saturated calomel electrode (SCE) as the reference electrode. The measurements were performed with 0.1 M tetrabutylammonium perchlorate in DCM as a supporting electrolyte. $\text{AuCl}_4^-/\text{TOAB}$ solution was prepared according to the laboratory protocol for a preparation of Au NP organosol until reductant addition. $\text{AuCl}_4^-/\text{TOAB}$ solution with five times excess of TOAB was prepared similarly as $\text{AuCl}_4^-/\text{TOAB}$ solution, only the concentration of TOAB was five times higher. In case of preparation of $\text{AuCl}_4^-/\text{TBAPC}$, TBAPC was used instead of TOAB. The solutions of $\text{AuCl}_4^-/\text{TOAB}$ and $\text{AuCl}_4^-/\text{TBAPC}$ for cyclic voltammetry measurements were prepared by addition of 1 mL of these solutions into 30 mL of DCM in a voltammetry cell.

SEM imaging and EDAX measurements were performed similarly as reported in Instrumentation to Chapter 4.3.

Fluorescence spectra of the Au/MEH-PPV composites **R₇** and **R₁** were measured in a 1 cm quartz cuvette using steady state fluorimeter SPEX Fluorolog 3-11, excitation wavelength was 500 nm. Low concentrations of MEH-PPV (1.7×10^{-4} wt %) in the composites enabled to exclude the effects of inner filter since the extinction of the composites samples was around 0.1.

4. RESULTS AND DISCUSSION

4.1. Interaction of high-power laser pulses with monodisperse Au NPs of various sizes

In this chapter, results of the investigation on the interaction of repetitive high-power nanosecond laser pulses with near-spherical Au NPs, dispersed in water and having various mean sizes are presented. The effects of the laser pulse fluence (Chapter 4.1.2.), laser wavelength (355 and 532 nm, Chapter 4.1.4.) and effect of the initial nanoparticle size (Chapter 4.1.4.) on fragmentation of Au NPs has been explored. The hydrosols obtained after the laser pulse impact were characterized by in-situ measurements of surface plasmon extinction (SPE) spectra and by TEM imaging. TEM images were analyzed for determination of nanoparticle size distribution in order to evaluate the morphological changes caused by the laser pulse impact. For elucidation and comparison of some of these effects, laser fluence has been adjusted in such a way that the same amount of energy per pulse was absorbed in the various parent Au hydrosols.

4.1.1. Parent Au hydrosols

Hydrosols containing Au NPs with mean diameters of 5, 11, 35 and 104 nm (as determined by TEM imaging and analysis) were used within the experiments. The values of the mean particle sizes determined by the image analysis confirmed that the synthesis yielded nanoparticles with the theoretically pre-calculated values within an error of 10%. The UV-Vis extinction spectra of the hydrosols are shown in Figure 4.1-1. The SPE of the NPs is clearly observed, with the maximum and the halfwidth of the extinction bands dependent on the NP size. The maxima of the SPE bands for the hydrosols with NP having the mean diameter of 5 (Au1), 11 (Au2), 35 (Au3), and 104 (Au4) nm were observed at 514, 519, 524, and 568 nm, respectively.

The relationship between the position of the SPE maximum and the mean particle diameter is plotted in Figure 4.1-2. The SPE maximum shows a systematic shift towards longer wavelengths with the increasing mean particle size, that is in agreement with theoretical calculations¹⁵² and previous experimental observations^{3, 10}. In the size interval 10 – 30 nm, the position of the SPE maximum does not change. For particle sizes below 10 nm, the shift of the SPE maximum towards lower wavelengths is observed. In particular, the results obtained in this study were compared to the SPE maxima positions of Au NPs prepared by El-Sayed³ who studied NPs within the same size range of 5 – 99 nm. A good

agreement between extinction spectra of the particles used within this study us and those prepared by El-Sayed was achieved (Figure 4.1-2).

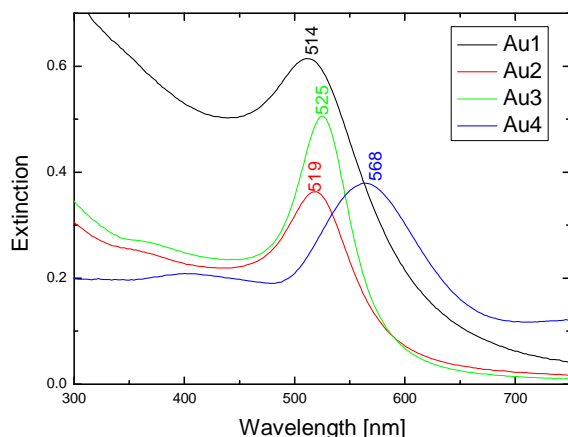


Figure 4.1-1. SPE spectra of Au1 – Au4 hydrosols.

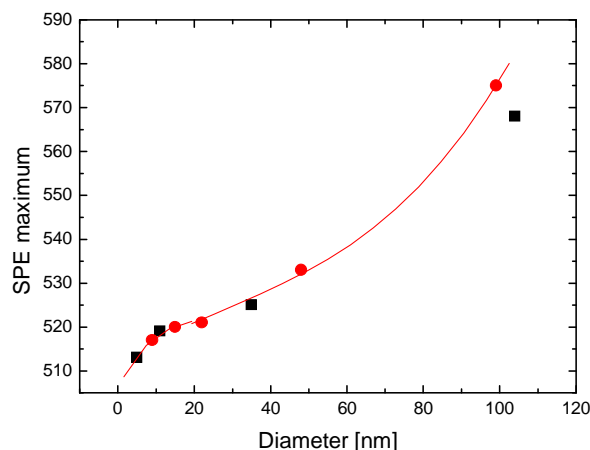


Figure 4.1-2. Comparison of the positions of the SPE maximum of Au sols Au1 - Au4 hydrosols (squares) and those of hydrosols reported in ref.³ (circles).

4.1.2. Effect of laser pulse fluence on fragmentation of Au NPs of various sizes

Extinction spectra of Au1 – Au4 hydrosols irradiated by 532 nm laser pulses of various fluences were measured in-situ after the impact of 1 pulse, 600 and 1800 pulses. The spectra for particular fluences are shown in Figure 4.1-3. For Au1 hydrosol, the spectrum of the parent sol does not change significantly during fragmentation with pulses of all used laser fluences. Only small decrease in extinction is observed after the impact of 1800 pulses at the highest laser fluence (205 mJ/cm²pulse). For Au2 hydrosol, the spectrum of the parent hydrosol does not change only during fragmentation with the pulses of the smallest laser fluence (45 mJ/cm²pulse). The pulses with higher laser fluences (86 and 205 mJ/cm²pulse) cause both the decrease in extinction and the shift of SPE maximum of the parent hydrosol. While the shift of SPE maximum of the parent sol is observed for the fluence of 86 mJ/cm² pulse after the impact of 1800 pulses, for the fluence of 205 mJ/cm²pulse the shift of SPE maximum is observed after the impact of a single pulse. For Au3 and Au4 hydrosols, the changes of SPE spectra of the parent sols are observed during fragmentation with laser pulses of all fluences. For Au3 sol, a decrease in extinction occurs even after the impact of 1800 pulses with the lowest laser fluence (45 mJ/cm²pulse). For fragmentation with the pulses of laser fluences higher than 45 mJ/cm²pulse the decrease in extinction intensity is accompanied by a shift of the SPE maximum. This shift occurs for the fluence of 86 mJ/cm²pulse after the impact of 600 pulses, for the fluence of 205 mJ/cm²pulse,

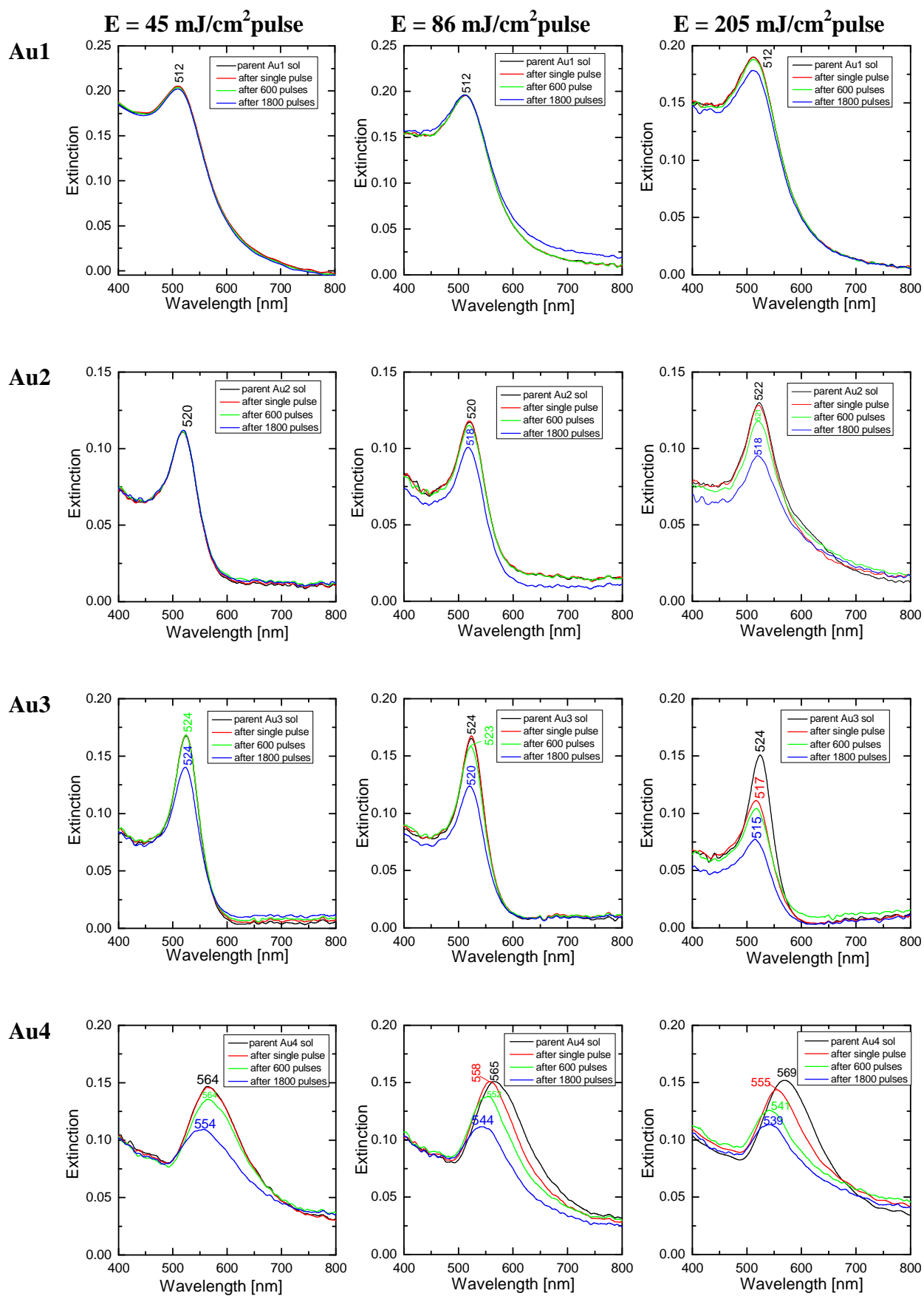


Figure 4.1-3. Time evolutions of in-situ measured SPE spectra of Au1-Au4 hydrosols after the impact of a single pulse, 600 pulses and 1800 pulses of 532 nm wavelength at various laser fluences.

a significant shift is observed after the impact of a single pulse. The most pronounced changes take place during fragmentation of Au4 hydrosol. A shift of the SPE maximum of the parent sol is observed after the impact of 1800 laser pulses of the lowest laser fluence (45 mJ/cm^2 pulse). With increasing laser fluence used for fragmentation of Au4 sol, the spectra change immediately after the impact of a single pulse and the effect on the extinction intensity and shift of SPE maximum grows with increasing laser fluence.

In Figure 4.1-4, the position of SPE maxima of the hydrosols after selected number of the impacted pulses is plotted as a function of laser fluence. The most pronounced changes in the SPE maximum position - from 567 to 522 nm - were observed for Au4 hydrosols after the impact of 1800 laser pulses at the highest laser fluence. For Au3 hydrosol, the changes of SPE maxima were noticeable after the impact of 1800 laser pulse at fluence higher than 45 mJ/cm^2 pulse, as shown in Figure 4.1-4. At the highest fluence, the shift from 524 to 515 nm was observed. Negligible changes in position of SPE maximum for Au1 and Au2 hydrosols were observed, which vary only within an experimental error of the used spectrophotometer.

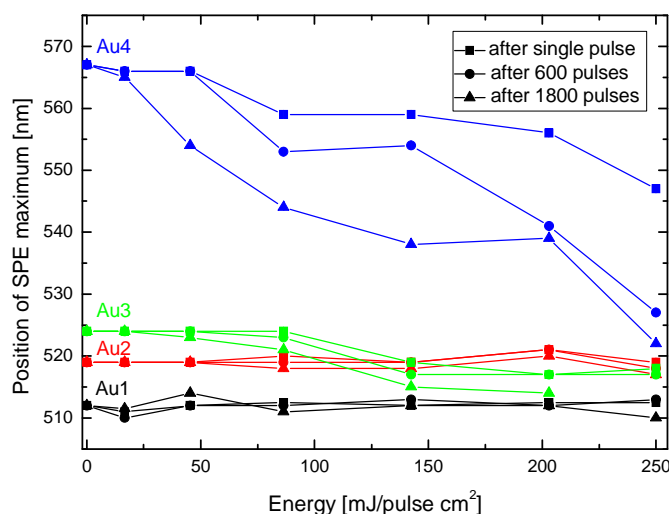


Figure 4.1-4. Dependence of the position of the SPE extinction maximum of Au4 (blue symbols), Au3 (green symbols), Au2 (red symbols), Au1 (black symbols) hydrosols on laser fluence after the impact of 1 pulse (squares), 600 pulses (circles), 1800 pulses (triangles). Laser wavelength 532 nm.

From the results described above it is obvious that the changes in SPE spectra of the hydrosols during fragmentation with laser pulses of various fluence, in particular the shift of the SPE maximum with increasing number of impacted laser pulses of a particular energy, is proportional to the size of the NPs. According to the relation between NPs size and position

of the SPE maximum in Figure 4.1-2, the spectral changes observed for both Au4 and Au3 hydrosols correspond to a size-reduction of Au NPs. Furthermore, it appears that for the Au3 and Au4 hydrosols the process of laser fragmentation is cumulative with the increasing number of subsequent pulses: for longer time of the fragmentation the shift in SPE maximum position starts to appear at lower laser fluence. For Au1 and Au2 hydrosols the prediction about the size reduction is not so simple as for Au3 and Au4 hydrosols because of the very low sensitivity of the SPE maximum to the changes of NPs size for diameters 10 - 30 nm (see Figure 4.1-2). Therefore, TEM imaging and image analysis of the resulted deposited hydrosols were done for determination of the NP sizes. The image analysis of the Au NPs found in the Au2 – Au4 hydrosols after the impact of 1800 pulses at fluence 250 mJ/cm^2 pulse showed that the resulted hydrosols contain the particles with the same mean particle size of about 6 nm. On the other hand, the irradiation of Au1 hydrosol at the same laser fluence led to a slight increase of the NP diameter (from initial 5 nm to about 7 nm).

4.1.3. Effect of initial Au NPs sizes on their fragmentation with laser pulses of normalized fluences

The following experiment was designed to elucidate the effect of the initial size of the NPs on their final size distribution after fragmentation. Au1 - Au4 hydrosols, containing particles with various mean diameters, were irradiated by laser pulses of the same wavelength (532 nm). The respective normalized laser fluences used for the fragmentation were calculated from the optical absorption of the hydrosols at this particular wavelength to provide the same absorbed energy per pulse in the hydrosol, all other conditions were kept constant. The exact value of optical absorption could not be calculated simply from the measured optical transmission of the hydrosol because, besides the optical absorption, also scattering contributes to the extinction coefficient. To know the amount of energy absorbed in the hydrosol correctly, we measured the diffusion transmission and diffusion reflection of hydrosols using an integrating sphere. Compared to the values obtained using normal transmission-mode measurements, the real absorbed energy was only between 70 to 90 %.

SPE spectra were measured in-situ during the course of the fragmentation process. Figure 4.1-5 shows the extinction bands of Au1 – Au4 hydrosols after the impact of a single pulse and 1800 pulses, respectively, for the laser fluences corresponding to the absorbed energy of 41 mJ/cm^2 pulse in the tested volume of the hydrosols. Observable spectral changes in extinction of Au3 and Au4 hydrosols were detected after a single pulse. Typically, we see a broadening of the bands, a decrease in extinction and a characteristic blue shift. In the case of

Au3 the extinction maximum shifts from 525 to 516 nm and for Au4 from 563 to 537 nm after the impact of a single pulse. After the impact of 1800 laser pulses the most marked change in the position of maximum was observed for Au4 hydrosol where the maximum shifts from 563 to 514 nm after 1800 pulses. Because the positions of SPE maximum of all sols shifted to values less than 519 nm after the impact of 1800 pulses, we expect similar composition of all the final products of fragmentation having NPs with diameters below 20 nm.

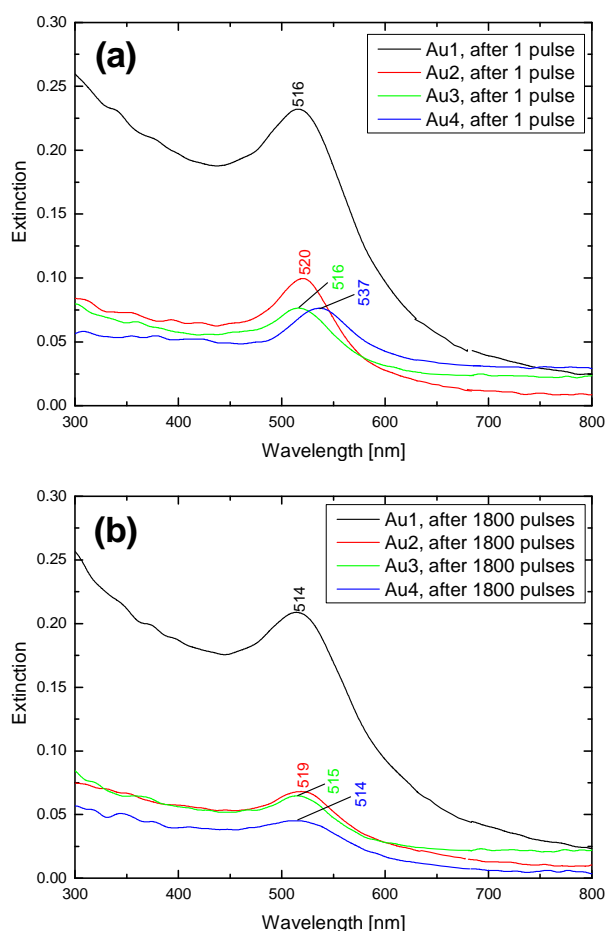


Figure 4.1-5. In-situ measured extinction spectra of Au1 – Au4 hydrosols after the impact of (a) a single pulse and (b) 1800 pulses of 532 nm wavelength. The normalized laser fluences were 151, 248, 270 and 245 $\text{mJ}/\text{cm}^2/\text{pulse}$ for Au1 – Au4 hydrosols, respectively, to provide the same absorbed energy.

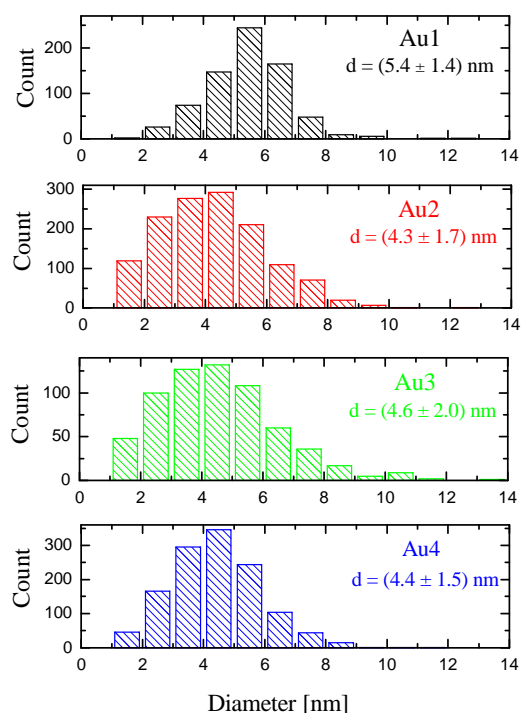


Figure 4.1-6. Nanoparticle size distributions of Au1 – Au4 hydrosols after the impact of 1800 laser pulses of 532 nm wavelength. The normalized laser fluences were 151, 248, 270 and 245 $\text{mJ}/\text{cm}^2/\text{pulse}$ for Au1 – Au4 hydrosols, respectively.

The NP size distributions obtained from the analysis of the TEM images of the final products are shown in Figure 4.1-6. Remarkable differences between the behavior of Au2 – Au4 hydrosols on one side and Au1 on the opposite were observed. Size distributions indicate that the fragmentation of all Au2 – Au4 sols provides small particles with mean size

about 5 nm, particles larger than 10 nm were not observed except of a few particles in the final Au3 hydrosol. Surprisingly, the distribution of diameters of NPs found in the Au1 hydrosol after the fragmentation was slightly shifted towards larger values after irradiation. The measurements performed at the same energy absorbed in the hydrosols thus confirm the conclusions obtained from the measurements at the highest available laser fluence (previous chapter). All initially large NPs end up with the same size but, if the fragmentation starts with already small NPs having the diameter below a certain value, the NPs tend to small but detectable growth.

4.1.4. The effect of laser pulse wavelength on fragmentation of Au NPs of various sizes

To elucidate whether the fragmentation process is wavelength selective, the fragmentation was performed by laser pulses of two wavelengths, 355 and 532 nm, respectively, while all the other conditions were kept constant. The energy per pulse used for the fragmentation was again calculated on the basis of different extinction coefficients at the respective wavelengths. The laser fluence was adjusted so as the same amount of energy per pulse was absorbed by the NPs at both wavelengths. In-situ measured SPE spectra of Au1 – Au4 hydrosols after the impact of a single pulse, 600 pulses and 1800 laser pulses are compared in Figure 4.1-7. SPE spectra of the hydrosols Au1 and Au2 do not significantly change upon laser irradiation at both wavelengths. The shifts of SPE maximum are not observed, only a decrease in extinction intensity occurs. While for Au1 sol this decrease is observed after the impact of 1800 laser pulses, for Au2 sol the decrease occurs after the impact of 600 pulses. The impact of a single pulse of 355 nm wavelength on the hydrosols Au3 and Au4 causes a blue shift of SPE maxima (see Figure 4.1-7). On the other hand, the impact of a single pulse of 532 nm wavelength does not change the spectra of the parent hydrosols. With increasing number of impacted laser pulses, blue shifts of SPE maxima are observed at both wavelengths of laser pulses. After the impact of 1800 laser pulses, the Au3 hydrosols with nearly identical SPE spectra are obtained for both fragmentation wavelengths. Impact of 1800 laser pulses of 355 and 532 nm wavelengths influences the SPE spectra of the hydrosol Au4 by different ways. More pronounced shift of SPE maximum is observed for 532 nm fragmentation wavelength (from 561 to 541 nm) compared to the shift from 562 to 553 nm for 355 nm fragmentation wavelength. This blue shift of the peak position is analogous to that reported in⁴⁸, however, in that case, it has been ascribed to changes not only in size, but also in the shape of the initially non-spherical particles.

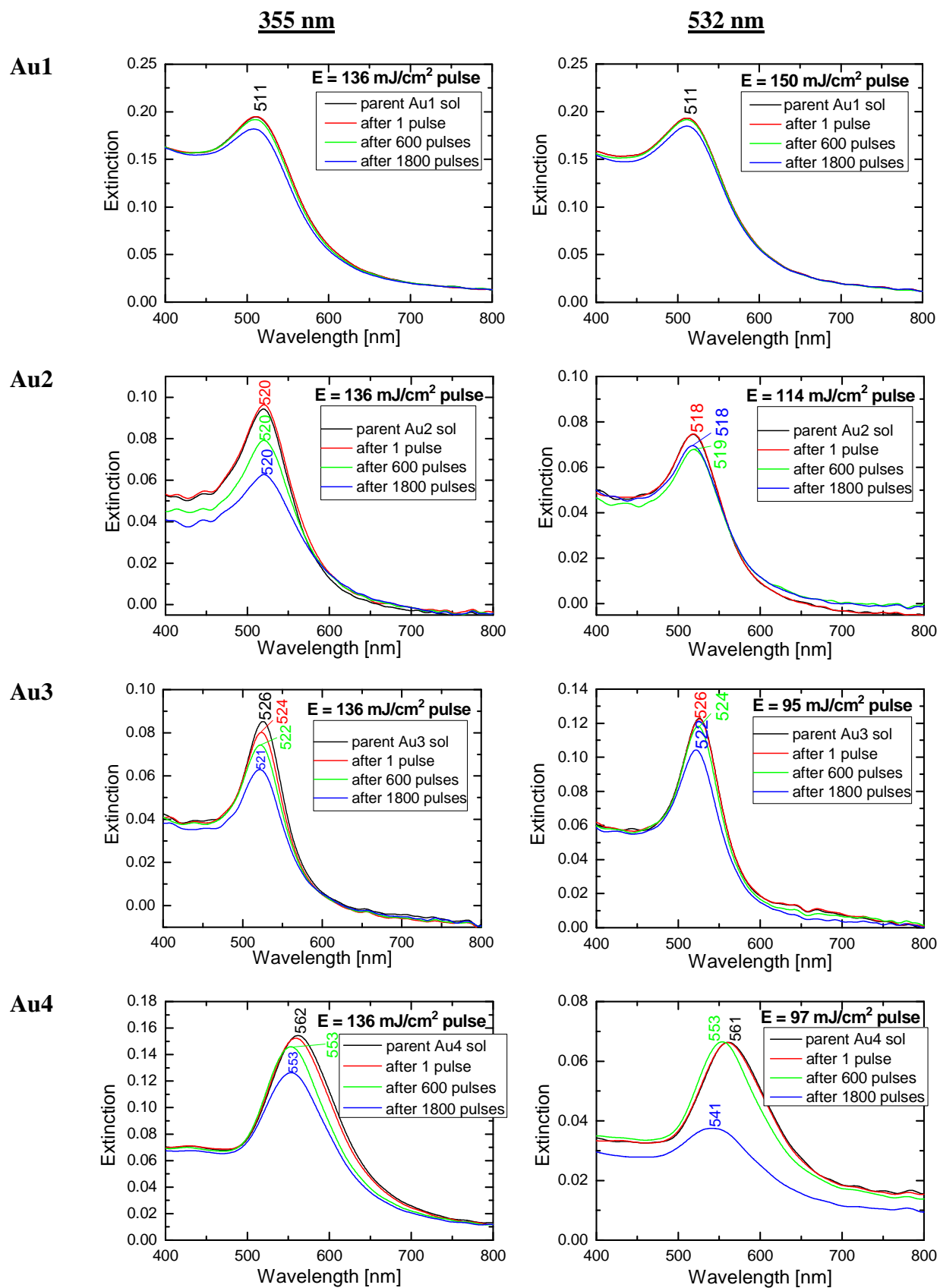


Figure 4.1-7. In-situ measured SPE spectra of the parent Au1 – Au4 hydrosols and sols after the impact of a single pulse, 600 pulses and 1800 pulses of 355 and 532 nm wavelength. The spectra were smoothed by FFT filtering in program Origin 8.

TEM images of the Au NPs were acquired (Figure 4.1-8a,b - Figure 4.1-11a,b) and analyzed for the size distributions to assess the morphological changes caused by laser irradiation by 1800 pulses. At least 700 particles were counted for the image analysis of each sample. The corresponding size distributions are shown in Figure 4.1-8c,d - Figure 4.1-11c,d. The analyses of all hydrosols (Au1 – Au4) showed that the fragmentation by laser pulses at the 355 nm wavelength yields NPs with narrower size distributions and smaller values of particle mean size compared to that performed by 532 nm laser pulses.

For Au2 hydrosol, the initial monomodal size distribution turned into a bimodal one after the irradiation with 1800 pulses of 532 nm wavelength (Figure 4.1-9d). Bimodal size distributions of Au NPs under nanosecond⁵³ and picosecond⁵⁰ laser pulses, centered at 2 – 6 nm and the other at 8 – 14 nm, respectively, separated with a well pronounced “valley” at 7 – 8 nm were reported recently. The larger particles were ascribed to be “parent” particles with reduced size, the smaller ones were suggested to be a product of the material evaporated from the “parent” particle heated by the laser pulse impact. The bimodal size distribution observed in ref.⁵⁰ was interpreted as a transient phenomenon that can be seen before the completion of the size reduction of initial particles into small ones. The bimodal particle size distribution after the irradiation by 532 nm pulses was not observed for Au3 (Figure 4.1-10d) and Au4 (Figure 4.1-11d) hydrosols. Nanoparticle size distributions of fragmented particles Au3 and Au4 consist of a large fraction of small particles (diameter less than 10 nm) and a small fraction of larger particles (diameter above 10 nm) shown as a tail in the size distribution diagram. Although the mean sizes of particles Au3 and Au4 are similar, they differ slightly in the width of their size distributions. The fragmented Au3 hydrosol contains a small fraction of the “parent” particles with diameters corresponding to the diameters of the initial particles around 35 nm. In the fragmented sol Au4 “parent” particles with the diameter equal to the diameter of initial particles do not occur. On the other hand, a fraction of larger particles with diameter between 15 - 25 nm are observed in TEM image and NPs size distribution. “Parent” particles which are observed in TEM images of the fragmented Au2 and Au3 hydrosols could be considered as non-fragmented particles of the parent hydrosols.

A careful analysis of these NPs shows a shape transformation during the fragmentation. Parent particles with the sharp edges change into particles with a near-spherical shape. The shape transformation of Au NPs was investigated in several studies^{48, 50, 57, 61, 153-155}. Inasawa et al.¹⁵³ calculated the threshold energy for the shape transformation of relatively large Au particles (mean diameter 38 nm). They used 355 nm pulses with energy 2 - 8 mJ per pulse and pulse width 30 ps. The shape transformation was

explained by surface melting. This situation can occur when the laser pulse energy is not high enough to heat the whole volume of the nanoparticle above its melting point. The structural transition of Au NPs before and after the shape transformation was also discussed by Koga et al.¹⁵⁶ According to these study the mechanism of size and shape transformation, i.e. whether it proceeds via melting (as in the case of larger near-spherical “parent” particles) or via fragmentation (small particles with diameter less than 10 nm), simply depends on the amount of laser energy absorbed within a nanoparticle in a single pulse⁵³.

TEM images and nanoparticle size distributions of Au2 – Au4 hydrosols after the impact of 1800 laser pulses of 355 nm wavelength depicted in Figure 4.1-8a,c - Figure 4.1-11a,c are similar to each other and the values of particle mean size differ only within an experimental error. The statistical analysis further showed the narrow monomodal size distribution of all fragmented hydrosols with particle mean sizes around 4 nm. The fragmented hydrosols contain small near-spherical particles, while particles with diameters above 10 nm are not observed compared to the presence of these particles in the hydrosols after irradiation with 532 nm laser pulses. Probably, the size of some of the photoproducts (e.g. Au clusters) is smaller than the detection limit of transmission electron microscope, which in this case was typically between 1 and 2 nm for samples deposited on a flat carbon coated grid.

Nanoparticles size distribution of Au NPs in Au1 hydrosol after the impact of 355 nm laser pulses (Figure 4.1-8c) was narrower than size distribution after the impact of 532 nm pulses (Figure 4.1-8d) for the same energy per pulse absorbed in the hydrosol at both wavelengths. Also the mean diameter of particles after 355 nm was smaller ($d = 3$ nm) than the mean size after laser irradiation at 532 nm ($d = 6$ nm). These results confirm that 355 nm laser pulses provide smaller particles than 532 nm laser pulses, regardless the initial NPs sizes. These results indicate the differences in fragmentation mechanism by using 355 and/or 532 nm pulses. For NP fragmentation with nanosecond laser pulses, two processes were proposed; one is the vaporization of particles induced by a photothermal process in which particles vaporize at the boiling point, and the other is a kind of Coulomb explosion of particles induced by an electron ejection from particles.

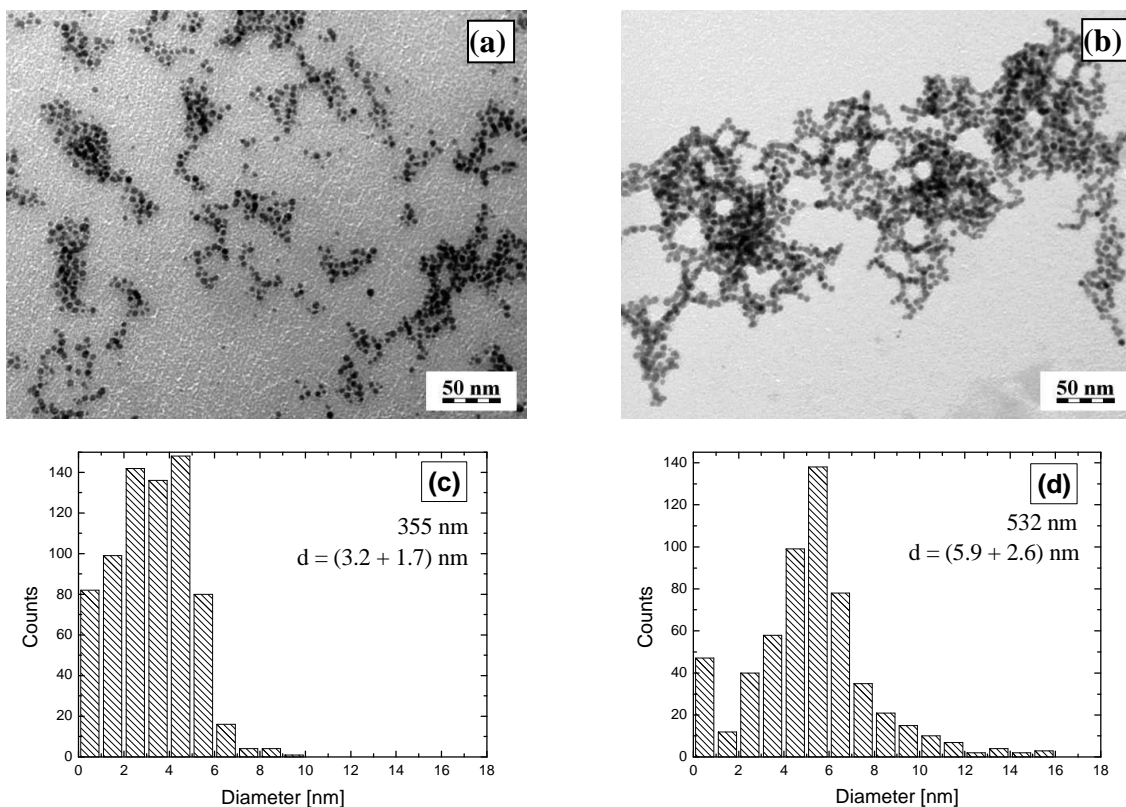


Figure 4.1-8. TEM images (a,b) and nanoparticles size distributions (c,d) of Au NPs in Au1 hydrosol after the impact of 1800 pulses of 355 nm (a,c) and 532 nm (b,d) wavelength. The laser fluences were 136 and 150 mJ/cm^2 pulse for 355 and 532 nm wavelength, respectively.

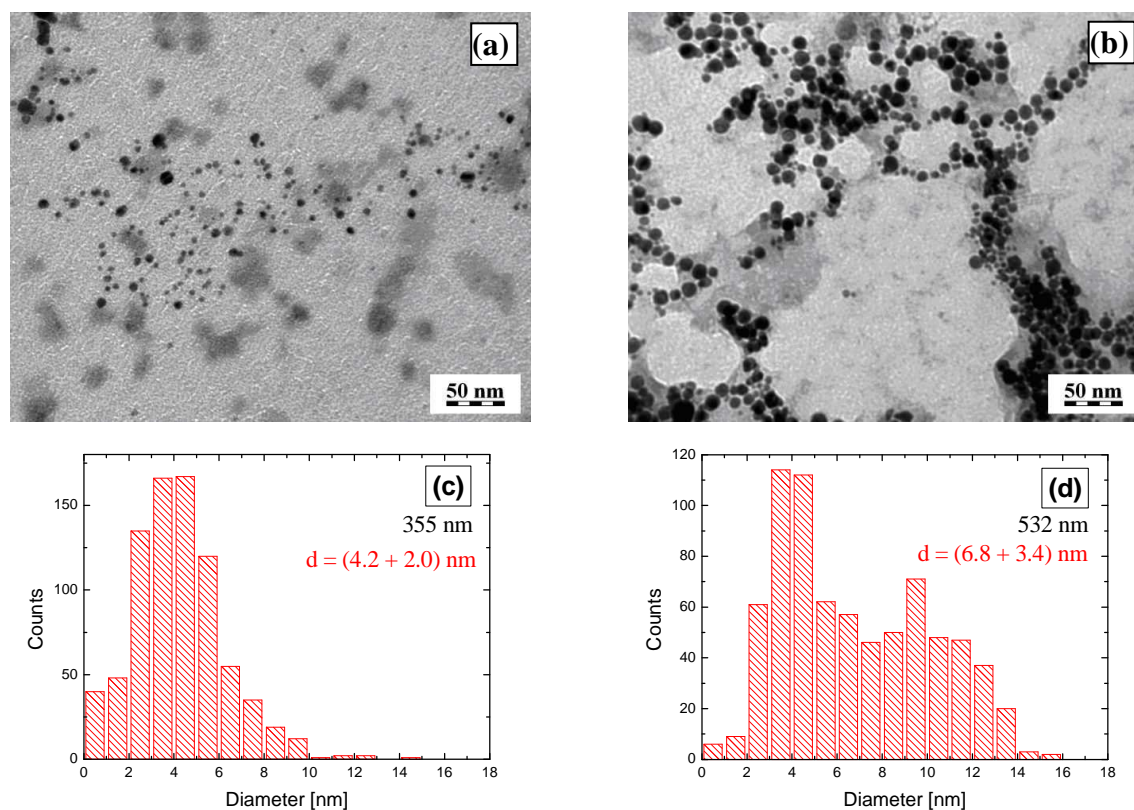


Figure 4.1-9. TEM images (a,b) and nanoparticles size distributions (c,d) of Au NPs in Au2 hydrosol after the impact of 1800 pulses of 355 nm (a,c) and 532 nm (b,d) wavelength. The laser fluences were 136 and 114 mJ/cm^2 pulse for 355 and 532 nm wavelength, respectively.

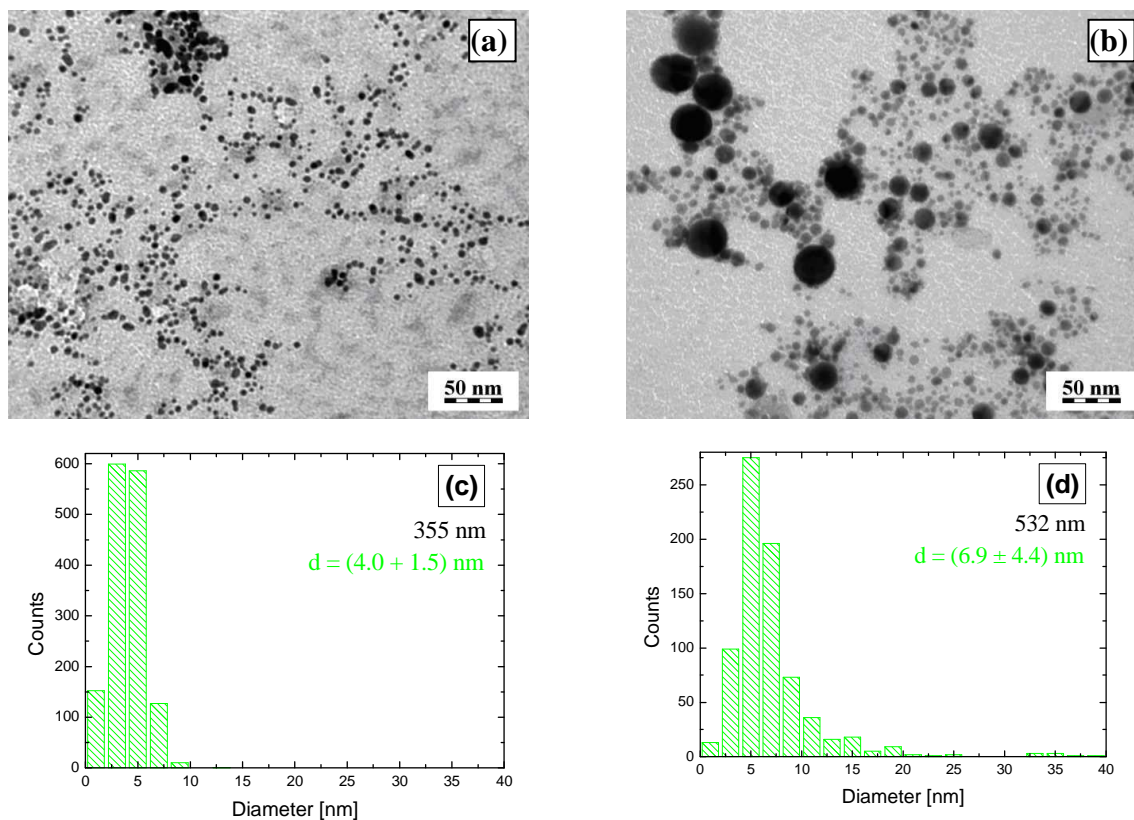


Figure 4.1-10. TEM images (a,b) and nanoparticles size distributions (c,d) of Au NPs in Au₃ hydrosol after the impact of 1800 pulses of 355 nm (a,c) and 532 nm (b,d) wavelength. The laser fluences were 136 and 95 mJ/cm²/pulse for 355 and 532 nm wavelength, respectively.

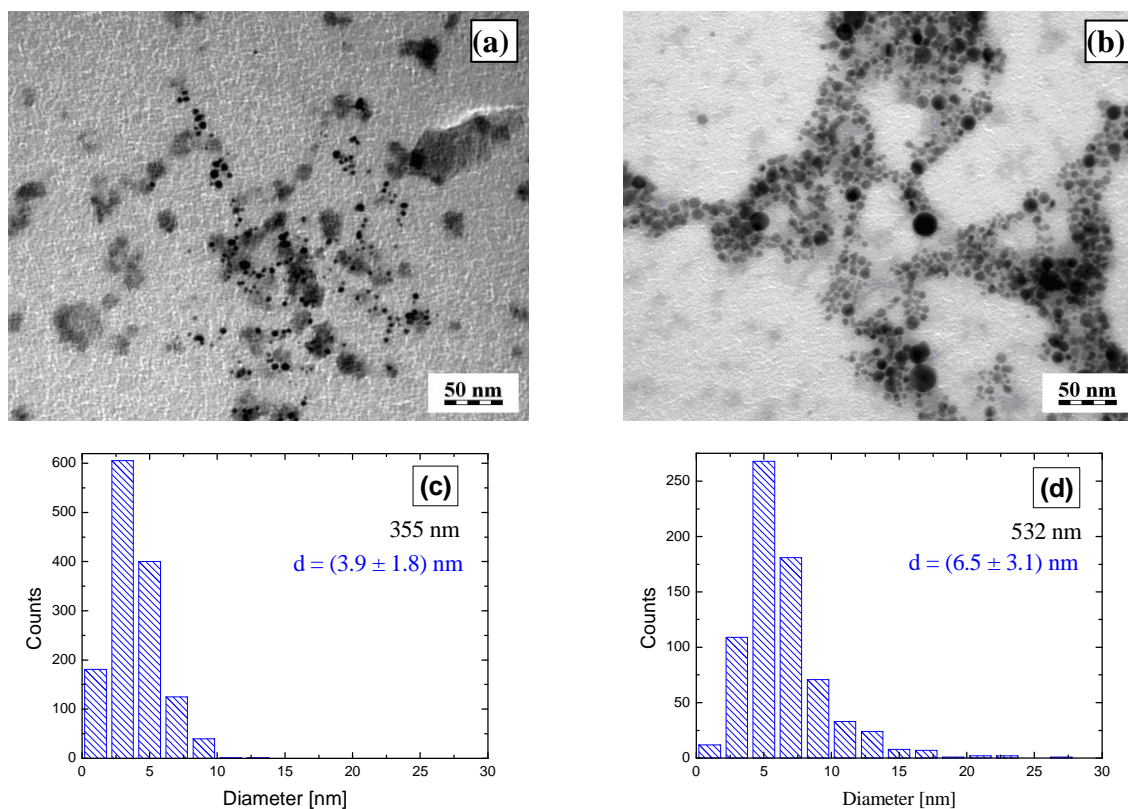


Figure 4.1-11. TEM images (a,b) and nanoparticles size distributions (c,d) of Au NPs in Au₄ hydrosol after the impact of 1800 pulses of 355 nm (a,c) and 532 nm (b,d) wavelength. The laser fluences were 136 and 97 mJ/cm²/pulse for 355 and 532 nm wavelength, respectively.

4.1.5. Discussion of Au NPs fragmentation mechanisms

In order to discuss the mechanism of fragmentation one has to consider the time scale of light absorption, heating of the material and exchange of the thermal energy with the surrounding medium. As the heating of the NPs upon light energy absorption is given by the phonon-phonon relaxation time and it is in the time scale of 100 ps, in experiments in which the nanosecond pulses are used the hot molten spheres are continuously bath with light from the nanosecond laser pulse. These hot particles continue to absorb on the nanosecond time scale of the pulse and also lose some heat to the solvent simultaneously^{53, 155}. It has been reported that during a single laser pulse, one parent Au NP absorbs consecutively more than thousands photons, and its temperature can easily reach the boiling points of the metal. The heated parent Au NPs release photofragments and Au atoms which aggregate into small Au clusters on a nanosecond time scale. The Au clusters begin to contribute to the optical absorption as they grow into nanosized particles by aggregation and/or attachment to the already formed NPs. Under certain conditions, very large NP aggregates (nanonetworks) and larger NPs can be formed by interparticle fusion⁵⁹. However, neither aggregation nor interparticle fusion was observed in this study.

The competition between heating of the NP by absorbed photons and heat dissipation from the hot molten particle to the medium plays an important role in its size reduction¹⁵⁵. It was shown that the rate of energy dissipation for Au NPs in an aqueous solution depends on their size; smaller particles show faster thermal relaxation times because of their higher surface-to-volume ratio¹⁵⁷. Therefore, for smaller particles, either present in the parent hydrosol or formed by a size reduction during the precedent fragmentation, there is a lower probability of further reduction of their sizes, because these particles are not heated to enough high temperature due to their lower optical absorption and due to a fast heat dissipation (heat dissipation within 10 ps for NPs with the diameter 4 nm). If the heat dissipation from larger particles to the medium proceeds in a longer time scale as estimated in the paper by Inasawa and coworkers⁵⁰, the high temperature of a particle could be maintained if nanosecond laser pulses of sufficient energy are used. The delivery of energy within the nanosecond laser pulses could overcompensate the amount of energy lost to the solvent and, therefore, the creation of small spheres by fragmentation can be thus explained. This is quite realistic if it is considered that the cooling process could be even retarded due to the presence of water vapours shell around the nanoparticles, instead of a liquid medium⁵⁰. Vapours are developed by a temporal excess of thermal energy during the fragmentation.

4.1.6. Conclusions

1. The process of laser-induced fragmentation of Au NPs is cumulative with increasing number of subsequent laser pulses.
2. Laser irradiation of all parent Au NP hydrosols containing NPs with different mean diameters (except that one containing NPs with the mean diameter 5 nm) by pulses of 532 nm wavelength and of the same energy per pulse absorbed in the hydrosol, resulted in hydrosols containing NPs of a very similar mean size and size distribution. On the other hand the parent NPs with a mean diameter below 5 nm had a tendency to a slight, but still observable growth during the fragmentation at the same wavelength.
3. Comparison of fragmentations with the pulse energy adjusted in such a way that the energy per pulse absorbed in the hydrosols was the same for both wavelengths (355 and 532 nm) showed that the fragmentation at 355 nm wavelength led to final hydrosols with lower mean particle size and narrower size distribution in comparison to those obtained by irradiation with 532 nm pulses. Under the same conditions and using laser pulses of 532 nm, the irradiation of all the hydrosols containing NPs with the original diameter larger than 10 nm resulted into the final hydrosols containing NPs of a very similar mean size ($d \sim 7$ nm). The NPs of a mean diameter 5 nm were not fragmented by pulses of 532 nm wavelength. On the other hand, the impact of 1800 laser pulses of 355 nm wavelength led to the formation of NPs of the same size in all the hydrosols ($d \sim 4$ nm).

4.2. Morphology and optical responses of SERS active π -conjugated poly(N-ethyl-2-ethynylpyridinium iodide)/Ag nanocomposite systems

In this chapter, designing and probing of SERS active-nanocomposite systems consisting of poly(N-ethyl-2-ethynylpyridinium iodide), PEEP-I (Figure 4.2-1), and Ag NPs is reported. The effect of the changes in the morphology of nanocomposite systems (as determined by TEM) on their optical characteristics was investigated by a combination of surface plasmon extinction (SPE) measurements, surface-enhanced Raman spectroscopy (SERS) and fluorescence spectroscopy. The SERS spectra measurements have been focused on optimization of the polymer concentration for the preparation of Ag/PEEP-I SERS active system as well as on the selection of the excitation wavelength providing the highest SERS enhancement.

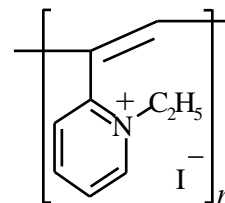


Figure 4.2-1. Chemical structure of poly(N-ethyl-2-ethynylpyridinium iodide), PEEP-I.

4.2.1. SPE spectra of Ag/PEEP-I hydrosol systems with various polymer concentration

The UV-Vis spectrum of the pure polymer dissolved in water (Figure 4.2-2) shows a strong absorption centered at 440 nm resulting from the $\pi \rightarrow \pi^*$ transition of the conjugated polymer backbone. Assuming the relationship of the UV-Vis absorption maxima versus conjugation length for unsubstituted polyenes¹⁵⁸, the effective conjugation length of this polymer is around 9. The shoulders at 268 and 286 nm can be associated with the aromatic $\pi \rightarrow \pi^*$ or $n \rightarrow \pi^*$ transitions of pyridine or pyridinium, respectively. It indicates that the prepared polymer contains both the protonated and non-protonated pyridines.

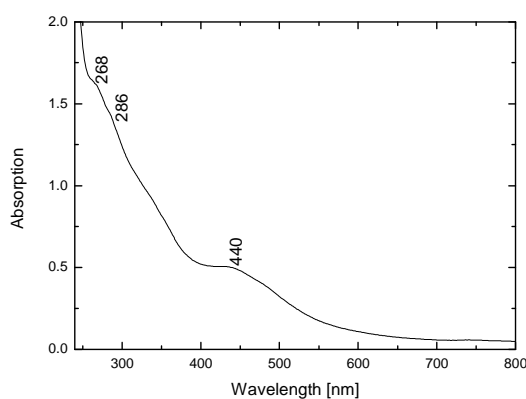


Figure 4.2-2. UV-Vis spectrum of PEEP-I aqueous solution, $c_{\text{PEEP-I}} = 3 \times 10^{-4}$ M.

The time evolutions of SPE spectra of the Ag hydrosol after the addition of PEEP-I at various concentrations are shown in Figure 4.2-3. Upon addition of the polymer strong color changes were observed, depending on the concentration of the polymer in the composite

system. For understanding the spectra, it should be noted that the absorbance of the polymer at the maximum concentration of 1×10^{-4} M used in the experiments was only 10 % of the extinction of the Ag hydrosol and, therefore, the contribution of the absorbance of the polymer to the overall extinction was almost negligible for the polymer concentrations used within this study. Therefore, the spectra of the composites are expected to reflect entirely the changes in the SPE spectrum of the Ag hydrosol. The SPE spectral features for systems with the particular polymer concentrations will be now discussed.

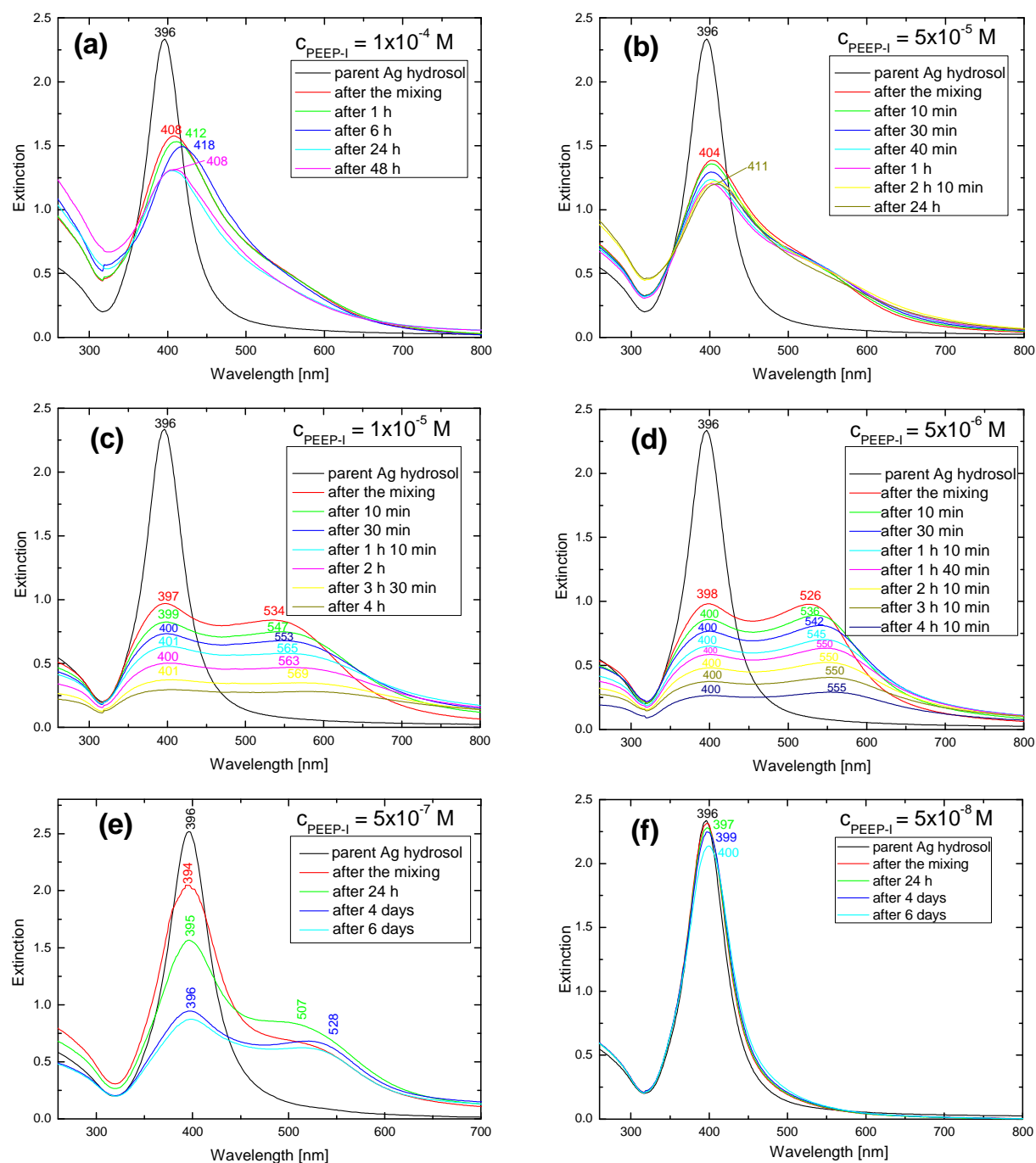


Figure 4.2-3. Time evolutions of SPE spectra of Ag/PEEP-I composite systems with (a) 1×10^{-4} M, (b) 5×10^{-5} M, (c) 1×10^{-5} M, (d) 5×10^{-6} M, (e) 5×10^{-7} M and (f) 5×10^{-8} M PEEP-I concentration.

The time evolution of SPE spectra of Ag/PEEP-I hydrosol system with the polymer concentration 1×10^{-4} M is shown in Figure 4.2-3a. After the polymer addition, the intensity of SPE band decreased, the band red-shifted to 408 nm and markedly broadened compared with the spectrum of the parent Ag hydrosol. With increasing time, the red-shift of SPE band continued to 418 nm 6 hrs after the mixing. However, at long time (48 hours after the mixing) the SPE maximum returned to 408 nm and, simultaneously, the extinction above 700 nm slightly increased. Similar evolution of SPE spectra exhibited Ag/PEEP-I hydrosol system with the polymer concentration 5×10^{-5} M (Figure 4.2-3b). Compared to SPE spectra of the system with the polymer concentration 1×10^{-4} M, the spectra contained a more pronounced secondary band with a maximum at about 530 nm. The SPE spectra did not show any significant changes in spectral features within 4 hrs after the mixing. A day after the mixing, SPE band shifted to 411 nm. Finally, it should be mentioned that both systems were stable since no visible aggregates were observed at the bottom of the vial during a week after the mixing.

Different behavior was observed when the PEEP-I concentration in the systems was in the range 1×10^{-5} M - 5×10^{-6} M. Time evolutions of SPE spectra of Ag/PEEP-I hydrosol systems with the polymer concentration 1×10^{-5} M and 5×10^{-6} M are depicted in Figure 4.2-3c and d, respectively. For example, in the case of the composite system with 5×10^{-6} M polymer concentration a decrease in extinction of SPE band and its slight red shift (from 396 nm to 398 nm) together with a development of a new broad band centered at 526 nm (Figure 4.2-3d, red line) were observed immediately after the mixing. With increasing time, the new band at the longer wavelength was broadened and red-shifted, showing a maximum at 545 nm about 70 min after the mixing. During further observation the intensity of the whole SPE spectrum decreased, while keeping the ratio of both bands unchanged. These changes of the SPE band of Ag hydrosol occurring immediately after the preparation indicate a rapid aggregation of Ag NPs. Aging of the system (in terms in hours) led to a decrease in the overall optical extinction, that was attributed to the formation of large aggregates and their sedimentation at the bottom of the vials. Comparing the observed extinction spectra with calculated optical responses of fractal aggregates²⁶, the optical spectra evolutions of these system can be explained by the formation of aggregates that might even show fractal features.

The time evolution of SPE of the Ag/PEEP-I hydrosol system containing 5×10^{-7} M polymer concentration is shown in Figure 4.2-3e. Although the spectra showed similar features as in the previous case for the higher polymer concentration (5×10^{-6} M), a slower progression of the spectral changes was recorded. After the preparation, the spectrum

consisted of the SPE band, with the maximum position similar to that of the parent Ag hydrosol (at 394 nm), and a shoulder around 500 nm. With increasing time, the SPE band at 394 nm gradually decreased and, simultaneously, the extinction intensity of the band around 500 nm increased. The fourth day after the preparation both bands had nearly the same extinction with maxima positioned at 396 and 528 nm. During further observation the intensity of the whole SPE spectrum decreased, while keeping the ratio of both bands unchanged. The increased extinction above 700 nm agrees well with the presence of large aggregates that have the tendency to sedimentation.

SPE spectra of Ag/PEEP-I hydrosol systems containing even lower polymer concentration than 5×10^{-7} M preserve the characteristics of the parent Ag hydrosol as is shown in Figure 4.2-3f for PEEP-I concentration 5×10^{-8} M. Only a small broadening and red-shift of the SPE band are observed with increasing time. Nevertheless, the system is stable for a long time (within weeks) and no aggregates are observed.

4.2.2. TEM imaging of Ag/PEEP-I hydrosol systems and determination of fractal dimension (D)

The characteristic morphologies of Ag/PEEP-I hydrosol systems deposited from sols containing various polymer concentrations immediately after their preparation are shown in Figure 4.2-4. It is obvious that the morphology of Ag NPs in the Ag/PEEP-I system with polymer concentration 1×10^{-4} M differs significantly from that observed for the systems with lower polymer concentration. TEM image of this system (Figure 4.2-4a) shows that smaller aggregates are formed in which Ag NPs are well separated from each other. Interparticle spacing is larger compared to the systems containing lower polymer concentration.

For the Ag/PEEP-I systems containing polymer concentration lower than 5×10^{-5} M (Figure 4.2-4b and c), large aggregates consisting of nanoparticles with an average size about 9 nm (corresponding to the average size of nanoparticles in the parent Ag hydrosol) are observed. The nanoparticles in these aggregates form closely packed arrays which mutually overlay as can be seen on some places of the TEM image.

Ag/PEEP-I system containing polymer concentration 5×10^{-6} M was chosen for determination of fractal dimension since SPE spectra of this system taken immediately after the preparation are similar to those observed for fractal aggregates²⁶. Fractal dimensions (D) were determined from three different TEM images by a procedure based on the mass-radius relation according to the method described by Solecká¹⁵⁹ (see also Experimental, Chapter 3.3.). Briefly, TEM images were covered by sets of centered squares with three different

central points selected on each of them. Assuming that all silver nanoparticles have the same size, the number of particles in one square can be taken as the mass of the fractal object while the length of the side of the square is taken as its size. The slope of the dependence of the number of particles versus the side-length of the square in double logarithmic plot thus represents the fractal dimension D of the Ag NP assemblies.

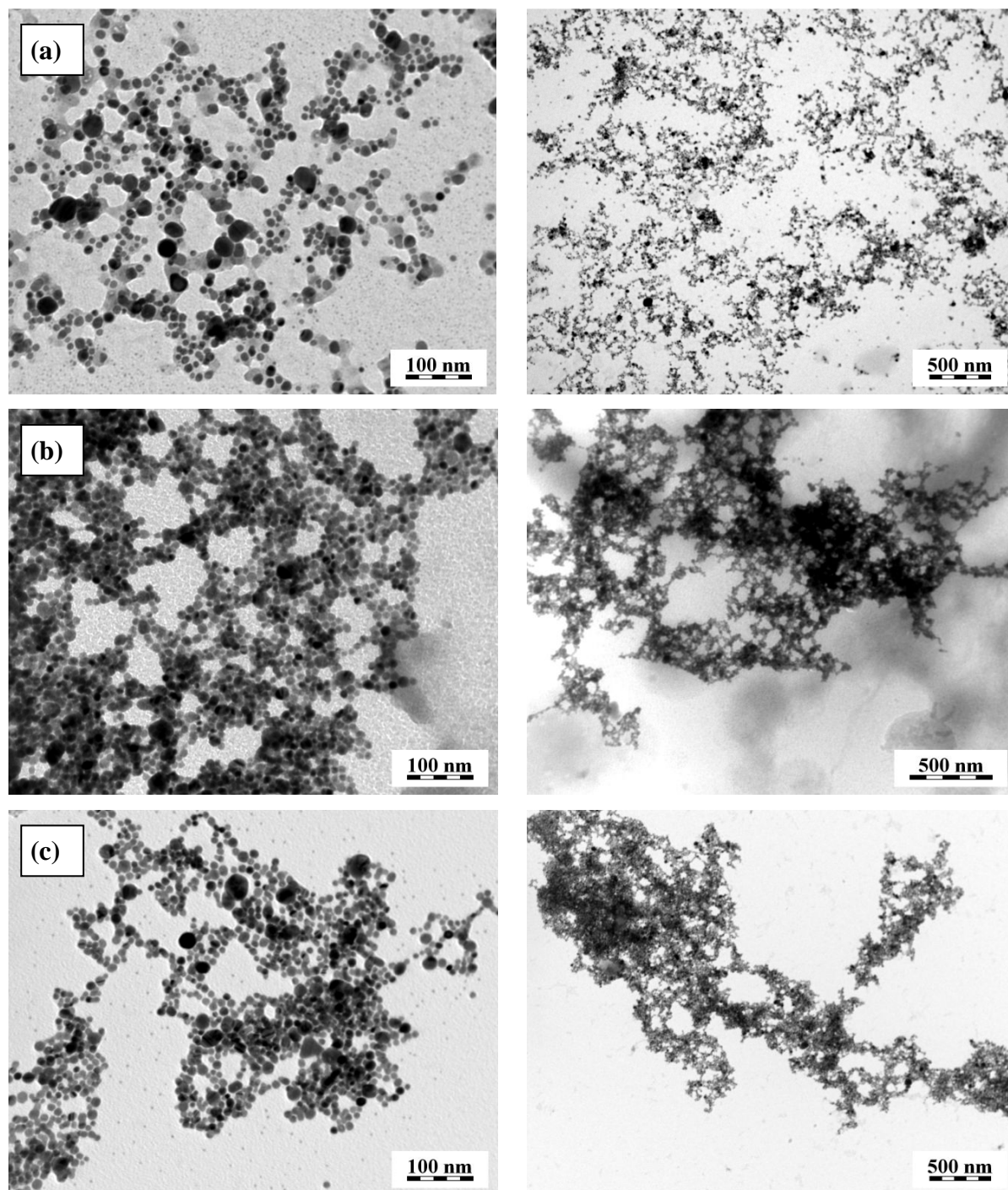


Figure 4.2-4. TEM images of the composites cast and dried from the Ag/PEEP-I hydrosol systems with (a) 1×10^{-4} M (b) 5×10^{-6} M and (c) 5×10^{-7} M PEEP-I concentration taken immediately after the preparation. Two different magnifications are shown.

Representative TEM image used for fractal analysis and corresponding dependences from which the fractal dimensions were determined are shown in Figure 4.2-5. An average value of the fractal dimension, $D = 1.9 \pm 0.1$, was obtained from the slopes of all dependences for three different TEM images. This value indicates that the fractal aggregates are present in the Ag/PEEP-I system obtained from the hydrosol system with the 5×10^{-6} M polymer concentration. The actual values of fractal dimensions determined from these analyses ranged from $D = 1.78$ (which is close to $D = 1.75$ inherent to fractal aggregates formed by diffusion-limited cluster-cluster aggregation), to $D = 2.05$ (which is close to $D = 2$, the value typical for an infinite array of regularly /hexagonally/ packed NPs of uniform sizes). The observed dispersion of fractal dimension values can possibly stem from a partial re-assembling of fractal Ag NPs aggregates after the deposition on the supporting surface, i.e. on the carbon-coated TEM grid, into planar sub-structures of more or less regularly packed Ag NPs. The regularity of the planar arrangement is influenced by a polydispersity of the Ag NPs assembly.

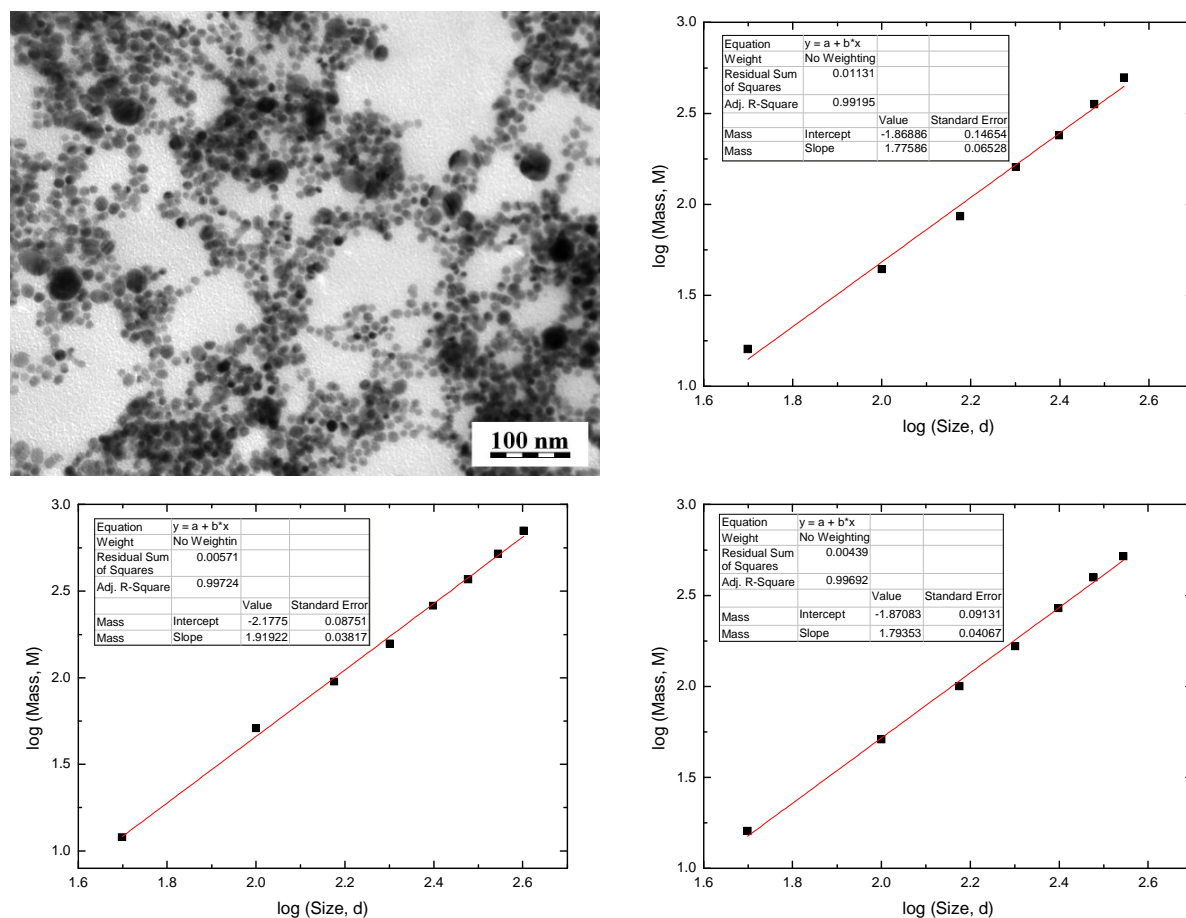


Figure 4.2-5. TEM image of Ag/PEEP-I system with 5×10^{-6} M PEEP-I concentration used for determination of fractal dimension and dependences of masses M versus sizes R of the objects. The slope of such dependence corresponds to the fractal dimension (D).

4.2.3. Summary of results of the SPE probing and TEM imaging of the Ag/PEEP-I hydrosol systems

In summation, the rate of aggregation, the morphology of the aggregates as well as the stability of the nanocomposite systems depend on the polymer concentration. We assume that the polymer is adsorbed on Ag NPs by an electrostatic interaction between the positively charged pyridinium polymer side groups and negatively charged ions (borates and iodides) covering the Ag NP surface. At low polymer concentrations, the positively charged polymer partially compensates the negative surface charge of the nanoparticles, and the aggregation is observed with a rate proportional to the polymer concentration. In particular, in the system with 5×10^{-6} M polymer concentration, the compensation of charges causes a rapid aggregation of Ag NPs into fractal aggregates ($D = 1.90$). This process manifests itself in the SPE spectra by the growth of a secondary SPE extinction band around 530 nm, in accord with the theoretically predicted optical responses of fractal aggregates²⁶. At a limiting polymer concentration (estimated to be around 1×10^{-5} M), the negative surface charge of the NPs is expected to be fully compensated by the attachment of the cationic pyridinium side-groups of the polymer. Therefore, at higher polymer concentrations, there are non-adsorbed parts of the polymer chains, the presence of which hinders Ag NP aggregation. As a result, less dense Ag NP – polymer aggregates are formed with interparticle spacings larger and the overall dimensions smaller than those encountered for fractal aggregates formed at lower polymer concentrations (Figure 4.2-4). This explanation is confirmed both by the increased hydrosol stability for the system with the polymer concentration higher than 1×10^{-5} M, and by the SPE spectra exhibiting a broad extinction band red-shifted from that of the parent Ag NP hydrosol, as expected on the basis of theoretical calculations performed for DNA linked Au NP aggregates¹⁶⁰.

Furthermore, two types of calculations related to the explanation provided above were performed. In the first case, a simple calculation showed that there are 500 and 10 000 monomeric units per one Ag NP for the systems with polymer concentration 5×10^{-6} M and 1×10^{-4} M, respectively, considering the average diameter of Ag nanoparticles of 9 nm determined by TEM image analysis. If we estimate the surface area of one monomer unit anchored to the NP surface to be about 0.15 nm^2 , 1800 monomer units would be required to cover the whole NP surface. This value is close to the limiting concentration 1×10^{-5} M, at which a change in the optical spectra evolution and, consequently, in the mechanism of the aggregate formation, has been encountered.

An alternative explanation of spectra evolution at the higher polymer concentrations was tested based on a possible change of resonance conditions caused by variations in the dielectric constant of the environment after addition of the polymer. In particular, it was considered whether or not this effect could be fully or partially responsible for the red shifts of SPE band in the spectra of the composite systems with the polymer concentration above 1×10^{-5} M. Nevertheless, it was found that the magnitude of the observed effect does not correspond to the calculated values¹⁶¹. Therefore, the primary reason for the observation of the broad SPE band red-shifted with respect to that of the parent sol is a weak interparticle interaction in the loosely packed Ag NP-polymer aggregates, as proposed above.

4.2.4. Raman spectra of Ag/PEEP-I nanocomposite systems

Raman spectra of Ag/PEEP-I system ($C_{\text{PEEP-I}} = 5 \times 10^{-6}$ M) containing fractal aggregates of Ag nanoparticles were measured using 441.6, 488.0 and 514.5 nm excitations (Figure 4.2-6). The 441.6 nm excitation matches the polymer absorption at 440 nm maximum (Figure 4.2-2) and fulfills thus the molecular resonance condition with the π -conjugated polymer chain. On the other hand, it falls within a minimum between the two SPE bands of the composite system (Figure 4.2-3d). By contrast, the 488.0 and 514.5 nm wavelengths fall only into the edge of the polymer absorption band (Figure 4.2-2), however, they approach the maximum of the second SPE band of the composite system attributed to fractal aggregates (Figure 4.2-3c).

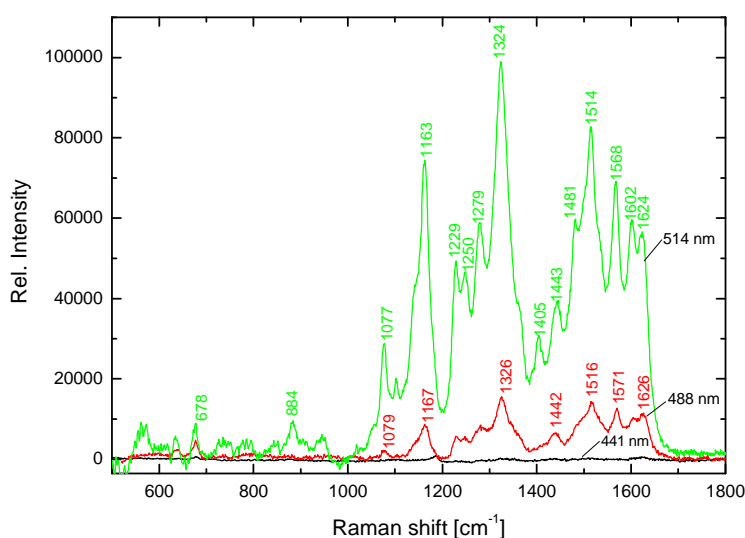


Figure 4.2-6. SERS spectra of Ag/PEEP-I hydrosol system with 5×10^{-6} M PEEP-I concentration measured with (a) 441.6 nm, (b) 488.0 nm and (c) 514.5 nm excitation wavelengths. Baseline correction was performed with Origin 8 software.

The spectrum obtained at 441.6 nm excitation wavelength is dominated by a strong fluorescence, and no characteristic Raman bands could be observed after the subtraction of the fluorescence background. In contrast to that, intense and well resolved Raman spectra were obtained with the 488.0 and 514.5 nm laser excitations. The positions of Raman bands closely match those observed recently for structurally analogous polymers^{127, 162}. The bands at 1076, 1160, 1568 and 1622 cm^{-1} are assigned to the vibrations of pyridinium ring: pyridine CCH bending (1076, 1160 cm^{-1}) and pyridinium ring stretching (1568, 1622 cm^{-1}). The band at 1514 cm^{-1} corresponds to the polymer backbone C=C stretching vibration. Additionally, it should be mentioned that with the same excitation wavelengths Raman spectrum of pure PEEP-I could not be obtained owing to its strong fluorescence background.

The results of Raman spectral probing provide an unequivocal proof that the Raman spectra obtained from the Ag/PEEP-I composite system at 514.5 and 488 nm are the surface-enhanced Raman spectra of the polymer and demonstrate that the operation of electromagnetic mechanism of SERS is of key importance for obtaining a Raman spectrum of the polymer from the composite system.

Furthermore, SERS spectra of the Ag/PEEP-I system ($C_{\text{PEEP-I}} = 5 \times 10^{-6}$ M) measured with the 514.5 nm excitation both from the hydrosol system and from the sedimented aggregates deposited on a glass slide are compared in Figure 4.2-7. It was found that SERS spectra of deposited Ag/PEEP-I aggregates are nearly identical with those obtained from the hydrosol system. We can thus conclude that the polymer remains to be an inherent part of the Ag/PEEP-I system even after the deposition, and that about the same fraction of the polymer chains remains localized in the hot spots of fractal aggregates before and after the deposition. Nevertheless, a minor spectral difference, in particular the change of the relative intensity ratios of 1604 cm^{-1} and 1622 cm^{-1} bands attributed to the pyridine and pyridinium ring stretching, respectively, has been observed. This can be explained by the change of the fraction of the protonated and the non-protonated pyridines of polymer, or by the change of the enhancement experienced by these vibrational modes after the deposition.

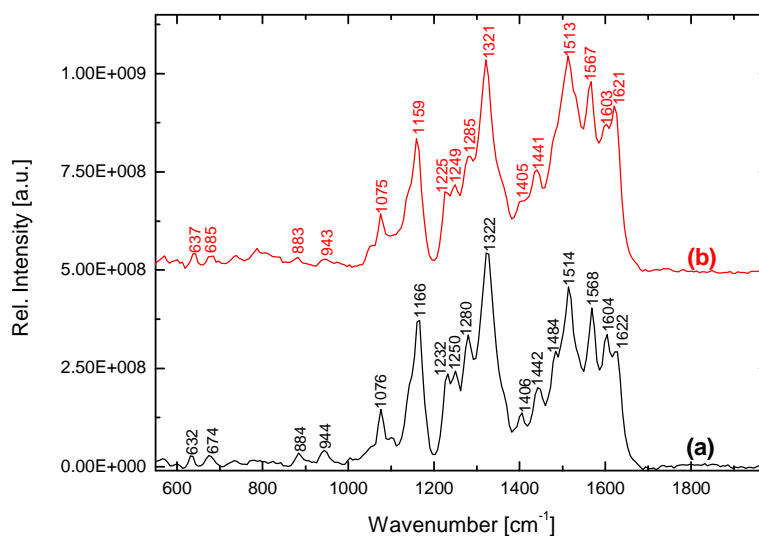


Figure 4.2-7. SERS spectra of Ag/PEEP-I system with 5×10^{-6} M PEEP-I concentration measured from (a) hydrosol system immediately after the preparation and (b) Ag/PEEP-I aggregates cast on glass substrate. Excitation wavelength was 514.5 nm in both cases. Baseline correction was performed with Origin 8 software.

Finally, SERS spectra of Ag/PEEP-I nanocomposite systems were measured using 514.5 nm excitation wavelength as a function of the polymer concentration. The resulting spectra, measured immediately after the system preparation, are compared in Figure 4.2-8. The onset of the polymer SERS signal observation is at 5×10^{-8} M concentration. For 5×10^{-7} M concentration, a substantial increase of SERS intensity is observed, however, only a weak increase of the SERS signal is detected in the 5×10^{-7} M- 1×10^{-5} M concentration range. For concentrations higher than 1×10^{-5} M, the SERS signal has actually decreased. This somewhat peculiar concentration dependence of the SERS signal can be plausibly explained, provided that we consider the morphology and optical spectra of the composite systems and their dependence on the polymer concentration (see Figure 4.2-3 and Figure 4.2-4). Apparently, the largest SERS signals are obtained for systems with an occurrence of fractal aggregates, in which localization of the polymer chain segments in hot spots can be expected. In such systems the 514.5 nm optical excitation closely matches the fractal aggregate extinction band (Figure 4.2-3c,d,e) resulting in the strongest enhancement of Raman scattering by electromagnetic mechanism^{163, 164}. Since the number of Ag NPs in the systems remains constant and fractal aggregates are formed, the number of hot spots finally created in the system after the aggregation is accomplished does not change dramatically with the polymer concentration in the 5×10^{-7} M - 1×10^{-5} M concentration range. However, since the spectra were measured immediately after system preparation, the weak increase of SERS

signal with increasing polymer concentration probably reflects the increasing rate of aggregation and, consequently, of hot spots formation. The decrease of the SERS signal for systems with the polymer concentrations higher than 1×10^{-5} M can be explained by weakening of the localized electromagnetic fields between the Ag NPs caused by the increasing interparticle distance in the loosely packed Ag nanoparticle-polymer aggregates formed at these high polymer concentrations as well as by a rather poor matching between the 514.5 nm excitation and the extinction of these aggregates having the maximum at 430 nm (Figure 4.2-3a, b).

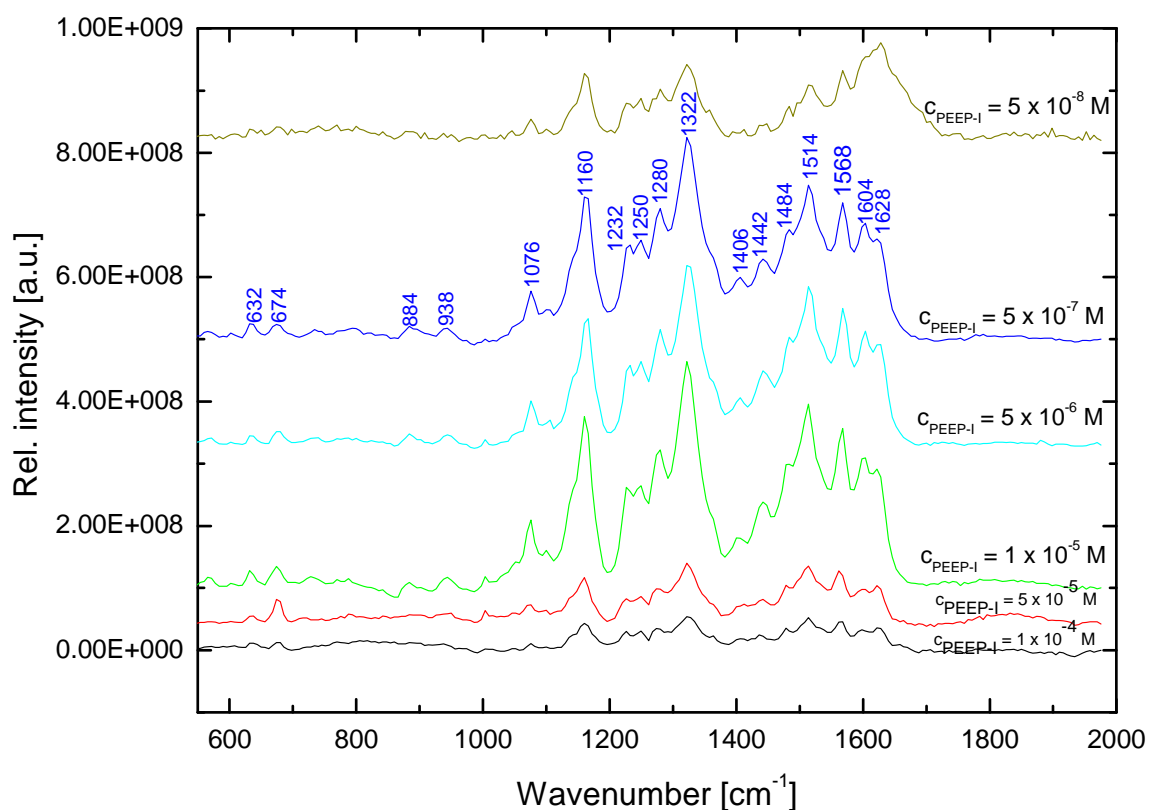


Figure 4.2-8. SERS spectra of Ag/PEEP-I hydrosol systems containing different PEEP-I concentration measured with 514.5 nm excitation wavelength. Baseline correction was performed with Origin 8 software.

4.2.5. Fluorescence spectra of Ag/PEEP-I nanocomposite systems

Most of the π -conjugated polymers show fluorescence emission in the visible spectral region. Although iodine ions are known as fluorescence quenchers, PEEP-I exhibits a strong fluorescence with emission maximum around 500 nm. It is generally accepted that the main advantage of the incorporation of Ag or Au nanostructures in SERS measurements is the limitation of fluorescence background that decreases the sensitivity of Raman spectroscopy. Surprisingly, in SERS spectra of PEEP-I fluorescence background was still observed, even

when a strong enhancement of Raman scattering proves the efficient interaction between the polymer and surface plasmons of Ag NPs. Hence, we performed independent fluorescence measurements of Ag/PEEP-I hydrosol systems. The fluorescence spectra of Ag/PEEP-I systems were compared with those obtained for the reference polymer solutions diluted by water to the same concentration as in Ag/PEEP-I systems. Fluorescence was excited with 352 nm wavelength falling into the maximum of excitation spectrum of the polymer (Figure 4.2-9) corresponding to the photoexcitation of the π -conjugated backbone. Several questions and problems which have arisen during the measurements will be discussed in the following paragraphs.

First, it should be emphasized that contradictory results concerning fluorescence of chromophores near metal nanostructures were reported in the literature. Some experimental studies demonstrate fluorescence enhancement^{130, 165} for molecules placed near a metal nanostructure, other studies report fluorescence quenching^{146, 166}. It has been found that the distance between the chromophore and the metal nanoparticle¹⁶⁷ as well as the fluorescence quantum yield of the isolated chromophore¹¹⁸ play the key role in determination of the fluorescence of the chromophore - metal nanoparticle system. Moreover, the influence of the morphology of nanoparticle assemblies on the fluorescence emission is only poorly discussed. To our best knowledge, there is no report in the literature on the influence of fractal aggregates formation on the fluorescence emission.

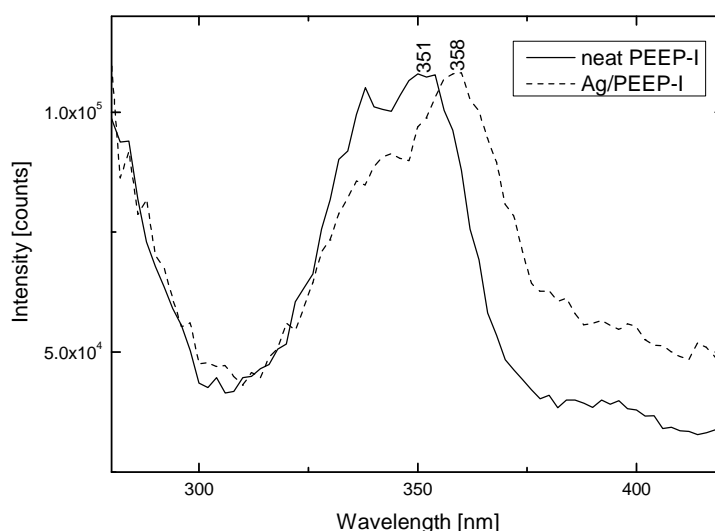


Figure 4.2-9. Excitation spectra of neat polymer (solid line) and of Ag/PEEP-I system (dashed line) containing 5×10^{-7} M polymer concentration prepared by five times dilution of 2.5×10^{-6} M Ag/PEEP-I system, measured at 500 nm emission wavelength.

The problem has arisen since Ag hydrosol used for the aggregation studies had a high extinction, thus internal filter effect appeared during the fluorescence measurements of Ag/PEEP-I systems. Therefore, to be able to compare the fluorescence intensity of Ag/PEEP-I systems with that of reference systems, we had to perform the correction to the internal filter effect. No changes were detected in emission spectra of Ag/PEEP-I systems containing polymer concentration higher than 1×10^{-5} M (1000 monomeric units per one Ag NP) for the overall monitored period of about 90 min after the mixing. On the other hand, more pronounced changes were detected for the Ag/PEEP-I systems which show the secondary SPE band (around 530 nm) assigned to the fractal aggregates formation in the same time as during fluorescence monitoring. Nevertheless, the results obtained for various experiments were scattered: no statistically relevant tendency of the changes of fluorescence emission could be determined.

We also considered a possibility that the changes in fluorescence emission can be actually very small and can be caused by decrease of polymer concentration due to the sedimentation of Ag aggregates formed after the mixing with the Ag hydrosol. Therefore, we determined the amount of silver left in the sol during aggregation process for Ag/PEEP-I system with the polymer concentration 5×10^{-6} M using an atomic absorption spectroscopy. We found that the content of silver in the hydrosol does not change within two hours after the mixing of Ag hydrosol with PEEP-I solution. Therefore, the observed changes in the fluorescence spectra reflect the dynamic behavior of the composite system and they are not related to aggregates sedimentation, since it occurs only at much longer time after the mixing, than it is the time scale of the fluorescence measurement.

In order to exclude the errors which could be caused by the correction on the internal filter effect we measured the emission spectra of Ag/PEEP-I systems that had been diluted to yield the optical extinction values below 0.35. These systems were prepared by dilution of Ag/PEEP-I systems originally containing 2.5×10^{-6} M polymer concentration with water to the final concentrations 5×10^{-7} M, 2.5×10^{-7} M and 1.7×10^{-7} M. The dilution was done 2 min after the mixing of the polymer solution with Ag hydrosol to allow for the nanoparticle aggregation as it was evidenced by UV-Vis spectra. The emission spectra of the Ag/PEEP-I systems together with the emission spectra of the polymer solutions containing the same corresponding polymer concentrations are shown in Figure 4.2-10. A decrease of about 10 - 20 % in the fluorescence intensity was observed for all Ag/PEEP-I systems compared to the intensities of the reference systems. Hypsochromic shift of the emission spectra and

bathochromic shift of the excitation spectra (see Figure 4.2-9) were observed that resulted in the decrease of Stokes shift of about 10 nm.

Two factors have to be taken into account to explain the observed changes. First, fluorescence intensity may decrease with ionic strength of the polymer environment. It is expected to occur upon mixing the polymer solution with Ag hydrosol containing ions originating from the reductant (NaBH_4). The decreased Stokes shift may be explained by increased rigidity of the polymer chains anchored to the nanoparticle surface. Adsorption of the polymer on Ag nanoparticle leads to a limitation of vibrations of the polymer chains, which are more solidly anchored to Ag nanoparticle compared with free polymer chains in reference system (in water).

The observed decrease in the fluorescence intensity could be also explained by NP induced fluorescence quenching. In the Ag/PEEP-I systems, there could be an equilibrium between the polymer electrostatically attached to the NP surface and the free polymer dissolved in water. Only the fluorescence of the minority of molecules, that are in contact with the NP surface, would be quenched, while the emission of free molecules remains unaffected. This could lead to only partial fluorescence quenching of the Ag/PEEP-I system. However, the whole spectrum is blue shifted, showing that the majority of emitting molecules is affected by the interaction with Ag NPs.

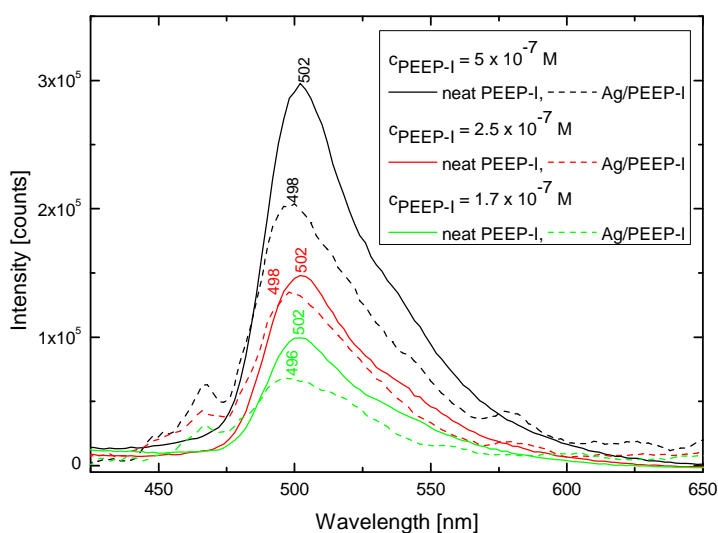


Figure 4.2-10. Emission spectra of the neat polymer (solid lines) and of the Ag/PEEP-I systems (dashed lines) with various polymer concentrations obtained by five (black line), ten (red line) and fifteen (green line) times dilution of 2.5×10^{-6} M Ag/PEEP-I system. The excitation wavelength was 352 nm.

4.2.6. Conclusions

1. The morphology, optical responses and stability (in an aqueous ambient) of Ag NP/PEEP-I composite systems are influenced by the polymer concentration. Attachment of the polymer to Ag NP surface by an electrostatic interaction between the positively charged side-groups of the polymer chains and negatively charged ions on the Ag NP surface is witnessed by the dependence of the rate of Ag NP aggregates formation on the polymer concentration in the low concentration range ($5 \times 10^{-7} \text{ M} - 1 \times 10^{-5} \text{ M}$). Fractal character of the deposited aggregates is documented by their average fractal dimension $D = 1.9 \pm 0.1$.
2. Using optical excitations with laser line wavelengths matching the extinction band of the fractal aggregates, intense and well resolved SERS spectra of the polymer are obtained. The strong signal most probably originates from the hot spots formed in the fractal aggregates occupied by the polymer chains.
3. In systems with polymer concentrations higher than 10^{-5} M , relatively small aggregates with a large interparticle distance are formed. Small size of the aggregates is responsible for their stability in the hydrosol. Longer interparticle distance in the aggregates with the increasing polymer concentration most probably originates in the steric effects caused by non-adsorbed parts of the polymer chains and results in a substantial decrease of SERS signal of the polymer.
4. A small decrease in fluorescence intensity of about 10 – 20 % accompanied by a blue shift of the emission spectra was observed for diluted Ag/PEEP-I systems showing SPE band typical of fractal aggregates. It was explained by (i) increased ionic strength upon addition of the polymer into Ag hydrosol, (ii) increased rigidity of polymer chains anchored to Au NPs and/or (iii) NP induced fluorescence quenching.

4.3. Polymer composites consisting of regioregular poly(3-octylthiophene-2,5-diyl) and plasmonic metal nanoparticles

In general, a two-phase synthesis approach has been adapted for the preparation of polymer composites consisting of regioregular poly(3-octylthiophene-2,5-diyl), P3OT, and Au or Ag NPs. This chapter compares optical and morphological properties of nanocomposites prepared by mixing a metal NP organosol with the polymer solution (composites type **M**) and nanocomposites prepared by in-situ reduction of a metal salt in the polymer solution (composites type **R**). Au/P3OT weight ratio was 1/1 for both composites since this ratio provided a narrow size distribution of Au NPs in Au/P3OT composite prepared by similar procedure as composite type **R** according to ref.⁷¹.

In the first chapter (Chapter 4.3.1.), metal (Au and Ag) organosols, which were used as precursors of composites type **M**, will be characterized. Surface plasmon extinction (SPE) spectra and transmission electron microscopy (TEM) images will be discussed and nanoparticle sizes obtained by TEM analysis and dynamic light scattering (DLS) for both organosols will be compared. The effect of the phase-transfer reagent used in the organosol preparation on the stability of the resulted sols and on the nanoparticle morphology will be also described.

Chapters 4.3.2. and 4.3.3. are focused on a characterization of nanocomposites containing Au and Ag nanoparticles, respectively. A number of techniques were used for nanocomposites characterization including UV-Vis absorption spectroscopy, transmission electron microscopy (TEM) and dynamic light scattering (DLS). A special attention was paid to the effect of the type of phase transfer agent used in composite preparation as well as to the effect of precipitation of composite solution in methanol and its redissolution in toluene, as important steps in composite preparation, on nanoparticle morphology in the resulted composites.

In the last chapter 4.3.4., Raman spectra of thin films of Au/P3OT and Ag/P3OT composites are investigated. The spectra are interpreted in terms of the actual nanoparticle morphology within the thin nanocomposite films. The spectral analysis is focused on several characteristic bands, which are compared with the previously published results obtained for similar systems. For Raman spectra measurements of Ag/P3OT composites, several excitation lines were used to evaluate the magnitude of the surface enhancement of Raman scattering at various wavelengths with regards to their UV-Vis spectra.

4.3.1. Metal organosols – precursors for composite type M

4.3.1.1. Au organosols

SPE spectra of Au organosols in toluene prepared with two different phase-transfer agents, tetraoctylammonium bromide (TOAB) and tetradodecylammonium bromide (TDAB), respectively, are shown in Figure 4.3-1. Although the positions of SPE maxima of both organosols are at the same wavelength ($\lambda_{max} = 526$ nm), the half-widths of the SPE band as well as the magnitudes of the extinction at the SPE maximum mutually differ. The SPE band of TDAB-stabilized Au organosol exhibits narrower band with a higher value of extinction at the SPE maximum compared to the TOAB-stabilized Au organosol (see inset of Figure 4.3-1). TDAB-stabilized Au organosols shows a better long-term stability (more than 1 year) without formation of any macroscopic Au aggregates. On the other hand, macroscopic Au aggregates were found already during the preparation of TOAB-stabilized Au organosols. The aggregates have a tendency to sedimentation, hence the magnitude of their SPE extinction maximum is lower than that for TDAB-stabilized Au organosol. This result indicates that TDAB molecules stabilize Au NPs more effectively than TOAB.

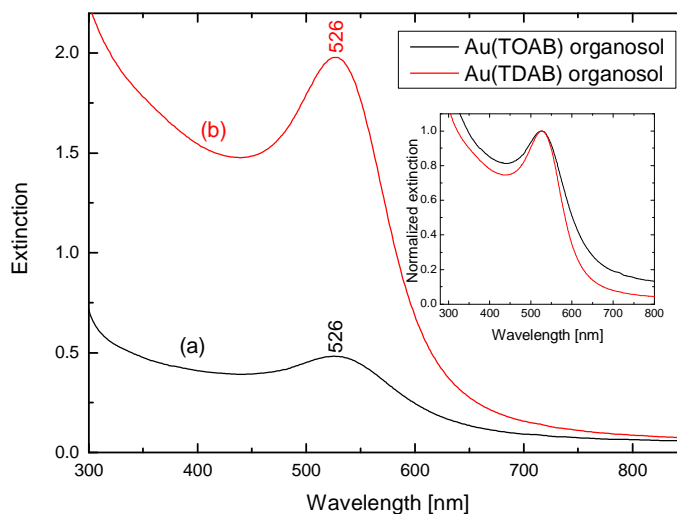


Figure 4.3-1. SPE spectra of Au organosols stabilized by (a) TOAB and (b) TDAB. Spectra normalized at their maxima are shown in Inset for comparison of the band half-width.

TEM images of Au organosols prepared using TOAB and TDAB are shown in Figure 4.3-2. TOAB-stabilized NPs form a network of closely packed nanoparticles. Although the presence of TOAB partially prevents nanoparticle aggregation into 3-D aggregates during deposition, it is evident from Figure 4.3-2a that the separation distance between nanoparticles is not uniform upon drying on microscopic grid and an overlap of some particles is clearly observable. On the other hand, TDAB-stabilized Au NPs remain well separated even upon

drying on microscopic grid. A tendency of Au NPs towards two-dimensional assembling, in which the individual particles have adopted the pseudohexagonal closely-packed arrangement, is clearly observable in TEM image of the organosol (Figure 4.3-2b). Different degree of self-assembling of TOAB- compared to TDAB-stabilized Au sols can be explained by the different chain length of the phase transfer agents resulting in various hydrophobic interactions. TDAB contains longer hydrophobic chains having higher affinity to carbon foil of microscopic grid than TOAB.

Nanoparticle sizes determined by TEM and DLS measurement are presented in Table 4.3-1. For both sols, the nanoparticle diameters determined by DLS measurement exceed those determined by TEM image analysis. This increase in diameter can not be explained by the presence of a layer formed by the phase-transfer reagent around the particle, because, in that case one would expect a maximal difference of only about 1-2 nm. Therefore, it is more probable that the solutions of Au organosols contain small associates of stabilized nanoparticles rather than individual NPs. These associates of Au NPs are formed by mutually interacting NPs which move jointly in the solution.

Finally, it should be noted that there is possibility that the organosol contains some traces of water because it was not dried (to avoid losses of nanoparticles which accompany the drying steps in organosol purification and desiccant separation). Therefore, the organosol could contain the emulsion of water in toluene.

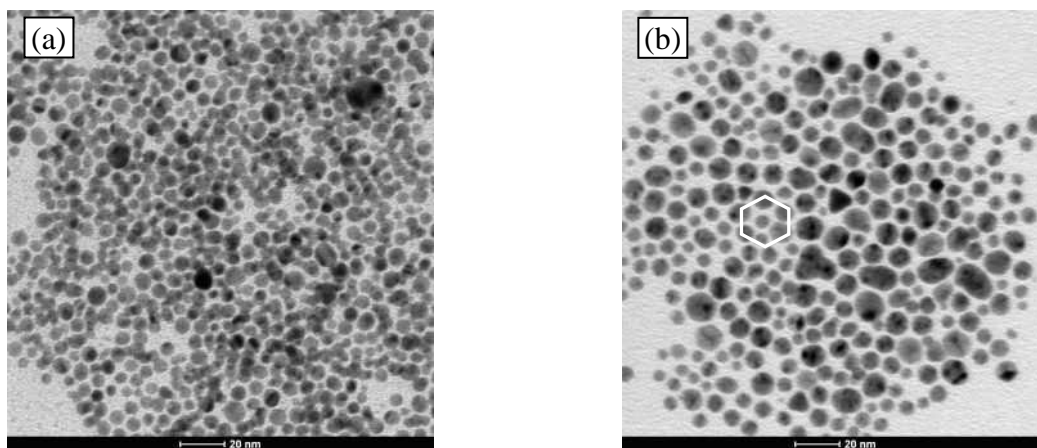


Figure 4.3-2. TEM images of Au organosols stabilized by (a) TOAB and (b) TDAB.

	d_{TEM} [nm]	d_{DLS} [nm]
Au(TOAB) organosol	5.6 ± 1.4	11.0 ± 1.6
Au(TDAB) organosol	6.4 ± 2.4	11.3 ± 0.3

Table 4.3-1. Nanoparticle diameters in Au organosols determined by TEM and DLS.

4.3.1.2. Ag organosols

Ag organosols in toluene were prepared by procedures similar to those employed for Au organosols preparation (see Experimental). However, for Ag organosols, the selection of the phase-transfer reagent plays a much more important role for the organosol stability than for Au organosols. In case of

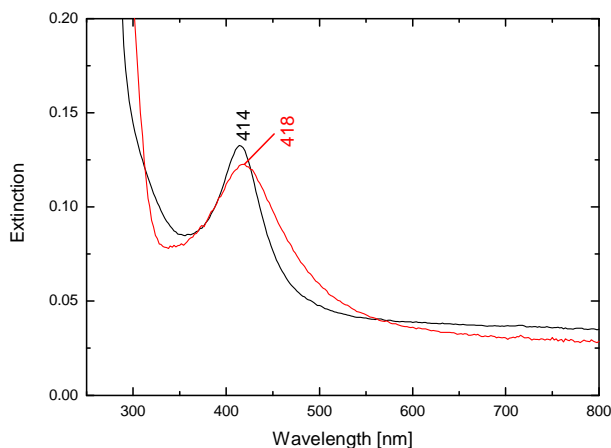


Figure 4.3-3. SPE spectra of TOAB-stabilized Ag organosol after the preparation (black line) and 8 days after the preparation (red line).

TOAB-stabilized Ag organosol, nanoparticle aggregation and pronounced sedimentation of macroscopic aggregates are observed even during the preparation. As a result, the concentration of Ag NPs in the sol is very low with a corresponding low optical extinction (typically below 0.15 in 1 cm cuvette) as documented in Figure 4.3-3. SPE spectrum of freshly prepared TOAB-stabilized Ag NP organosols is relatively narrow with a sharp band with a maximum at 414 nm. The spectrum develops in time as witnesses in Figure 4.3-3: eight days after the preparation, SPE band is non-symmetric with the maximum shifted to 418 nm. These spectral changes can be assigned to nanoparticle aggregation.

When TDAB is used in Ag organosol preparation instead of TOAB, Ag NPs remain stable for more than two months. Nevertheless, the aggregate formation and their sedimentation were also observed during the preparation, in particular during stirring after the addition of the reductant. To avoid losses of NPs from the organosol, the time of stirring after the reductant addition was limited. After 5 min of stirring, the aqueous phase was removed in separatory funnel. It was expected that the residual reductant was completely removed from the organic phase together with the aqueous phase. The organosol was left to stay at laboratory temperature and the time evolution of the SPE spectra was measured. Figure 4.3-4 shows the time-evolution of the SPE band of Ag organosol after the disruption of stirring. The extinction gradually increases with time while the position of SPE band remains unchanged. The extinction reaches the value of 2.1 after 5.5 h. After 5 days after the preparation, a further small increase in extinction was observed and the SPE maximum was shifted to 419 nm. The increase of the extinction during the time evolution shows that some traces of the reducing

agent remain in the organosol even after the removal of aqueous phase. Slow rate of reduction can be assigned to the different mechanism of reduction in the non-aqueous ambient compared to the reduction in the aqueous ambient where the reduction is completed within an hour.

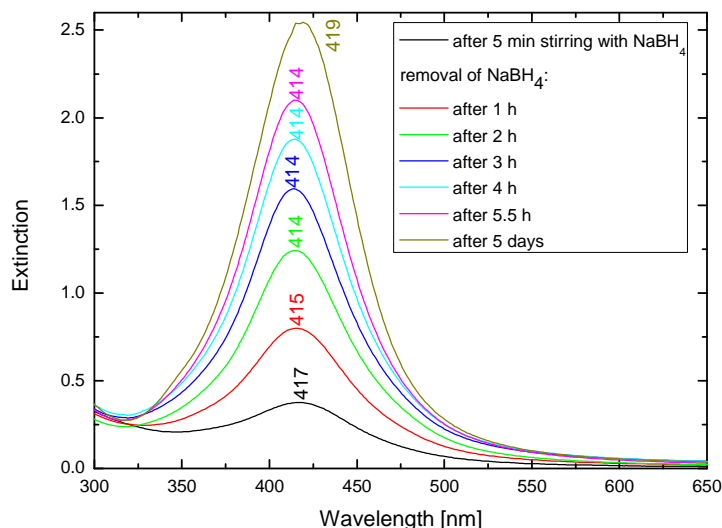


Figure 4.3-4. Time evolution of SPE spectra after the removal of aqueous phase and stirring disruption during TDAB-stabilized Ag organosol preparation.

TEM images of Ag organosols prepared using TOAB and TDAB are shown in Figure 4.3-5a and b, respectively. Ag NPs of the TOAB-stabilized Ag organosol (Figure 4.3-5a) are randomly scattered on microscopic grid whereas NPs of the TDAB-stabilized Ag organosol (Figure 4.3-5b) arrange into 2-D assemblies analogous to the NPs assemblies formed by Au organosols (Figure 4.3-2). The difference in nanoparticle arrangement could be assigned to the differences in concentration of nanoparticles in Ag organosols and/or in the dispersity of the nanoparticle sizes. Monodisperse Ag NPs in the TDAB-stabilized Ag organosol have higher tendency to form 2-D assemblies than polydisperse NPs in the TOAB-stabilized Ag organosol.

Nanoparticle diameters determined from the TEM images (Table 4.3-2) of the deposited Ag organosols stabilized by both phase-transfer reagents are very similar, but the TOAB-stabilized Ag organosol exhibits a significantly broader size distribution compared with the TDAB-stabilized Ag organosol. Nanoparticle diameters were also determined by DLS measurement (Table 4.3-2). The diameter of TDAB-stabilized Ag NPs is larger than that determined by TEM imaging, analogously to the case of the TDAB-stabilized Au NPs. The diameter of TOAB-stabilized Ag NPs could not be determined by DLS because of the high

polydispersity of the sample. The DLS results did not meet quality criteria for distribution analysis and the mean values could not be determined.

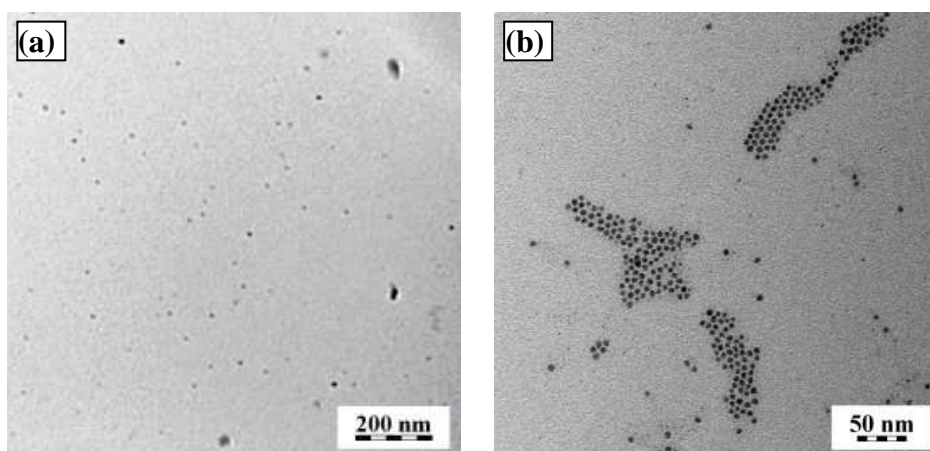


Figure 4.3-5. TEM images of Ag organosols stabilized by (a) TOAB and (b) TDAB.

	d_{TEM} [nm]	d_{DLS} [nm]
Ag(TOAB) organosol	7.6 ± 4.5	----
Ag(TDAB) organosol	6.2 ± 1.1	17.0 ± 1.4

Table 4.3-2. Nanoparticle diameters in Ag organosols determined by TEM and DLS.

In summation, TDAB used in the Ag organosol preparation leads to the fabrication of monodisperse Ag nanoparticles. Generally, the production of monodisperse nanoparticles requires a temporally discrete nucleation event which, in our case, can be achieved by the rapid addition of the reducing agent (sodium borohydride) to the reaction vessel followed by a slower controlled growth of the existing nuclei¹⁶⁸. For Ag NPs larger than 25 nm in diameter, a further nanoparticle growth should be accompanied by the shift of SPE maxima. However, SPE maxima remain in the same position during the experiment. It indicates that small Ag NPs with sizes up to 25 nm are produced. Moreover, the formed nanoparticles are highly monodisperse as demonstrated by the TEM image (Figure 4.3-5b). Therefore, we speculate that the nanoparticle formation could possibly occur in reverse micelles which consist of a hydrophilic core containing some Ag^+ species together with ions of the reducing agent and a shell formed by hydrophobic alkyl chains of the phase-transfer reagent. The formation of nanoparticles inside the micelles could explain the monodispersity of TDAB-stabilized Ag NPs. It should be noted that the mechanism of the phase transfer of silver-containing species into the organic phase is not clear since silver is originally present in the aqueous phase as a cation.

4.3.2. Characterization of Au/P3OT composites

4.3.2.1. UV-Vis spectroscopy

UV-Vis spectra of toluene solutions of Au/P3OT composites type **M** are shown in Figure 4.3-6a. The main absorption band of P3OT observed at 450 nm is consistent with the known position of $\pi \rightarrow \pi^*$ transition of the conjugated polymer chain. The spectra of the composites resemble to the spectrum of neat polymer, the positions of absorption maximum are the same as that for neat polymer and only distinct asymmetric broadening of the polymer absorption band is observed when compared to the spectrum of pure P3OT. In particular, the spectra of Au/P3OT composites type **M** show a substantially higher absorption in the regions 300 to 400 nm and 500 to 800 nm. The increase in extinction within these wavelength regions is more pronounced for the composites obtained from TDAB-stabilized Au organosol. It corresponds to a higher content of Au NPs in TDAB-stabilized Au organosol. Zhai et al.⁷¹ explained the extended absorption in the range 500 to 600 nm by a combined effect of two factors: a long-range ordering of the polythiophene caused by self-assembling of the polymer segments on metal NP surface, and by the SPE of Au NPs. Absorption spectra of highly ordered chains of regioregular poly(3-hexylthiophene) show typical distinct vibronic features¹⁶⁹. In our case, an increased intermolecular interaction during the self-assembling of the polymer was not confirmed as neither a spectral structuring nor a shift of absorption maximum of the polymer was observed. Therefore, the increase of extinction in the red spectral region corresponds to the SPE of Au NPs and/or Au NP aggregates (see Figure 4.3-6a).

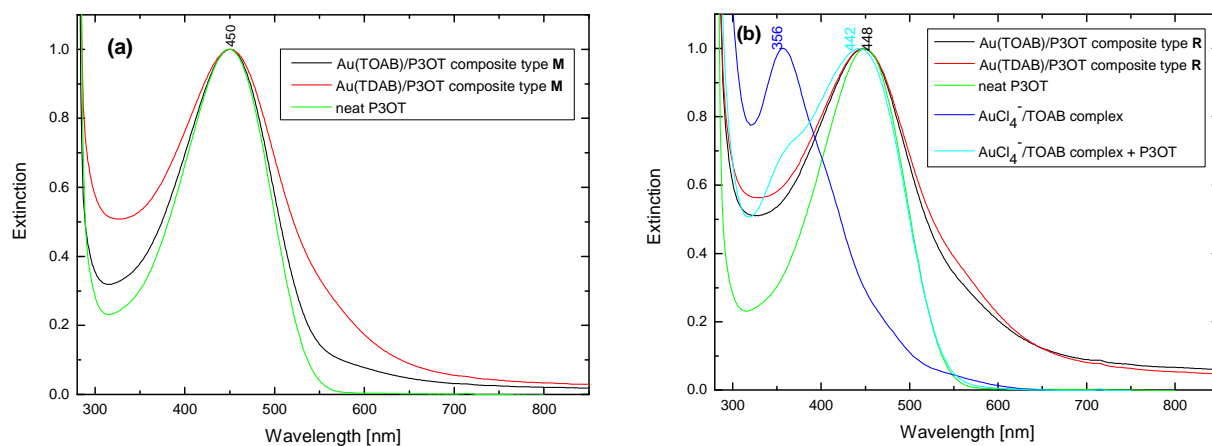
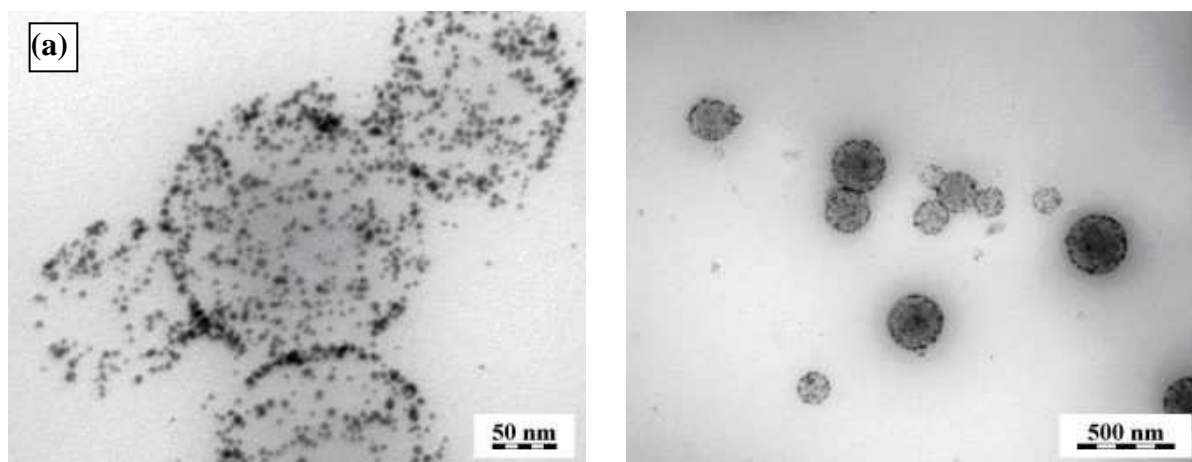


Figure 4.3-6. UV-Vis spectra of Au/P3OT composites: (a) type **M** and (b) type **R** prepared by using two different phase transfer agents. The spectra are normalized to their extinction maxima.

UV-Vis absorption spectra of Au/P3OT composites type **R** and its constituents are depicted in Figure 4.3-6b. $\text{AuCl}_4^-/\text{TOAB}$ complex has a strong absorption band at 356 nm as shown in Figure 4.3-6b (blue curve). This absorption band is characteristic of the metal-to-ligand charge-transfer band of AuCl_4^- complex ions¹⁸. The cyan curve corresponds to the spectrum obtained by mixing $\text{AuCl}_4^-/\text{TOAB}$ complex and polymer solution before the reduction step. It is a simple superposition of the absorption bands of P3OT and of the complex. Rapid injection of the reducing agent to the mixture of the complex and polymer initiates the reduction of Au ions yielding composites type **R**. The spectra of both composites type **R** are similar, only slightly higher extinction was observed around 550 nm for Au(TDAB)/P3OT composite showing higher Au NP content in this composite than that in Au(TOAB)/P3OT composite. The higher extinction between 600 and 850 nm of the solutions of composites **R** compared to composites type **M** could be explained by a presence of larger Au NPs or NP aggregates.

4.3.2.2. Transmission electron microscopy (TEM)

Figure 4.3-7 shows the TEM micrographs of Au/P3OT composites type **M** and **R**, both obtained using TOAB, before the precipitation in methanol. A common feature observed in all obtained micrographs before precipitation is a presence of globular structures with the concentration of NPs on their perimeter. Similar globular structures were observed earlier in Au/P3OT blended film by Sarathy et al.¹⁷⁰. The high density of NPs in the periphery was explained by the non-uniform evaporation rate of the solvent within the droplet of composite cast on a substrate and by a finite mobility of the NPs. The aggregation of polymer chains was also taken into account. The aggregation can act as an effective force accelerating NPs motion during the drying process, giving rise to the inhomogeneous radial distribution of the NPs¹⁷⁰.



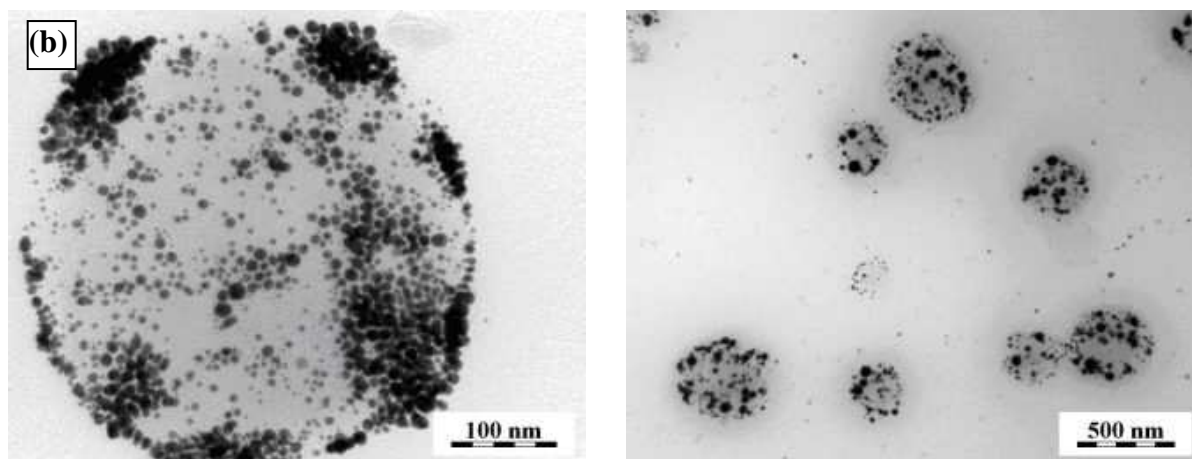


Figure 4.3-7. TEM images of Au(TOAB)/P3OT composites type (a) **M** and (b) **R** before the precipitation in methanol.

It was found that the formation of the globular structures is influenced by the presence of a phase transfer reagent (tetraoctylammonium bromide) as well as P3OT in the solution of Au/P3OT composites as confirmed by Figure 4.3-8. While the globular structures are not present in TEM images of the Au organosol and the neat polymer, they are obvious in TEM image (Figure 4.3-8) of the polymer containing TOAB of the same concentration as that used in composite preparation. Thus, TOAB in combination with the polymer plays the role in a formation of such globular structures. The dark structures may be identified as drops of P3OT/TOAB mixture formed during the drying of P3OT/TOAB solution on microscopic grid. The contrast is possibly given by the presence of Br atoms inside the structures. Formation of globular structures can be assigned to increased surface tension due to the presence of ionic TOAB.

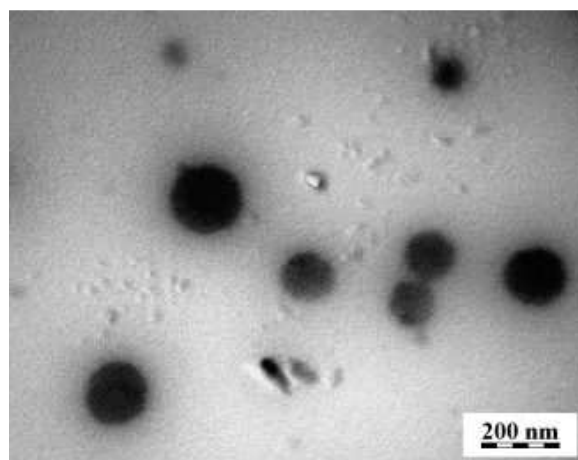


Figure 4.3-8. TEM images of a film cast from a solution of the P3OT with added TOAB.

Au NPs in the composites are stabilized preferentially by bromide ions originating from the phase-transfer reagent (TOAB). They show a high affinity towards Au surface. Bromide ions interact electrostatically with ammonium cation of TOAB, but the stabilization in organic solvent (toluene) is sterical through alkyl chains of TOAB. To ensure the replacement of TOAB for P3OT, the composites have to be precipitated in methanol. The precipitation plays an important role in composite preparation since the direct interaction

between Au NPs and the polymer is needed to induce effective surface plasmon modified photophysical phenomena in the polymer.

Figure 4.3-9 and Figure 4.3-10 show TEM images of Au NPs in the composite samples after the precipitation in methanol and redissolution in toluene. At the first glance, it is obvious that the globular structures disappeared. Au NPs in these composites are dispersed more homogeneously over the surface of a microscopic grid. The tendency of Au NPs towards two-dimensional assembling¹⁷¹ is clearly observable, manifesting itself as a formation of regions with nearly regular interparticle spacing.

As a result, a question has just arisen if the interparticle space is filled by the polymer and/or if the residual TOAB remained in the composites even after their precipitation and redissolution. To answer this question, an elemental analysis was performed. The results from the elemental analysis confirmed that the phase transfer reagent was mostly removed (the sample contained less than 0.25% nitrogen and no Br was detected within the resolution of the method).

Size distributions of Au NPs in Au/P3OT composites type **M** and **R** prepared using two different phase-transfer reagents are compared in Figure 4.3-11. Both procedures led to formation of small NPs (1 - 10 nm). Nanoparticle size distributions of Au/P3OT composites type **M** are narrower and mean particle sizes are slightly smaller than those for composites type **R**. In Au(TDAB)/P3OT composite type **M**, there is a great number of particles with sizes between 2 – 4 nm. This fraction results in a lower value of median of nanoparticle sizes ($d_{med} = 3.4$ nm) compared with that obtained for Au(TOAB)/P3OT composite **M** ($d_{med} = 4.2$ nm). In both composites type **R**, there are observable fractions of particles with sizes above 8 nm which are almost absent in the composites type **M**. The presence of these particles in the composites **R** shifts the values of median of nanoparticle sizes to higher values than those obtained for composites type **M**. The composite **R** prepared using TDAB contains particles with smaller sizes than composite **R** prepared using TOAB similarly to composites type **M**.

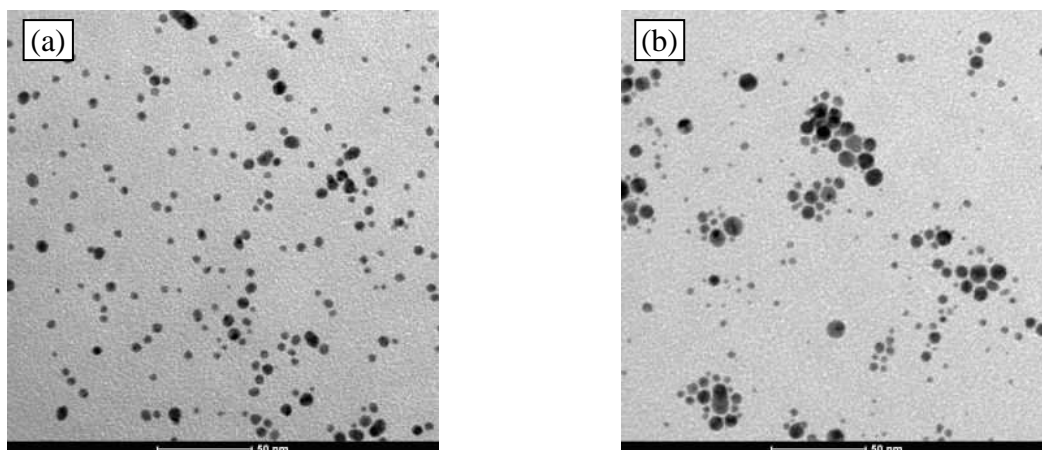


Figure 4.3-9. TEM images of Au/P3OT composites type **M** prepared from (a) TOAB-stabilized Au organosol and (b) TDAB-stabilized Au organosol.

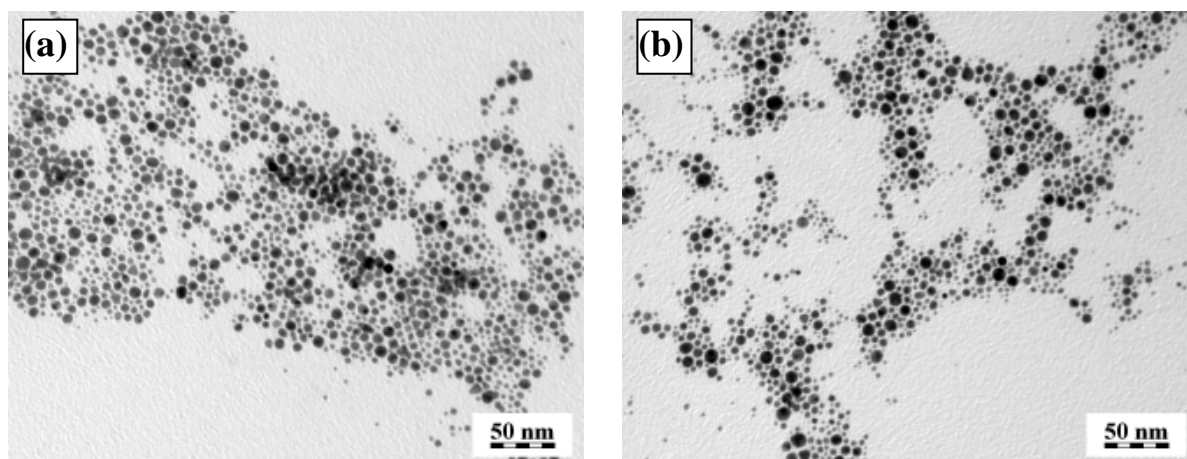


Figure 4.3-10. TEM images of Au/P3OT composites type **R** prepared using (a) TOAB and (b) TDAB.

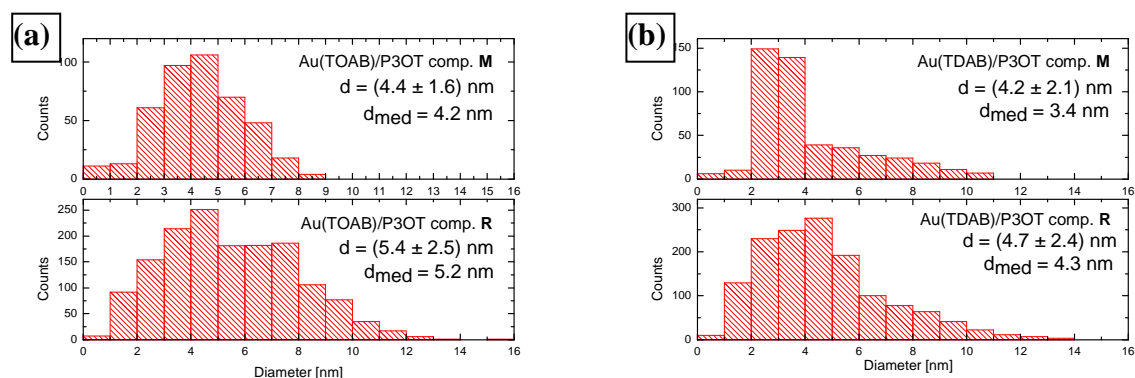


Figure 4.3-11. Nanoparticle size distributions in Au/P3OT composites type **M** and **R** obtained using (a) TOAB and (b) TDAB.

4.3.2.3. Dynamic light scattering (DLS)

The size of Au nanostructures in the composite solutions was also measured by DLS. DLS provides bulk information: it means that DLS measurement is sensitive to the size of the whole nanostructure present within the composite solution. Another advantage of DLS is that this method avoids selective sampling which can occur in TEM measurement. On the other hand, this technique has also inherent limitations (e.g., limited detectable size range) and should not be expected to give particle diameters which are identical to the TEM observations. DLS can serve as a very useful corroboratory technique in combination with TEM and UV-Vis measurements.

Nanoparticle size distributions determined by DLS for Au/P3OT composite samples are shown in Figure 4.3-12. Corresponding hydrodynamic diameters are presented in Table 4.3-3. Generally, monomodal particle size distributions were obtained for all composite samples except the composite type **M** prepared from the TDAB-stabilized Au organosol. The average nanoparticle sizes of all samples are markedly larger than those obtained by TEM measurements (Figure 4.3-11). It indicates that the solutions of composite samples contain larger objects which may be formed by the bridging of Au NPs by the polymer. These assemblies of Au NPs linked by the polymer chains thus show larger sizes in DLS experiment compared to the sizes of individual Au NPs obtained by TEM. Composite type **M** prepared from TOAB-stabilized Au organosol contains the assemblies with the smallest size ($d = (68.4 \pm 1.1)$ nm). Composite type **M** prepared from TDAB-stabilized Au organosol contains two particle fractions: the smaller one, having slightly larger size ($d = (17.1 \pm 2.1)$ nm) than the size of Au NPs in the original TDAB-stabilized Au organosol ($d = (11.3 \pm 0.3)$ nm), and the second one, having the size ($d = (117.6 \pm 1.7)$ nm) similar to the size of assemblies in the composites type **R** ($d = (105.7 \pm 1.7)$ nm). Au/P3OT composites type **R** prepared using both TOAB and TDAB have nearly the same particle sizes and particle size distribution.

	composite type M	composite type R
Au(TOAB)/P3OT	$d = (68.4 \pm 1.1)$ nm	$d = (106.4 \pm 1.4)$ nm
Au(TDAB)/P3OT	$d_1 = (117.6 \pm 1.7)$ nm $d_2 = (17.1 \pm 2.1)$ nm	$d = (105.7 \pm 1.7)$ nm

Table 4.3-3. Hydrodynamic diameters in Au/P3OT composites determined by DLS measurement.

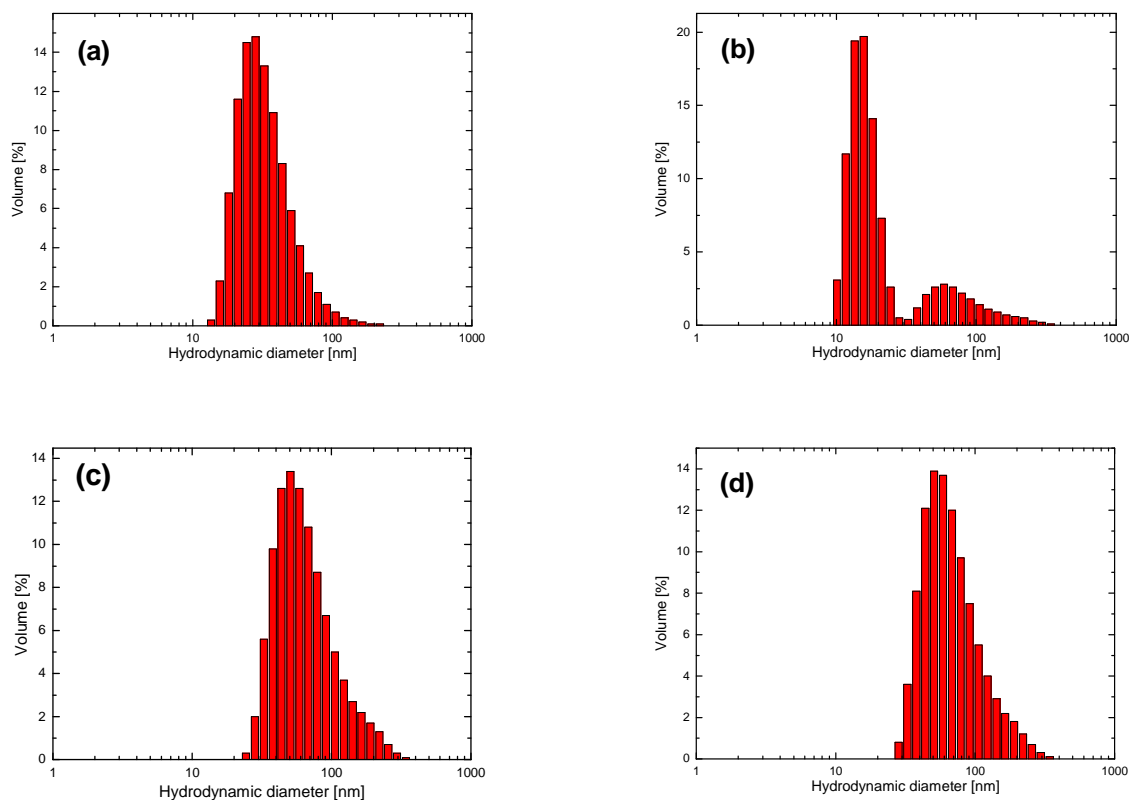


Figure 4.3-12. Nanoparticle size distributions determined by DLS for Au/P3OT composites type **M** (a,b) and type **R** (c,d) obtained using TOAB (a,c) and TDAB (b,d).

4.3.3. Characterization of Ag/P3OT composites

4.3.3.1. UV-Vis spectroscopy

UV-Vis spectra of Ag(TOAB)/P3OT composites type **M** and **R** are almost identical to the spectrum of the neat P3OT (Figure is not shown). This can be explained by weak extinction of TOAB-stabilized Ag organosol and by an overlap of the SPE band of Ag NPs with the absorption band of P3OT, both having the maxima in the same wavelength interval.

By contrast, the spectra of composites prepared using TDAB show observable differences from the spectrum of the neat polymer. Moreover, the precipitation of the composite in methanol has an influence on the spectra of composites. The spectra of Ag(TDAB)/P3OT composite type **M** before precipitation and its constituents (Ag organosol and neat P3OT) are depicted in Figure 4.3-13. The spectrum of the composite taken immediately after the mixing of both components exhibits the features of the Ag organosol. The band is slightly broadened compared to that of the parent organosol. The band broadening accompanied with a shift of SPE maxima occurs with increasing time of stirring of the composite. SPE maximum is shifted from 419 for the parent Ag organosol to 428 nm. It

could correspond to the interaction between the polymer chains and Ag NPs and/or nanoparticle aggregation. Precipitation of the composite and its redissolution in toluene has an essential impact on the composite spectrum. Firstly, the spectrum of composite loses the features of Ag organosol and resembles the spectrum of the polymer as can be seen from the inset of Figure 4.3-13. However, the difference between the spectra of the composite and neat polymer can be seen in long wavelength region. For the composite, the increase in extinction above 550 nm and a broad secondary band with a maximum around 800 nm are observed. It could be assigned to the presence of large Ag NPs or NP aggregates.

The spectra of Ag(TDAB)/P3OT composite type **R** during NPs formation as well as after precipitation are shown in Figure 4.3-14. Evolution of SPE spectra of the composite after the reductant addition shows that first the absorption maximum of the polymer shifts towards shorter wavelength and then the extinction increases with increasing time. We suspect that it corresponds to the formation of smaller Ag NPs having SPE band with maximum at about 420 nm, overlapping with polymer absorption. Precipitation of the composite and its redissolution in toluene has also influence on the composite spectrum, but the effect is different from that observed for composite type **M**. The position of the SPE maximum of the composite does not change, but the intensity of the main band decreases and, simultaneously, the extinction in the red region increases. The increase in extinction above 550 nm could correspond to the formation of Ag NP aggregates after the precipitation. We predict on basis of SPE spectra of the composites that the size of aggregates in composite type **R** is smaller than the aggregate size in the composite type **M** since elevated extinction background observed in the spectrum of composite **M** corresponds to large, nearly macroscopic aggregates. These aggregates approach the extinction characteristics of bulk silver. Contrary to that, gradual decrease in extinction above 550 nm observed for the composite **R** resembles a long-wavelength tail of SPE spectrum of Ag hydrosol upon addition of chloride ions which cause the formation of small compact Ag aggregates^{121, 172}.

Interestingly, such influence of precipitation on the spectra was not observed in the case of Au/P3OT composites. Thus, it can be suspected that the phase transfer reagent and/or the polymer have different affinity to nanoparticles of gold and silver, affecting the removal of the phase transfer agent during the precipitation. Moreover, the preparation method of composites seems to have also an influence on the morphology of nanoparticles in the resulted composites. To be able to discuss these speculations, the predicted nanoparticle morphology had to be confirmed by the TEM measurement followed by EDAX.

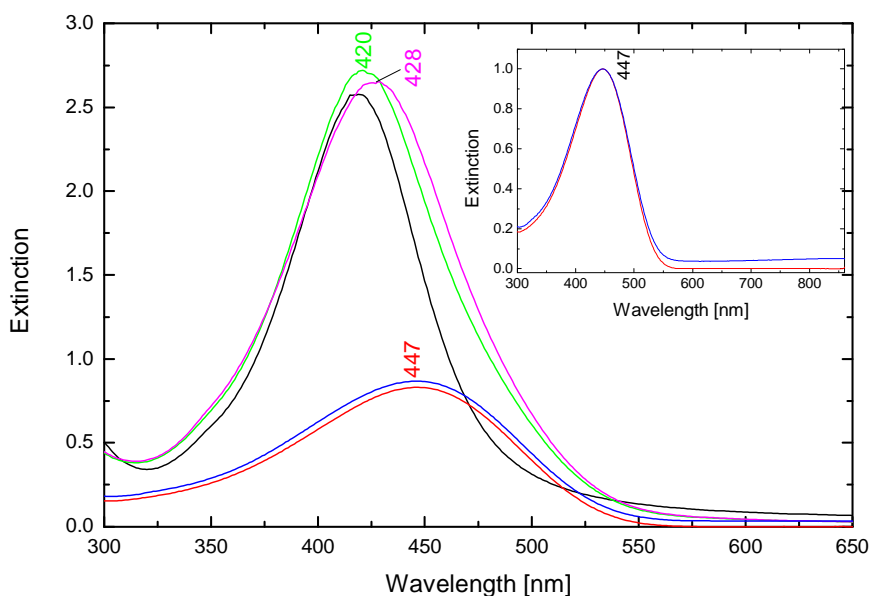


Figure 4.3-13. SPE spectra of Ag(TDAB)/P3OT composite type **M** taken immediately after the mixing of component (green line), 120 min after the mixing (purple line) and after the precipitation in methanol and redissolution in toluene (blue line). SPE spectrum of Ag organosol (black line) and absorption spectrum of neat polymer (red line) are plotted for comparison. Comparison of absorption spectrum of the neat polymer (red line) and SPE spectrum of the composite after the precipitation and redissolution in toluene (blue line) is shown in Inset.

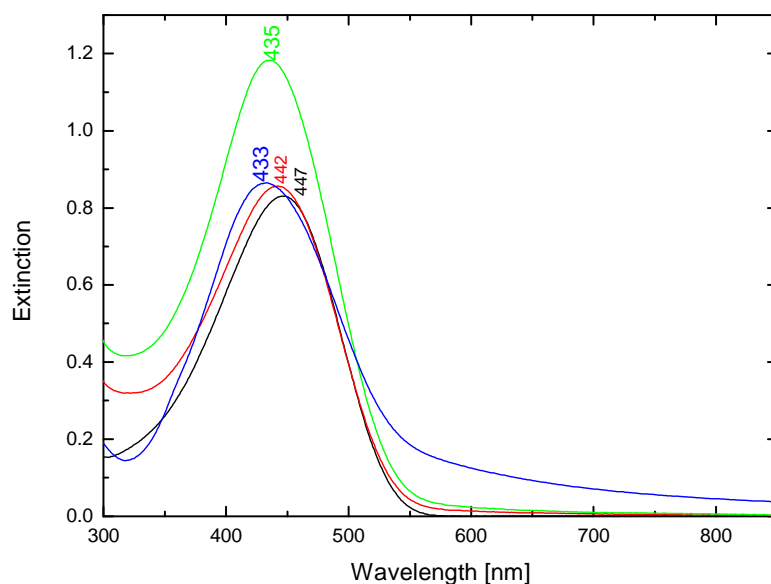


Figure 4.3-14. SPE spectra of Ag(TDAB)/P3OT composite type **R** taken 5 min after reductant addition (red line), 120 min after reductant addition (green line) and after the precipitation in methanol and redissolution in toluene (blue line). Absorption spectrum of the neat polymer is depicted as a black line.

4.3.3.2. Transmission electron microscopy (TEM)

At first, the morphology of Ag NPs in Ag/P3OT composites obtained using TOAB before and after the precipitation will be discussed. TEM images of these composites are depicted in Figure 4.3-15. Similarly to Au NPs containing composites, the globular structures are observed in TEM images (Figure 4.3-15a,b) of Ag/P3OT composites before the precipitation. However, the density of particles is much lower compared to Au/P3OT composites. It corresponds to the decrease in NPs content during the composite preparations. In Ag/P3OT composite type **R**, markedly more NPs are found outside globular structures (Figure 4.3-15b). After the precipitation and redissolution in toluene, the globular structures disappear and the NPs are scattered over the whole image (Figure 4.3-15c,d). The image analysis of NP sizes (Figure 4.3-16) shows that both procedures lead to very small nanoparticles of similar size, $d \approx 3$ nm, for both composites.

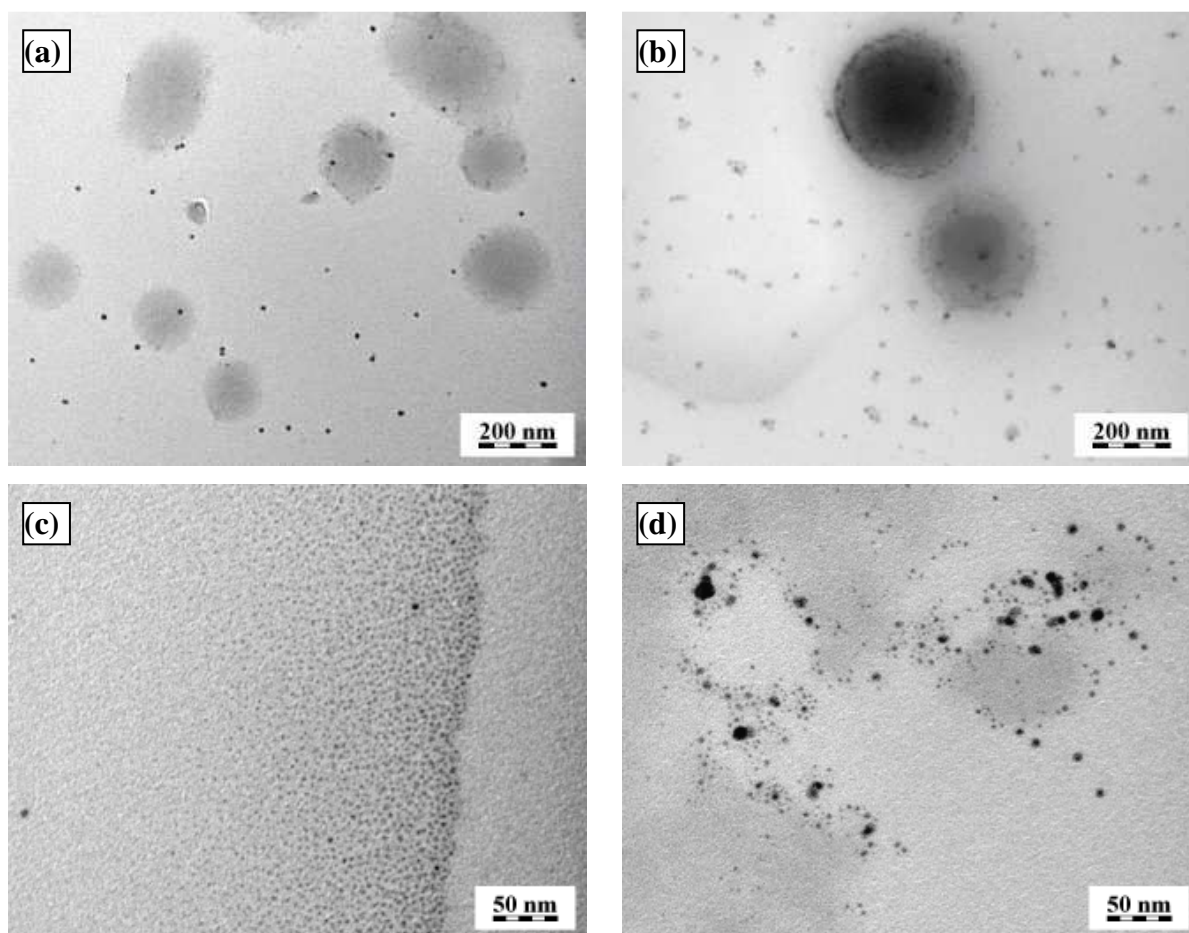


Figure 4.3-15. TEM images of Ag(TOAB)/P3OT composites type **M** (a,c) and type **R** (b,d) before the precipitation (a,b) and after the precipitation in methanol and redissolution in toluene (c,d).

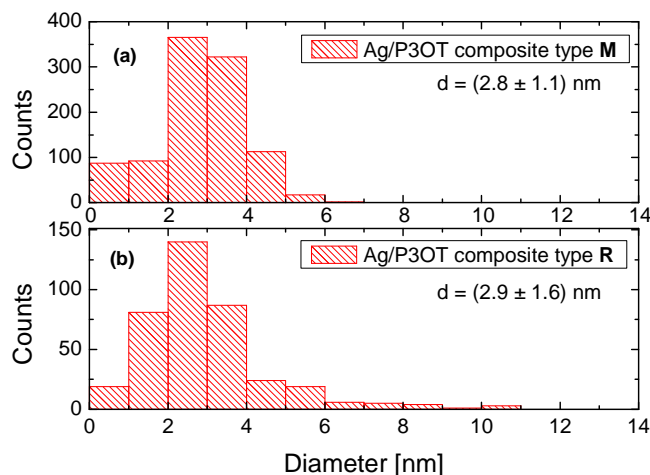


Figure 4.3-16. Nanoparticle size distributions in Ag(TOAB)/P3OT composites (a) type **M** and (b) type **R**.

Figure 4.3-17 shows the TEM images of Ag NPs in Ag(TDAB)/P3OT composites before the precipitation as well as after the precipitation and redissolution in toluene. Surprisingly, the globular structures are not observed even before precipitation (Figure 4.3-17a,b). The isolated particles are localized in small 2-D assemblies. The precipitation has significant influence on the nanoparticle morphology. In case of composite type **M**, the particles have tendency to aggregate into large aggregates with sizes in order μm (Figure 4.3-17c). The detail image (Figure 4.3-17e) shows that these aggregates are formed by intergrown particles. Aggregate formation occurs also in composite type **R** after the precipitation as shown in Figure 4.3-17d. Nevertheless, the aggregates are smaller in size. They are formed by larger intergrown particles surrounded by smaller separated particles.

The results presented above show that preparation procedure influences significantly the morphology of Ag NPs in the resulted Ag(TDAB)/P3OT nanocomposites in contrast to Au/P3OT composites. In case of composites type **M**, the particles are originally stabilized by the phase-transfer agent (TOAB or TDAB). Mixing of particles with P3OT should lead to a stabilizer exchange, replacement of the molecules of phase transfer agent by the polymer chains. Removal of phase-transfer agent by precipitation in methanol should lead to composites containing metal NPs stabilized mostly by the polymer. The presence of small separated Au NPs in Au/P3OT composites (Figure 4.3-9) indicates that P3OT acts as a good stabilizer of Au NPs. On the other hand, the presence of large intergrown aggregates in Ag(TDAB)/P3OT composites type **M** shows that P3OT only poorly stabilizes Ag NPs in this composite and, therefore, the removal of the phase transfer agent by precipitation leads to fusion of particles. Another possible explanation for the presence of such large aggregates can

be formation of Ag Br species on Ag NP surface since bromide ions have a good affinity towards Ag surface¹⁶⁸. To confirm this hypothesis, EDAX analysis has to be performed.

In case of *in situ* preparation of composites type **R**, it is believed that the particles are stabilized by the polymer and/or by the phase-transfer agent since both possible nanoparticle stabilizers are present in the course of the formation of nanoparticles during the *in situ* preparation. The presence of small Ag NPs and smaller NP aggregates in Ag(TDAB)/P3OT composites type **R** compared to large intergrown aggregates in composites type **M** shows that *in situ* procedure seems to be more suitable for the preparation of composites containing Ag NPs than merely mixing of the components since the stabilization of nanoparticles by the polymer in the composites type **R** is more efficient than in the composite type **M**. In summary, while both procedures can be used for the preparation of composites containing Au NPs, *in situ* procedure is more suitable for the preparation of polymer composites containing Ag NPs.

TEM imaging was followed by EDAX analysis to elucidate possible formation of AgBr species on Ag NP surface in Ag/P3OT composites. EDAX analysis (Figure 4.3-18) showed that bromide ions remain in the Ag(TDAB)/P3OT nanocomposites even after the precipitation. Since EDAX is sensitive to the species present only on the surface of strongly electron absorbing material in the focused electron beam, the observed signal can be ascribed to the Br atoms present on Ag NP surface. It thus confirms the affinity of bromide ions to silver surface leading to formation of bromide-modified Ag NPs and these bromides cannot be removed by purification. The adsorbed bromides on the Ag NP surface facilitate the formation of intergrown aggregates (Figure 4.3-17c-f) after Ag/P3OT composite purification.

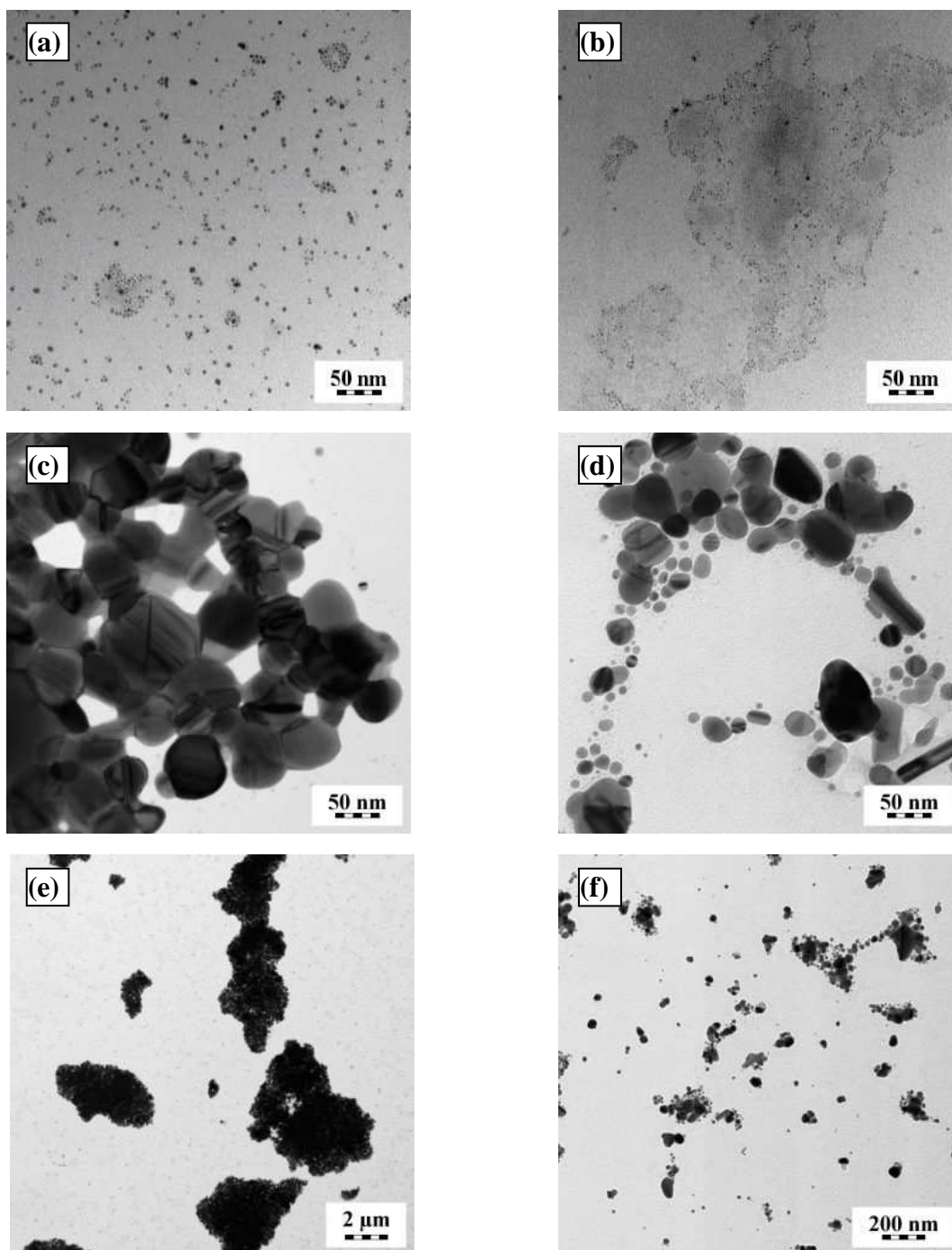


Figure 4.3-17. TEM images of Ag(TDAB)/P3OT composites type (a,c,e) **M** and (b,d,f) **R** before the precipitation (a,b) and after the precipitation in methanol and redissolution in toluene (c-f).

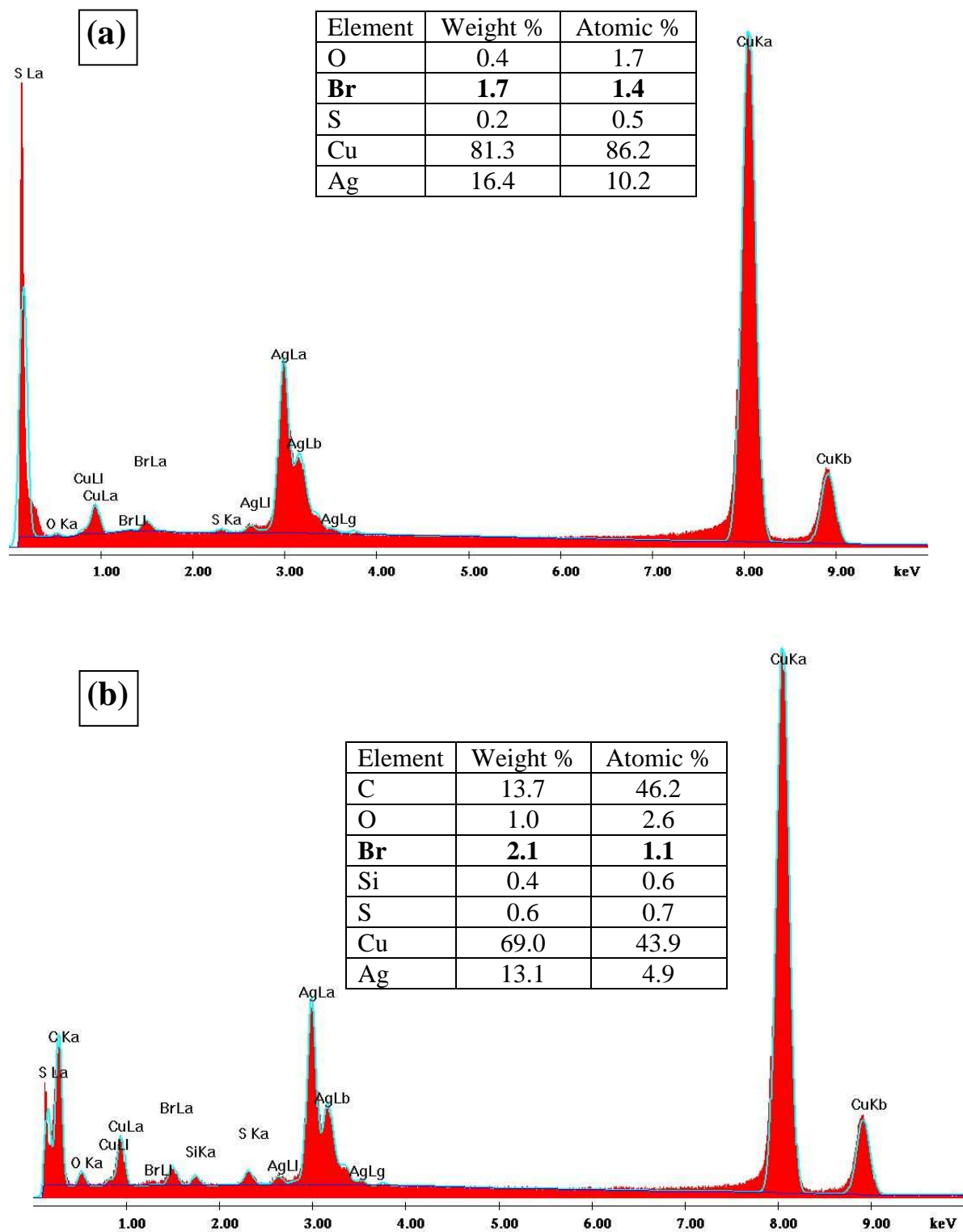


Figure 4.3-18. EDAX spectra of Ag NP aggregates in Ag(TDAB)/P3OT composite (a) type **M** and (b) type **R** after the precipitation in methanol and redissolution in toluene.

4.3.3.3. Dynamic light scattering (DLS)

Hydrodynamic diameters determined for Ag/P3OT composites are shown in Table 4.3-4. Similarly to Au NPs containing composites, the diameters found by DLS markedly exceed the values obtained from TEM imaging. It indicates that Ag NPs in composite solutions are present in larger assemblies or in associates formed by the NPs and by the polymer. The largest hydrodynamic diameter is obtained for Ag(TDAB)/P3OT composite type **M**. It is in agreement with TEM observation where large intergrown Ag aggregates are present (Figure 4.3-17c). Smaller diameter of nanoparticle assemblies was found for Ag(TOAB)/P3OT composite type **M**. For composites type **R**, bimodal size distributions were obtained. Smaller sizes of both nanoparticle fractions were observed for Ag(TDAB)/P3OT composite compared to the sizes of Ag(TOAB)/P3OT composite. For Ag(TDAB)/P3OT composite type **R**, the hydrodynamic diameter of fraction of particles with smaller size could correspond to small separated nanoparticles and/or small aggregates of several particles which were found in TEM image of this composite (Figure 4.3-17d). The second nanoparticle fraction with larger hydrodynamic diameter could be assigned to larger NP aggregates which were also observed in TEM image together with small NPs.

	composite type M	composite type R
Ag(TOAB)/P3OT	$d = (248.56 \pm 14.27) \text{ nm}$	$d_1 = (96.65 \pm 7.60) \text{ nm}$ $d_2 = (374.35 \pm 7.87) \text{ nm}$
Ag(TDAB)/P3OT	$d = (867.93 \pm 50.38) \text{ nm}$	$d_1 = (21.52 \pm 4.25) \text{ nm}$ $d_2 = (90.93 \pm 2.67) \text{ nm}$

Table 4.3-4. Hydrodynamic diameters in Ag/P3OT composites determined by DLS measurement.

4.3.4 Raman spectroscopy

4.3.4.1. SERS spectra of Au/P3OT composites

Raman spectra of Au(TOAB)/P3OT composites as well as of the neat polymer are shown in Figure 4.3-19a. The spectra were measured from thin films prepared according to the procedure described in Chapter 3.3. The positions of the most characteristic bands were assigned on the basis of earlier published results of SERS spectral measurements of polyalkylthiophenes cast on roughened gold electrodes^{126, 173}. The most intensive bands at 1444 cm^{-1} and 1380 cm^{-1} were assigned to the $C_{\alpha} = C_{\beta}$ symmetric stretching mode and to the $C_{\beta} - C_{\beta'}$ single bond stretching mode of the thiophene ring, respectively. The ratios of the integral intensities of these two bands for composite samples, known to be sensitive to the polymer oxidation^{126, 174}, remained the same in both types of the composites as for the neat P3OT. The band at 727 cm^{-1} (C-S-C ring bending) as well as the positions of Raman bands at 1509, 1208, 1198, 1182, 1090, 1013 and 598 cm^{-1} are the same as those reported for P3OT, e.g. in the paper by Baibarac and coworkers¹⁷³.

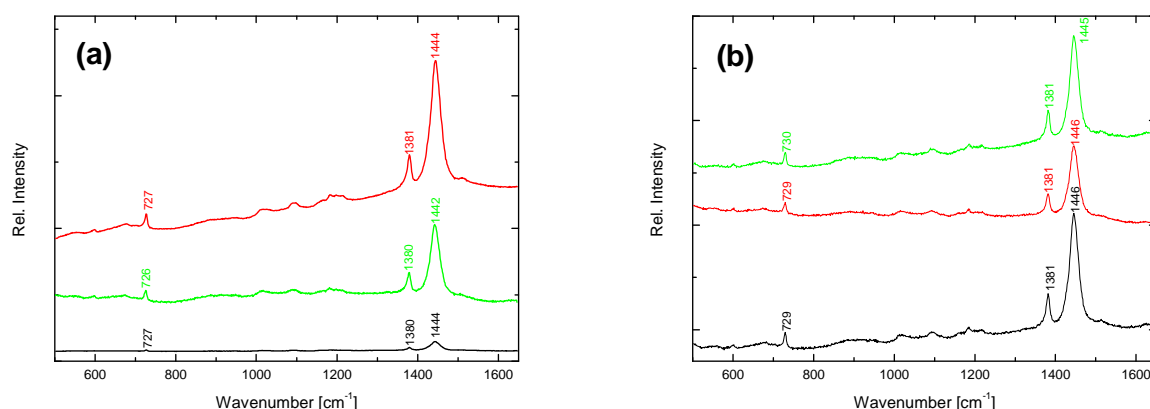


Figure 4.3-19. Raman spectra of (a) Au(TOAB)/P3OT composites and (b) Au(TDAB)/P3OT composites taken with 632.8 nm excitation wavelength. Composites type **M** are depicted as red curves, composites type **R** as green curves, neat P3OT (black curves) are shown for the comparison.

It is obvious that Raman spectra of the composite samples yielded enhanced Raman signal with clearly observable bands typical for polythiophene (Figure 4.3-19). The integrated relative intensities of the most intense Raman bands at 1444 cm^{-1} are more than ten times higher for the composites compared to the pure polymer (as follows from the results of the band decomposition and integration procedure). The enhancement is more pronounced for composite type **M** compared to that for composite type **R**. To enable an explanation of different surface enhancement of Raman scattering of each of the composite samples, the

morphology and optical responses of Au NPs in the thin films of composite samples have been investigated by SPE spectral measurements and SEM imaging.

Firstly, UV-Vis (i.e. SPE of Au NPs and polymer absorption) spectra of the composites were measured on the same films as employed for the Raman measurement. These spectra as well as the absorption spectrum of the neat polymer are compared in Figure 4.3-20a. The spectra of the composites show an increased extinction compared to the absorption of the neat polymer. It can be ascribed to the SPE of Au NPs or NP aggregates. Moreover, the extinction above 700 nm for composite type **M** is slightly higher than that for composite type **R**. Since extinction in this wavelength region mostly corresponds to the presence of nanoparticle aggregates, its increase could indicate that composite **M** has a higher content of the aggregates than composite **R**.

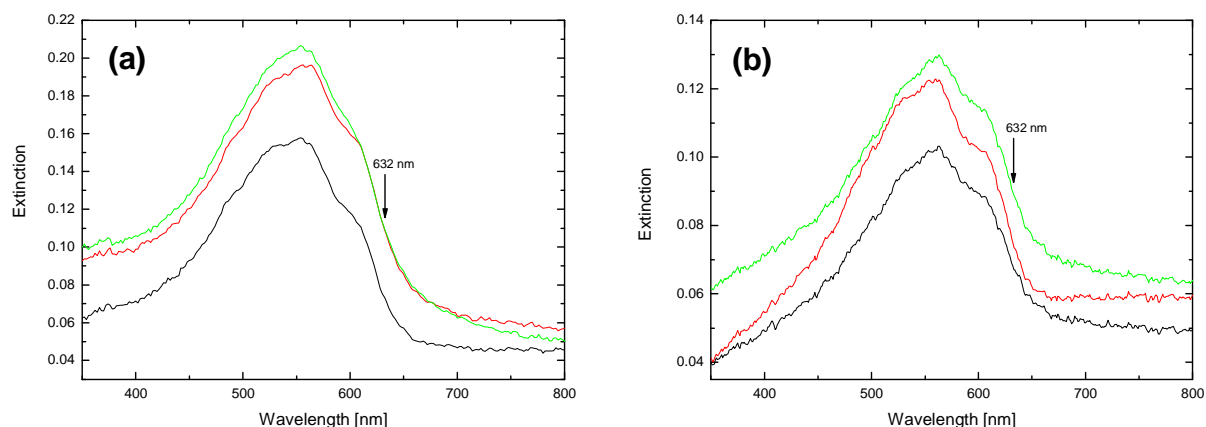


Figure 4.3-20. SPE spectra of thin films of (a) Au(TOAB)/P3OT composites and (b) Au(TDAB)/P3OT composites. Composites type **M** are depicted as red curves, composites type **R** as green curves and neat P3OT - black curves is shown for the comparison.

SEM images of composite films (Figure 4.3-21a, b) show that the morphologies of Au NPs in each of them are, indeed, different. In composite type **M**, large NP aggregates together with small aggregates or isolated particles are observed. The presence of large aggregates was also confirmed by optical microscopy imaging during micro-Raman spectra measurement. This observation is somewhat surprising, because only small isolated Au NPs were found in the TEM images of the deposited composite (Figure 4.3-9a). It should be mentioned that the preparation of films by spin-coating technique was repeated and the same morphology of composite type **M** was obtained. It thus seems that an application of the spin-coating technique of the film preparation plays a key role in the formation of such Au NP aggregates in these composites since it is generally known that morphology of polythiophene layer depends strongly on the condition of film preparation, namely, on the rate and duration of

solvent vaporization¹⁷⁵. On the other hand, such large aggregates are not present in the film of composite type **R**, which is constituted by small aggregates of Au NPs.

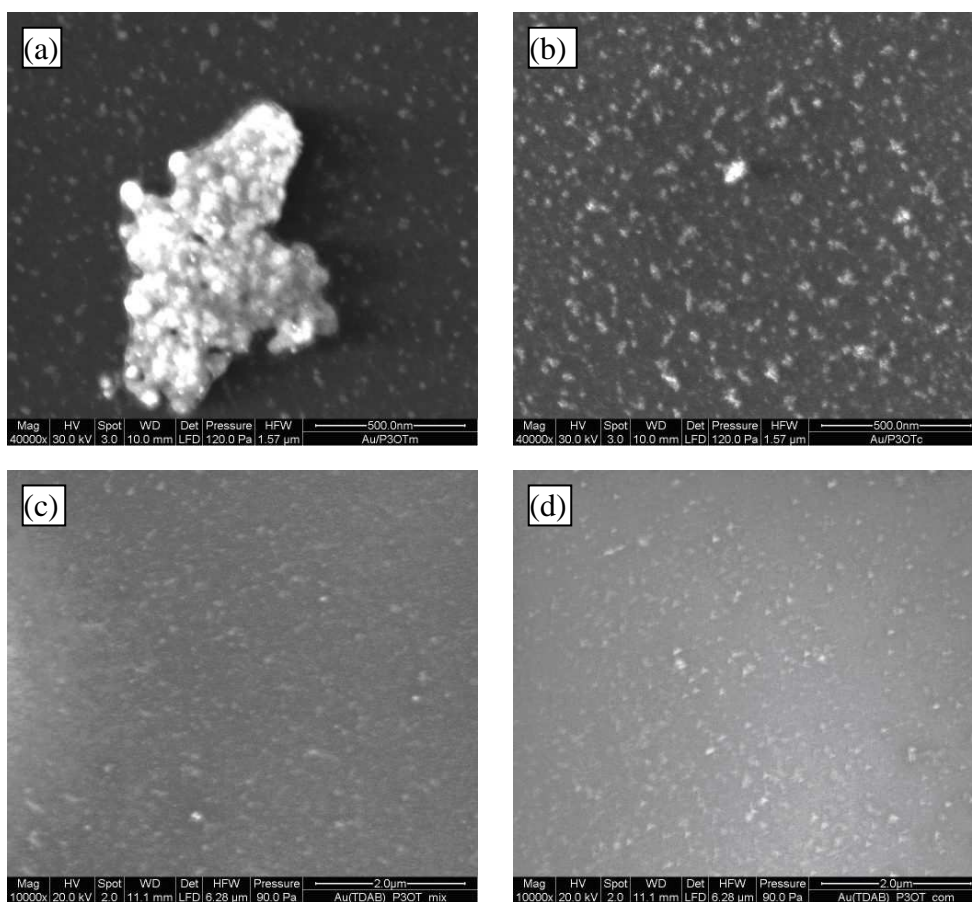


Figure 4.3-21. SEM images of films of Au(TOAB)/P3OT composites type (a) **M** and (b) **R** and of Au(TDAB)/P3OT composites type (c) **M** and (d) **R**.

The surface enhancement of the polymer Raman signal observed for these composite samples can be now more clearly explained. The enhancement is more pronounced for composite type **M** since it contains large NP aggregates. These aggregates can act as the carriers of „hot spots“, i.e. strong, nanoscale localized optical fields, from which strongly enhanced SERS signal of the polymer originates. The enhancement can be explained by an electromagnetic amplification mechanism in the presence of the plasmonic nanostructures (large Au NP aggregates for composite type **M** and small Au NP aggregates for composite type **R**). The absence of any shifts of the polymer Raman bands in the composites compared to the pure polymer indicates that the polymer is not chemisorbed on Au NPs. Therefore, the observed enhancement can be attributed only to the electromagnetic (EM) mechanisms of SERS. The largest contribution to the SERS signal originates from the polymer segments

localized in the vicinity of Au NPs surfaces, or even more probably, in the strong optical fields localized in interstices between the rather closely spaced Au NPs.

Raman spectra of composites prepared by using TDAB were also obtained with the 632.8 nm excitation. Raman spectra (Figure 4.3-19b) of the composite samples show no detectable enhancement of the Raman signal of the polymer. SPE spectra and corresponding SEM images of the composites are shown in Figure 4.3-20b and Figure 4.3-21c,d. The morphologies of Au NPs in both composite samples **M** and **R** are very similar: small Au NPs and/or small NP assemblies are observed. Therefore, the lack of the enhancement of Raman signal obtained with 632.8 nm excitation can be explained by the absence of nanoparticle aggregates in the spin-coated samples of the Au(TDAB)/P3OT composites.

4.3.4.2. SERS spectra of Ag/P3OT composites

Raman spectra of thin films of Ag/P3OT composites spin-coated on glass substrates have been measured and interpreted. For the Ag/P3OT composites prepared using TOAB, no changes in Raman spectra were observed. It was attributed to a low content of Ag NPs in the resulted composites and to the small size of nanoparticles (less than 3 nm). Such small nanoparticles do not show surface plasmon resonance.

On the other hand, Raman spectra of Ag/P3OT composites prepared using TDAB revealed some interesting features. Prior to the interpretation of Raman measurements, a special attention was paid to SPE spectral measurements and SEM imaging of composite films since variations of the plasmonic metal nanoparticle morphologies and their optical responses can substantially influence the Raman signal enhancement, as it was demonstrated in the previous chapter.

UV-Vis spectra (SPE of Ag NPs and polymer absorption) of the films of Ag(TDAB)/P3OT composites type **M** and **R** as well as neat P3OT are depicted in Figure 4.3-22. First, a slight increase in absorption above 700 nm observed for the neat polymer was assigned to the interference due to the reflections within films cast on a glass substrate. SPE spectrum of the

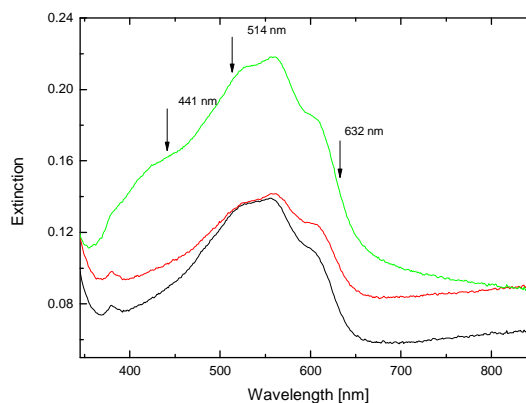


Figure 4.3-22. SPE spectra of Ag(TDAB)/P3OT composites type **M** (red curve) and **R** (green curve). Absorption spectrum of neat P3OT film (black curve) is shown for comparison.

composite type **M** is similar to the absorption spectrum of neat P3OT; however, an increase in extinction in spectral regions 340 – 470 and 600 – 800 nm is observed for the composite. This increase could correspond to the presence of Ag NP aggregates rather than of isolated NPs. Compared with the spectrum of the neat P3OT, the spectrum of composite **R** (green curve) contains the additional band in the 360 – 450 nm spectral range. It could be assigned to the extinction of small isolated Ag NPs (for example, SPE band of a hydrosol containing ca. 9 nm Ag NPs shows a maximum at 398 nm) and smaller aggregates.

SEM images (Figure 4.3-23) show the morphology of Ag NPs in composite films. The morphological features of the spin cast films are analogous to those observed earlier in the TEM images of the composites deposited on carbon coated grid (Figure 4.3-17). In particular, the composite type **M** contains large fused Ag NP aggregates while small isolated Ag NPs or smaller aggregates are found in composite type **R**. Different morphology of the composite samples could cause a different localization of electric field intensities upon laser excitation.

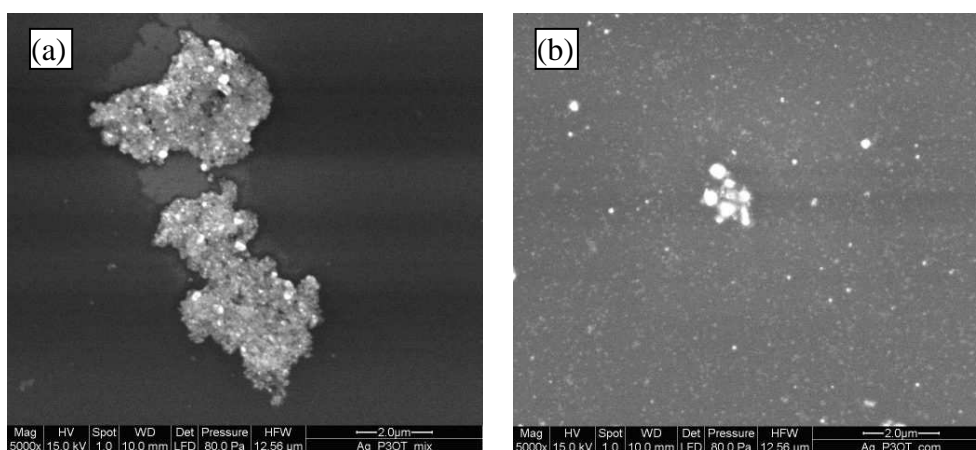


Figure 4.3-23. SEM images of spin cast films of Ag(TDAB)/P3OT composites (a) type **M** and (b) type **R**.

Raman spectra of the composites type **M** and **R** and of the neat polymer (Figure 4.3-24) were measured at various laser excitation wavelengths (441.6, 514.5 and 632.8 nm) to evaluate the Raman signal enhancement to the observed spectra.

Excitation with 632.8 nm wavelength. The spectra of the Ag/P3OT composites type **M** and **R** as well as of the neat polymer taken with 632.8 nm wavelength depicted in Figure 4.3-24c are identical. The wavenumbers of all bands are the same in the spectra of the composites as in the spectrum of the polymer. Therefore, chemisorption of the polymer on Ag NPs and the possibility of formation of a charge-transfer complex can be excluded. Moreover,

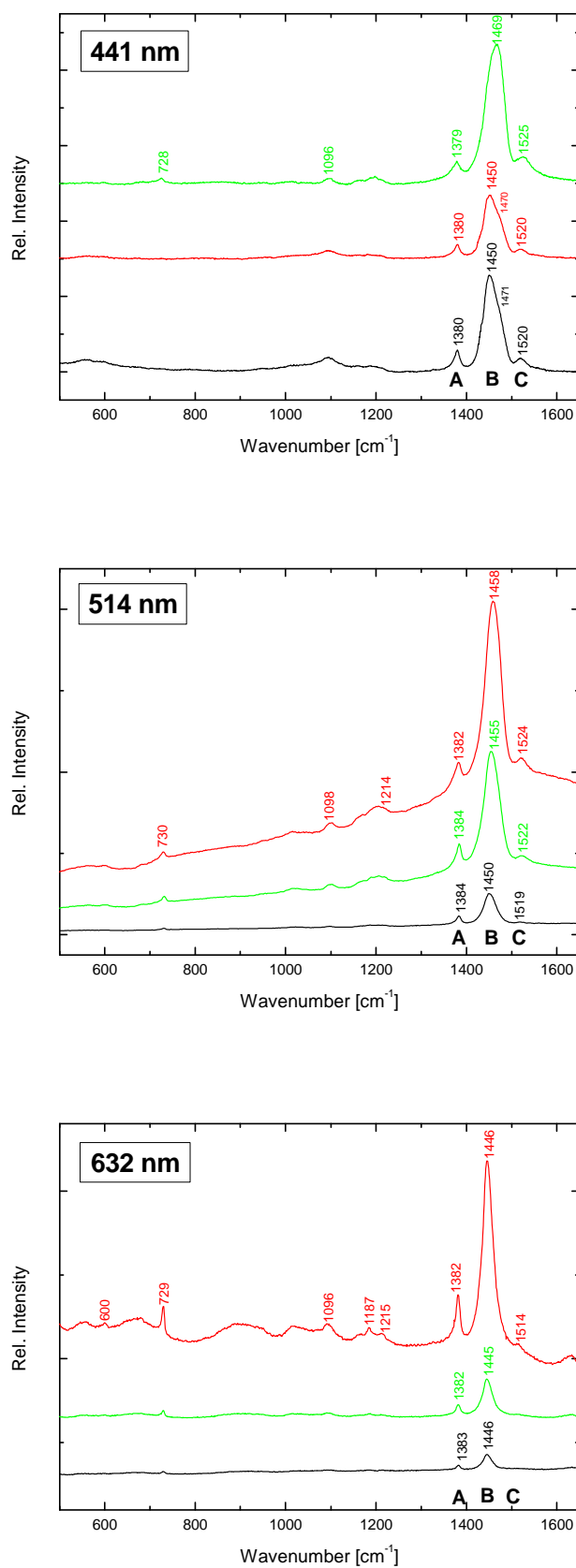


Figure 4.3-24. SERS spectra of Ag(TDAB)/P3OT composites type **M** (red spectra), type **R** (green spectra) and Raman spectra of neat P3OT (black spectra) measured at various excitation lines.

the wavenumbers of Raman bands are in agreement with those observed in the spectra of Au/P3OT composites and neat polymer excited at the same wavelength (632.8 nm, see Figure 4.3-19). The most intense bands at 1383 and 1446 cm^{-1} are assigned to $\text{C}_\beta\text{-C}_\beta$ stretching and $\text{C}_\alpha=\text{C}_\beta$ ring stretching vibrations^{126, 173}, respectively, and they are denoted within the text as band **A** and **B**.

Excitation with 441.6 nm wavelength. The Raman spectra of Ag/P3OT composites and neat polymer are depicted in Figure 4.3-24a. At a first glance, the substantial changes occur in these spectra in comparison to those excited at 632.8 nm (Figure 4.3-24c). Namely, the position and/or the shape of the band **B** change. In the spectra of the neat polymer and composite type **M**, the band **B** at 1450 cm^{-1} is markedly asymmetric with a shoulder around 1470 cm^{-1} , while in the spectrum of composite type **R**, this shoulder increases in intensity and determines the actual position of the band **B**. Therefore, a relatively large shift of the band **B** is observed (from 1450 cm^{-1} to 1469 cm^{-1}).

It should be mentioned that the spectra of the neat polymer and composite type **M** resemble the Raman spectrum of P3OT obtained at 457 nm excitation in ref.¹⁷⁶, in which a similar shoulder has been observed. The main band and the shoulder can be related to the different polymer structures. In ref.¹⁷⁷, two limiting molecular conformations of the polymer side chain are described. The ordered structure corresponding to the planar conformation of the thiophene main chains with all-*trans* methylene side chains at low temperatures gives rise to the absorption band at about 500 nm. A blue shift of the absorption band is observed for the disorder twisted main chain conformation with random-coiled methylene side groups at high temperatures. At room temperature (our case), both structures coexist in the polymer sample. Upon 441.6 nm excitation, Raman spectra of the polymer chains with short conjugation lengths (disordered structures) are resonantly excited. It can be proposed that the shoulder at 1470 cm^{-1} is probably related to this disordered structure. It seems that the presence of small isolated Ag NPs and small aggregates in the composite type **R** affects the crystallinity of the polymer chains and therefore the shoulder at 1470 cm^{-1} in this composite dominates in comparison to the spectra of the neat polymer and the composite type **M**. Furthermore, the shift of the band **B** from 1446 (632.8 nm excitation) to 1450 cm^{-1} (441.6 nm excitation) observed for the neat polymer and composite type **M** can be related to the effect of Raman dispersion or to the presence of a small fraction of disordered structure with shorter conjugation length which manifests itself by a shoulder at 1470 cm^{-1} .

In the spectra of the neat polymer as well as of both composites, a new band at 1520 cm^{-1} (1525 cm^{-1}) denoted as band **C** emerges. In particular, the wavenumber of the band

C in the Raman spectra of neat polymer and the composite **M** is 1520 cm^{-1} , while a shift of this band to 1525 cm^{-1} is encountered in the spectrum of composite **R**. This band is assigned to the $C_{\alpha}=C_{\beta}$ ring stretching vibration¹⁷⁸. A question has arisen if the shift of this band **C** is related to the shift of the band **B**. The answer to this question has emerged from interpretation of the Raman spectra measured with 514.5 nm excitation.

Excitation with 514.5 nm wavelength. Raman spectra of the neat polymer and the composites obtained using 514.5 nm excitation wavelength are shown in Figure 4.3-24b. The spectrum of the neat polymer shows the **B**-band position at the same wavenumber (1450 cm^{-1}) as that excited at 441.6 nm but without the shoulder at 1470 cm^{-1} . For composites **M** and **R**, the shifts of the band **B** with respect to the band for the neat polymer are observed. The most pronounced shift of the band **B** to 1458 cm^{-1} is observed for composite **M**, while in composite **R**, this band is shifted to 1455 cm^{-1} . The band **C** simultaneously shifts to higher wavenumbers in comparison with that for the neat polymer (1519 cm^{-1} (P3OT) \rightarrow 1522 cm^{-1} (**R**) \rightarrow 1524 cm^{-1} (**M**)). It is thus clearly seen that the shift of the band **C** is related to the shift of the band **B**. The simultaneous shifts of bands **B** and **C** in the spectra of the composites are consistent with their assignment since the bands belong to the $C_{\alpha}=C_{\beta}$ and $C_{\alpha}=C_{\beta}$ stretching vibrations of thiophene ring, respectively.

The origin of appearance of the band **C** and the changes of the band **B** with excitation wavelength have been examined on bases of determination of relative band intensities ratios $I(\mathbf{B})/I(\mathbf{A})$ and $I(\mathbf{C})/I(\mathbf{A})$. The ratios were related to the intensity of the band **A** since its intensity and position remains unchanged for all used excitation wavelengths. This analysis could provide the elucidation if the molecular resonance and/or EM enhancement of SERS, relation to the presence of disordered structures are responsible for the observed spectral changes.

The values of ratios of $I(\mathbf{B})/I(\mathbf{A})$ and $I(\mathbf{C})/I(\mathbf{A})$ band intensities are presented in Table 4.3-5 and Table 4.3-6. For the neat polymer, only the molecular resonance enhancement is expected. The ratio $I(\mathbf{B})/I(\mathbf{A})$ decreases as the excitation wavelength increases. The lowest value is achieved at 632.8 nm excitation since this excitation wavelength only poorly matches the absorption spectrum of the polymer. The 514.5 nm excitation wavelength falls nearly into the maximum of the absorption spectrum of the polymer and therefore the maximal value of the ratio $I(\mathbf{B})/I(\mathbf{A})$ should be achieved. However, the larger value of the ratio $I(\mathbf{B})/I(\mathbf{A})$ is obtained at 441.6 nm excitation. It can be explained by the presence of the polymer disordered structures which are resonantly enhanced at this excitation and which manifest itself as a shoulder of the band **B**. Therefore, the intensity of this band is larger at 441.6 nm

excitation than that obtained using 514.5 nm excitation. Also the value of the ratio $I(\mathbf{C})/I(\mathbf{A})$ has larger value at 441.6 nm excitation than that obtained using 514.5 nm excitation.

The values of the ratio $I(\mathbf{B})/I(\mathbf{A})$ determined for both composites for 632.8 nm excitation are similar to the value determined for the neat polymer. For composite type **R**, the values of the ratio $I(\mathbf{B})/I(\mathbf{A})$ increase with decreasing excitation wavelength analogously with these values determined for the neat polymer. However, the values determined for 514.5 and 441.6 nm excitations are much greater than those for the neat polymer. Moreover, the increasing trend of values of ratio $I(\mathbf{B})/I(\mathbf{A})$ with decreasing excitation wavelength is not fulfilled for composite type **M** since the maximal value is achieved for 514.5 nm excitation wavelength. The values of the ratio $I(\mathbf{C})/I(\mathbf{A})$ for composites exhibit also differences in comparison to those determined for the neat polymer: for composite type **R**, the values are greater than those for the polymer and, for composite type **M**, the maximal value is achieved at 514.5 nm excitation. The described changes in the values of ratios $I(\mathbf{B})/I(\mathbf{A})$ and $I(\mathbf{C})/I(\mathbf{A})$ show that the Raman signal enhancement can not be explained only by molecular resonance contribution. Therefore, the contribution of surface-enhancement could be considered.

Sample	$I(\mathbf{B})/I(\mathbf{A})$		
	$\lambda_{\text{exc}} = 441.6 \text{ nm}$	$\lambda_{\text{exc}} = 514.5 \text{ nm}$	$\lambda_{\text{exc}} = 632.8 \text{ nm}$
neat P3OT	18	11	8
composite type M	14	30	11
composite type R	31	18	9

Table 4.3-5. Mutual ratios of the **B** and **A** bands intensities.

Sample	$I(\mathbf{C})/I(\mathbf{A})$	
	$\lambda_{\text{exc}} = 441.6 \text{ nm}$	$\lambda_{\text{exc}} = 514.5 \text{ nm}$
neat P3OT	0.7	0.2
composite type M	0.4	0.6
composite type R	1.2	0.3

Table 4.3-6. Mutual ratios of the **C** and **A** bands intensities.

The SPE spectra of the composites (Figure 4.3-22) as well as the morphologies of Ag NPs in the composite samples (Figure 4.3-23) have to be considered for elucidation of surface-enhancement of their Raman signal. The excitation at 441.6 nm coincides with extinction of Ag NPs manifesting itself as a shoulder between 375 – 445 nm in the SPE

spectrum of the composite type **R** while 514.5 nm excitation matches the SPE spectrum of the composite type **M** containing large aggregates (Figure 4.3-22) showing extinction above 500 nm. From the ratios of the $I(\mathbf{B})/I(\mathbf{A})$ band intensities (Table 4.3-5) it is seen that the ratio reaches the maximal value when the laser excitation wavelength coincides with the SPE spectral features (bands or shoulders) of the particular composite sample. For the composite type **M**, the maximal value of the ratio $I(\mathbf{B})/I(\mathbf{A})$ is achieved at 514.5 nm excitation while for the composite type **R** the maximal value corresponds to 441.6 nm excitation. Similarly, the ratio $I(\mathbf{C})/I(\mathbf{A})$ (Table 4.3-6) is maximal for the cases when the excitation coincides with SPE spectral features of the particular composite sample.

In summation, the observed changes in Raman spectra of Ag/P3OT composites, in particular the change in both the shape and intensity of the band **B** and appearance of the band **C**, can be ascribed to the combination of molecular resonance and surface-enhancement electromagnetic contributions. At 441.6 nm excitation, disordered structures of the polymer with shorter conjugation length are resonantly enhanced. For the composite type **M**, the molecular resonance enhancement dominates the spectral pattern, since the extinction of Ag nanostructures in this composite is only very weak at this wavelength. The resonance enhancement manifests itself as a shoulder of the band **B** at 1470 cm^{-1} . On the other hand, for the composite type **R**, this shoulder becomes the main band. This band, apparently, gains its spectral intensity from both the molecular resonance and from surface-enhancement, since the 441.6 nm excitation wavelength coincides with a pronounced extinction of Ag nanostructures present in this composite. Therefore, it is expected that the polymer chains with shorter conjugation length are preferentially localized in the interstices of Ag NPs and/or NP aggregates. At 514.5 nm excitation, the surface-enhancement is achieved for the composite type **M** since the excitation wavelength matches the extinction of large intergrown aggregates which are present in the composite. Furthermore, the shift of the band **B** is related to the shift of the band **C**. It can be explained by the fact that the bands are assigned to the $C_{\alpha}=C_{\beta}$ and $C_{\alpha'}=C_{\beta'}$ stretching vibrations of thiophene ring, respectively.

In the previously published papers, SERS spectra of polyalkylthiophenes were obtained on a roughened Ag electrode^{123, 124, 174} as well as in Ag colloid¹²⁶ at 514.5 nm excitation wavelength. Electrodeposition of P3OT film onto Ag plates led to the amplification of Raman bands of the polymer which was assigned to SERS effect combined with a resonance contribution. The shifts of Raman bands were not observed. For measurement of SERS spectra of P3OT (dissolved in THF) in Ag hydrosol the addition of sodium nitrate was required which caused the aggregation of the hydrosol. Well resolved SERS spectra recorded

at 514.5 nm laser excitation were obtained at very low concentration of the polymer (10^{-7} - 10^{-8} M). The most significant changes in Raman spectrum accompanied by the shifts of Raman bands were observed for polymethylthiophene¹²⁶; in particular, the shift of the band **B** to 1461 cm^{-1} was found. These published results obtained for polyalkylthiophenes adsorbed on Ag NPs are in a good agreement with observation obtained for the composite type **M** at the same excitation wavelength (514.5 nm) in this study. There is thus the evidence that the polymer chains are in interaction with Ag NP aggregates or, alternatively, that the polymer chains are localized in hot spots of Ag NP aggregates.

4.3.5. Conclusions

1. Phase transfer agent used in organosol preparation influences the stability of the metal NPs during as well as after the preparation. While both TDAB and TOAB can be used for the preparation of Au organosols, for Ag organosol preparation it is better to use TDAB since Ag organosol prepared using TOAB is non-stable in time.
2. Precipitation of composite solutions in methanol (step in composite preparation) has significant impact on NPs morphology. Globular structures with the concentration of Au NPs on their perimeter were present in Au/P3OT composites before precipitation while well separated particles were observed after the precipitation and redissolution of composites. It was found that the formation of such globular structures is influenced by the presence of a phase transfer reagent (tetraoctylammonium bromide) as well as P3OT in the solution of Au/P3OT composites. In Ag/P3OT composites prepared using TDAB, formation of large intergrown nanoparticle aggregates was observed after the composite precipitation and its redissolution.
3. The difference in morphology of NPs in the resulted Au/P3OT and Ag/P3OT composites (small separated particles in Au/P3OT composites and large aggregates in Ag/P3OT composites) was assigned to higher adsorption affinity of bromide ions originated from the phase transfer agent to Ag NP surface compared with that to Au NP surface. Bromide ions can not be removed from Ag NP surface by precipitation and, therefore, intergrown NP aggregates are formed in Ag/P3OT composites.

4. The presence of smaller NP aggregates and small isolated Ag NPs in Ag/P3OT composites type **R** compared to large intergrown aggregates in composites type **M** indicates that *in situ* procedure seems to be more suitable for the preparation of P3OT composites containing Ag NPs than merely mixing of the components since the stabilization of nanoparticles by the polymer in the composites type **R** is more efficient than in the composite type **M**. On the other hand, both procedures can be equally used for the preparation of P3OT composites containing Au NPs since they provide similar nanoparticle size and nanoparticle size distribution.
5. SERS spectra of the composites of P3OT and metal NPs showed to be strongly affected by the morphology of metal NPs in the composite films. Interestingly, more than ten-fold enhancement of Raman scattering for Au/P3OT composite type **M** containing large nanoparticle aggregates was observed upon excitation with 632.8 nm wavelength. It was attributed to the EM mechanisms of SERS. SERS/SERRS spectral probing of Ag/P3OT composites type **M** and **R** enabled to pinpoint the mutual difference in the polymer structures encountered within each of them, in particular the dominance of the disordered structure in the composite type **R**.

4.4. Polymer composites containing Au nanoparticles and poly[2-methoxy-5-(2-ethylhexyloxy)-1,4-phenylenevinylene]

This Chapter is focused on the preparation and characterization of hybrid materials consisting of Au NPs and poly[2-methoxy-5-(2-ethylhexyloxy)-1,4-phenylenevinylene] (MEH-PPV). The composites were prepared using similar procedures as the composites with P3OT (Chapter 4.3.). Briefly, simple mixing of Au nanoparticle organosol with the polymer solution of various concentrations was used for obtaining composites type **M** while composites type **R** were prepared by an *in situ* reduction of metal ions in the presence of the polymer solutions of various concentrations. The optical and morphological properties of both types of hybrid materials will be compared and advantages/disadvantages of the preparative methods will be shown and discussed in this chapter. Finally, the properties of these composites will be compared with those obtained for P3OT.

4.4.1. Morphologies of Au nanoparticles in organosol and composites with MEH-PPV

4.4.1.1. Parent Au organosol

Since dichloromethane (DCM) is a commonly used solvent for alkoxy-substituted PPVs, contrary to P3OT composites, Au NPs had to be prepared in DCM. TEM image and corresponding nanoparticles size distribution of the parent Au organosol in DCM is shown in Figure 4.4-1. It contains small, mostly isolated Au NPs with the average size of 4 nm. Compared to TOAB-stabilized Au organosol in toluene, the particles in DCM are smaller than those prepared in toluene ($d = (5.6 \pm 1.4)$ nm).

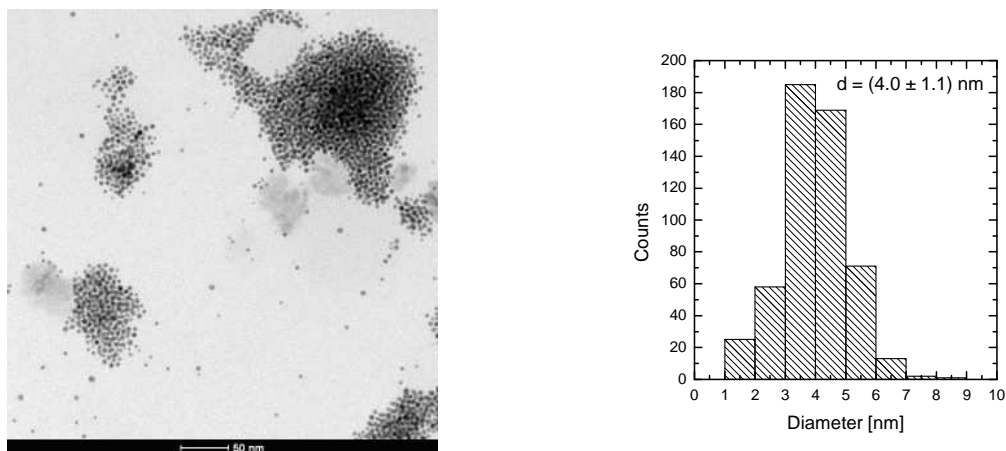


Figure 4.4-1. TEM image and nanoparticles size distribution of the parent Au organosol in DCM.

4.4.1.2. Nanocomposites type M

Representative TEM images and nanoparticle size distribution diagrams (Figure 4.4-2) clearly show that the morphology of Au NPs in nanocomposites **M** markedly depends on the polymer concentration. Well-separated small Au NPs of the mean size ($d = (4 \pm 1)$ nm) are observed in the nanocomposite **M₁** (higher polymer concentration, Figure 4.4-2b), having the size distribution practically identical with that of the parent Au organosol (Figure 4.4-1). On the other hand, large Au NPs and small compact aggregates consisting of several NPs with the overall mean size ($d = (10.2 \pm 5.3)$ nm) and a broad size distribution are observed in the nanocomposite **M₇** (Figure 4.4-2a), in which the polymer concentration is seven times lower than that in **M₁**. This observation suggests that polymer molecules take part in the stabilization of Au NPs after the removal of the original stabilizer (TOAB) from the system during the precipitation and purification of the nanocomposite. The preformed small Au NPs are well dispersed in the polymer-rich system **M₁** but poorly stabilized in the polymer-poor system **M₇**, in which they undergo subsequent assembling to aggregates or they even fuse to larger NPs. This means that the morphology of Au NPs in a **M**-type nanocomposite is strongly affected by the polymer/Au-NPs ratio.

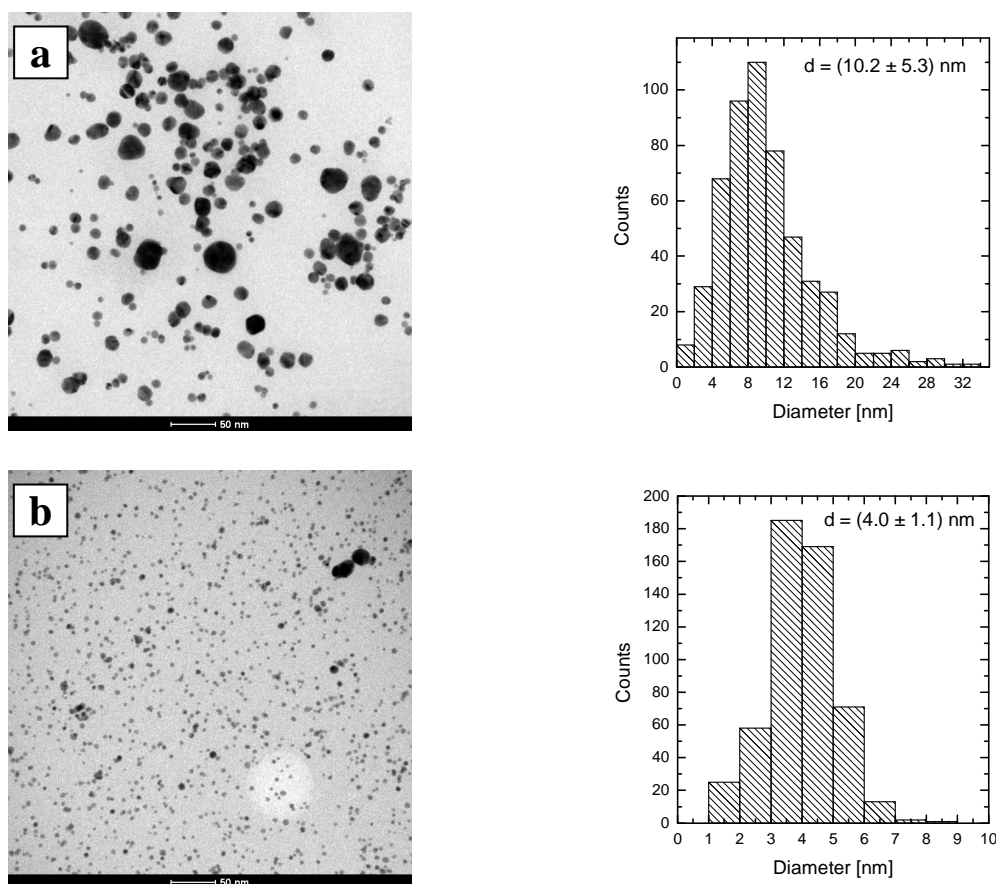


Figure 4.4-2. TEM images and nanoparticles size distributions of Au NPs for nanocomposites (a) **M₇** and (b) **M₁** with the Au/MEH-PPV ratio 7/1 and 1/1, respectively.

4.4.1.3. Nanocomposites type R

Figure 4.4-3 shows TEM images of nanocomposites **R**₁ to **R**₇ with various Au/polymer ratio, and nanoparticles size distribution diagrams of isolated particles in nanocomposites **R**₇ and **R**_{2,3}, for which corresponding nanoparticles size distributions could be determined. TEM images indicate entirely different dependence of the nanoparticle morphology on the polymer concentration, almost opposite to that one observed in the nanocomposites **M**. In the composite **R**₇ containing the lowest polymer concentration, a large fraction of small isolated NPs (mean size \approx 5 nm) accompanied by an occurrence of smaller aggregates of several nanoparticles and a small fraction of large, nearly macroscopic aggregates were observed (Figure 4.4-3a). One of the large aggregates is shown in SEM image of Figure 4.4-4a where it is seen that the aggregate is formed by a fusion of large spherical particles. In the composite **R**_{2,3}, a fraction of large aggregates has a higher abundance compared to the composite **R**₇. Nanoparticle size distribution of isolated particles in the composite **R**₇ differs from that in the composite **R**_{2,3}. While the composite **R**₇ contains isolated particles with the mean size about 5 nm, composite **R**_{2,3} consists of isolated particles with the size of 9 nm. Thus it seems that initially the aggregation of small (5 nm) particles occurs followed by aggregation of larger particles. With increasing polymer concentration (composites **R**_{1,4} and **R**₁), the small NPs that had been observed at low polymer concentrations almost disappeared and complex, irregular and branched aggregates were formed. At the highest polymer concentration (**R**₁), small Au NPs are practically absent having been transformed into aggregates (Figure 4.4-3d). Compared with the aggregates found in composites at the low polymer concentration (composite **R**₇), the aggregates at the high polymer concentration are smaller in size (Figure 4.4-4b).

As a result, a question arises whether the observed objects have been formed by polymer-induced Au nanoparticle aggregation, or by Au NPs fusion. An ultrasound-induced disintegration of Au nanoparticle aggregates embedded in poly[3,4-(ethylenedioxy)thiophene-2,5-diyl] into individual NPs has been observed by Li et al.⁷⁴. They concluded that π - π interactions between polymer chains attached to the Au NPs are the main force stabilizing their aggregates. Therefore, we exposed a DCM solution of **R**₁ to ultrasound of a similar frequency (at 40 kHz) for various times up to 45 min. However, any disintegration of nanoparticle aggregates into smaller ones was not observed. This suggests that the Au nanoparticle aggregates observed in TEM and SEM images of composites **R** are large compact aggregates formed by fusion of Au NPs rather than Au NP aggregates linked by the polymer chains.

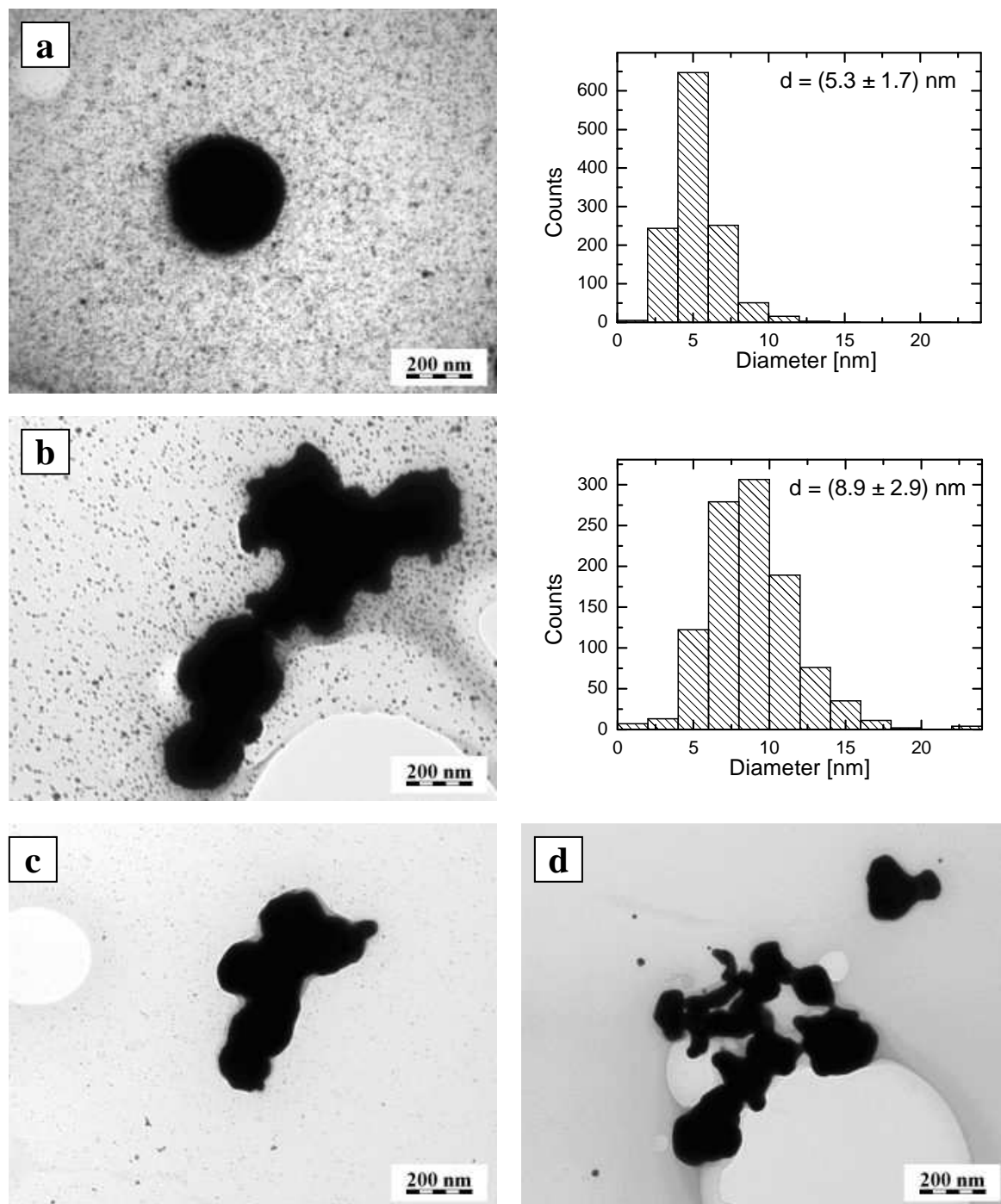


Figure 4.4-3. TEM images of Au NPs and NP aggregates for composites R_7 (a), $R_{2.3}$ (b), $R_{1.4}$ (c) and R_1 (d) with the Au/MEH-PPV ratio 7/1, 2.3/1, 1.4/1 and 1/1, respectively, and corresponding nanoparticles size distributions for the samples in which isolated nanoparticles could be distinguished.

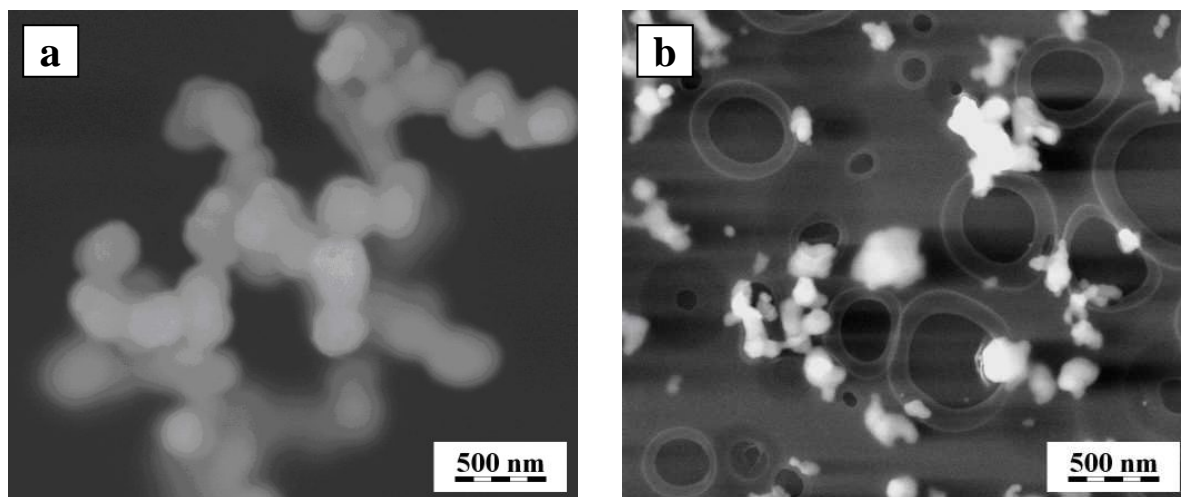


Figure 4.4-4. SEM images of Au NP aggregates for composites **R₇** (a) and **R₁** (b) with the Au/MEH-PPV ratio 7/1 and 1/1, respectively.

4.4.2. UV-Vis spectra of Au/MEH-PPV nanocomposites

Important information about the actual state of the polymer and of the Au nanoparticle assembly in the nanocomposites has been obtained from the comparison of the UV-Vis optical spectra of the nanocomposites and their constituents (Figure 4.4-5). The main-chain $\pi \rightarrow \pi^*$ absorption band of MEH-PPV (Figure 4.4-5, black lines) occurs at 500 nm. The SPE band of the parent Au organosol is observed at 520 nm (Figure 4.4-5, inset) which indicates the presence of small isolated Au NPs, in agreement with the TEM images (Figure 4.4-1).

The spectra of nanocomposites **M** (Figure 4.4-5a, **M₇** red line; **M₁** green line) resemble that of the neat MEH-PPV. They only differ in an increased extinction in the red spectral region outside the MEH-PPV $\pi \rightarrow \pi^*$ absorption band. The optical absorption at longer wavelength increases with the increasing Au content. No distinct shoulders at 520 nm attributable to the SPE band of small Au NPs are observed in the spectra of both nanocomposites **M₇** and **M₁**. Only a slight broadening and a barely detectable red-shift of the MEH-PPV $\pi \rightarrow \pi^*$ transition band maximum (from 500 to 502 nm) is observed for **M₇**. The longer-wavelength extinction up to the NIR region can be ascribed to the presence of larger Au NPs and assemblies of Au NPs, for which a red shift of the SPE has been observed experimentally as well as predicted by calculations^{179, 180}. The volume fraction of Au in **M₁** is only ca. 5 %, and hence the SPE band of Au NPs has low intensity compared with the strong MEH-PPV $\pi \rightarrow \pi^*$ transition band.

The UV-Vis spectra of nanocomposites **R** (prepared by an *in situ* reduction of AuCl_4^- salt in the polymer solution, Figure 4.4-5b) also show an increased extinction in the wavelength regions typical of the presence of large Au NPs and/or NP aggregates. While the

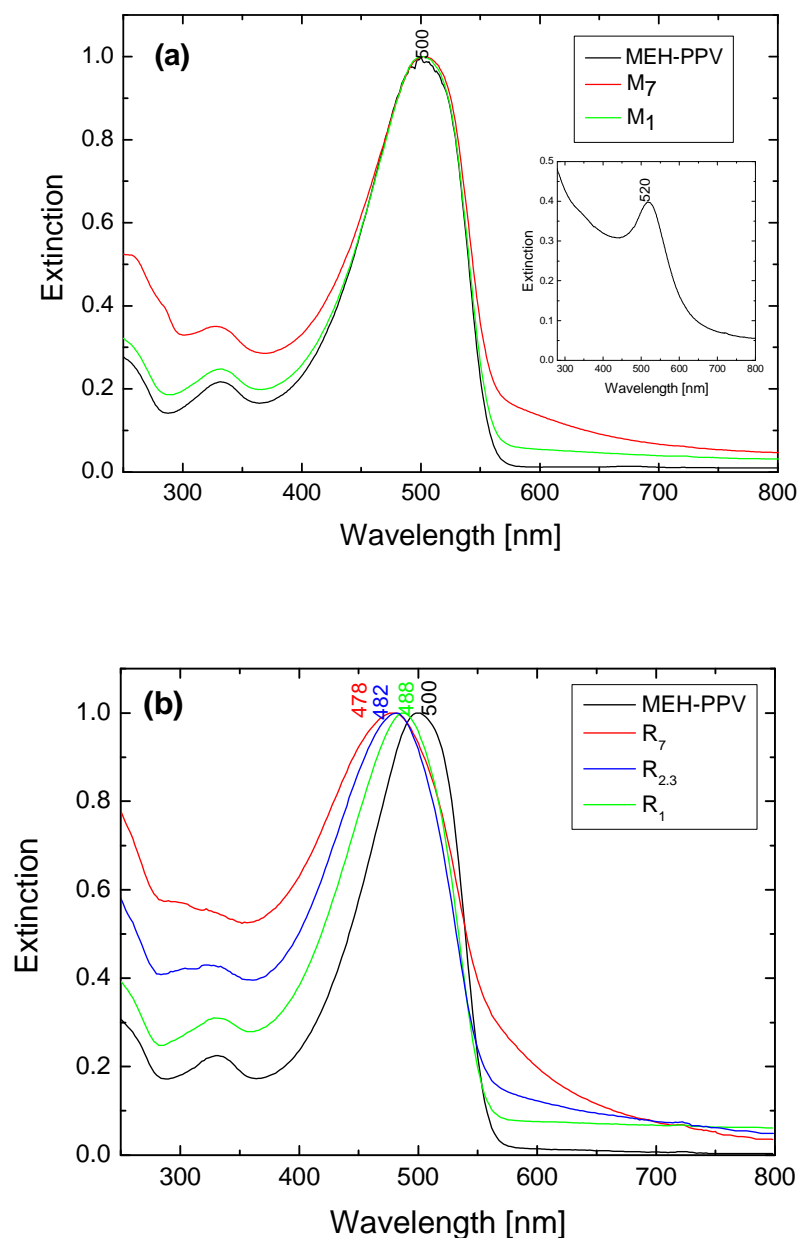


Figure 4.4-5. Extinction spectra of (a) composites M_7 (red line) and M_1 (green line) with the Au/MEH-PPV ratio 7/1 and 1/1, respectively; (b) composites R_7 (red line), $R_{2.3}$ (blue line) and R_1 (green line) having Au/MEH-PPV ratio 7/1, 2.3/1 and 1/1, respectively. Extinction spectrum of Au organosol (inset of Fig 4.4-5a) is shown for a comparison. The spectra were normalized on their absorption maxima.

extinction of the composite R_7 above 550 nm gradually decreases (Figure 4.4-5b, red line), only a constant elevated extinction background is observed for composite R_1 (Figure 4.4-5b, green line). For the composite R_7 , the extinction between 550 – 700 nm could correspond to the smaller aggregates of several Au NPs which were observed in the TEM image (Figure 4.4-3a). Their number is much smaller than the fraction of small isolated Au NPs and thus they were not included in the size distribution. The extinction above 700 nm for the

polymer poor composite (**R**₇) can be ascribed to the large macroscopic aggregates which are also present in the composite sample. For the composite **R**₁, the elevated extinction background above 550 nm could correspond to the aggregates as well as to large, nearly macroscopic compact aggregates which gradually approach the extinction characteristics of bulk gold. Such aggregates were found in the TEM images (Figure 4.4-3d). Moreover, the spectra of the composites exhibit a pronounced blue shift of the $\pi \rightarrow \pi^*$ absorption band maximum compared with its position in the neat polymer (500 nm): the maximum occurs at 478 nm for nanocomposite **R**₇ (Figure 4.4-5b, red line), at 480 nm for **R**_{2,3} (Figure 4.4-5b, blue line) and **R**_{1,4}, and at 488 nm for **R**₁ (Figure 4.4-5b, green line). Such blue shift indicates shortening of the extent of the π -electron delocalization in π -conjugated macromolecules¹⁸¹. It means that MEH-PPV undergoes molecular structure changes during the preparation of the nanocomposites **R**.

4.4.3. Stability of MEH-PPV in reference systems

An important question has arisen whether the observed shortening of the conjugation length of the polymer in composites type **R** actually occurs prior to the addition of the reductant, i.e. by interaction of the polymer with the AuCl₄⁻/TOAB complex, or, alternatively, during the subsequent reduction step. To elucidate this point, time evolutions of the UV-Vis spectra of reference systems containing (i) the reducing agent (NaBH₄) and the polymer and (ii) the AuCl₄⁻/TOAB complex and the polymer have been recorded.

4.4.3.1. Stability of MEH-PPV after addition of NaBH₄

Addition of an aqueous solution of NaBH₄ to a DCM solution of MEH-PPV both with and without the phase transfer reagent (TOAB) did not cause any change of the UV-Vis spectrum of the polymer as well as of the molecular weight of the polymer (as obtained by size-exclusion chromatography measurements) even after 24 h treatment in the dark upon vigorous stirring.

4.4.3.2. UV-Vis spectral study of reaction of MEH-PPV with the AuCl₄⁻/TOAB complex

The AuCl₄⁻/TOAB complex reacts with the polymer quite fast. Figure 4.4-6a shows the time evolution of UV-Vis spectra of reference system containing the AuCl₄⁻/TOAB complex and the polymer with the Au/MEH-PPV ratio 2.3/1 together with spectra of the neat

polymer and the $\text{AuCl}_4^-/\text{TOAB}$ complex. The $\text{AuCl}_4^-/\text{TOAB}$ complex itself has a strong absorption band at 366 nm due to a metal-to-ligand charge-transfer transition. After addition of the polymer having its optical absorption maximum at 500 nm, the absorption band is shifted to 494 nm. The spectrum is close to a simple superposition of the spectra of the polymer and of the complex. With increasing time after the mixing, the absorption band of the polymer shows significant band broadening, considerable loss in the absorbance and a pronounced blue shift of the main absorption band, the maximum reaching 381 nm after a 24 h exposure of the polymer to $\text{AuCl}_4^-/\text{TOAB}$ complex. The observed blue shifts are thus compatible with those detected in the UV-Vis absorption spectra of the composites **R**.

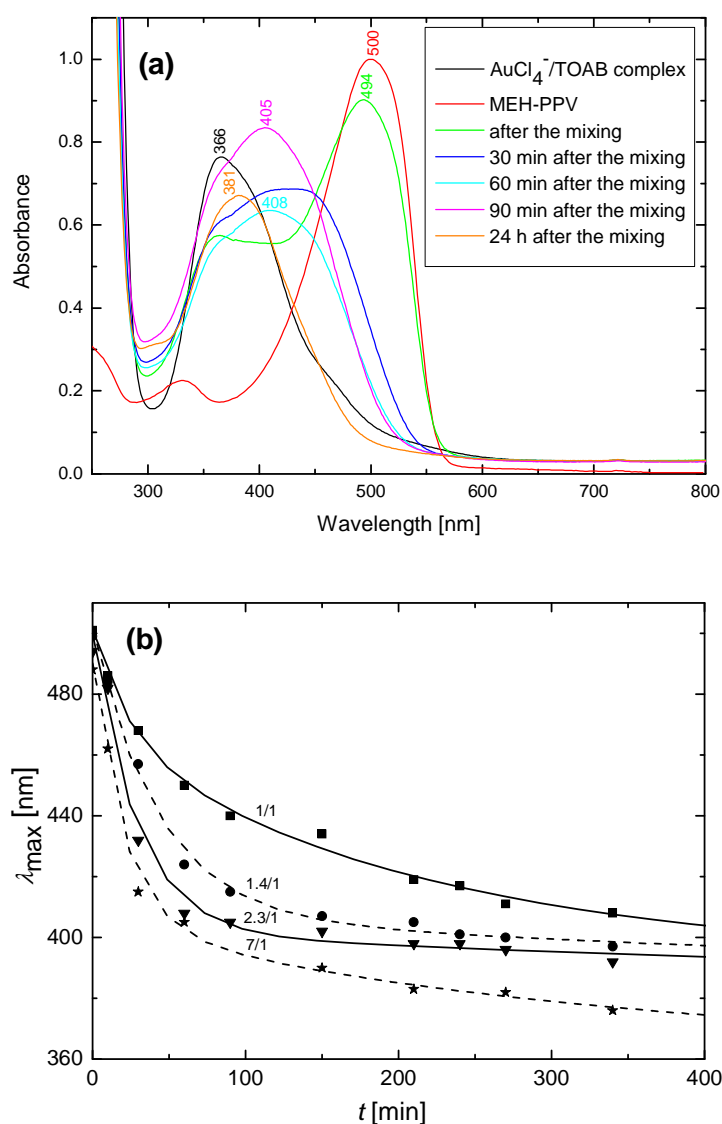


Figure 4.4-6. (a) Time-evolution of UV-Vis spectra of the reference reaction system containing the $\text{AuCl}_4^-/\text{TOAB}$ complex (black line) and the polymer (red line) after the mixing. (b) Time dependence of the position of the MeH-PPV absorption band maximum, λ_{max} , during the reaction. The weight ratios of Au^{3+} ions and MEH-PPV were from 7/1 to 1/1.

Progressive blue shifts of UV-Vis absorption maximum of the polymer were observed for all reference systems differing in the Au/MEH-PPV ratio, as shown in Figure 4.4-6b. The higher is the concentration of AuCl_4^- with respect to the polymer concentration the faster and the more progressive is the blue shift, i.e. the decrease in the extent of the polymer chain conjugation. Therefore, in our case, the most significant changes occur for the reference system with Au/MEH-PPV ratio 7/1. It is thus evident that the presence of the $\text{AuCl}_4^-/\text{TOAB}$ complex in the polymer solution affects the conjugation length of the polymer in both the reference systems as well as in the composites type **R**, and this effect is both time- and polymer concentration-dependent.

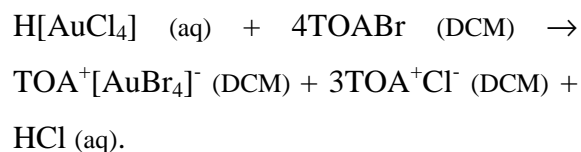
It should be noted that no similar perturbation of the conjugation length of polymer chains by the $\text{AuCl}_4^-/\text{TOAB}$ complex has been observed in the case of polythiophenes^{71, 182}. Zhai et al.⁷¹ reported that an excess of TOAB prevents poly(3-hexylthiophene)s from oxidation in the $\text{AuCl}_4^-/\text{TOAB}$ environment. However, we have found that a fivefold stoichiometric excess of TOAB does not prevent MEH-PPV chains from the damage. Therefore, we examined the redox activity of the $\text{AuCl}_4^-/\text{TOAB}$ complex towards MEH-PPV by cyclic voltammetry.

4.4.3.3. Cyclic voltammetry

Cyclic voltammogram (CV) of the $\text{AuCl}_4^-/\text{TOAB}$ complex in 0.1 M tetrabutylammonium perchlorate solution (TBAPC) in DCM as a supporting electrolyte is depicted in Figure 4.4-7a. Two oxidation peaks with the onsets at about 0.6 V and 1 V, respectively, were observed. In the reversed direction, the reduction peak with the onset at about 0.2 V appeared. To be able to assign these peaks to the redox processes which occur during the preparation, we also examined CVs of (i) $\text{AuCl}_4^-/\text{TBAPC}$ complex and (ii) $\text{AuCl}_4^-/\text{TOAB}$ complex with addition of five times higher amount of TOAB compared to that in the complex used for composite type **R** preparation (see Chapter 3.3. for sample preparation). The CVs are shown in Figure 4.4-7b and c. For $\text{AuCl}_4^-/\text{TBAPC}$ complex, only one oxidation peak with the onset at about 1 V was observed. Thus, this peak could be assigned to the oxidation of Cl^- anions originating from Au salt (HAuCl_4) and bound in complex with TBAPC. Formation of $\text{AuCl}_4^-/\text{TBAPC}$ complex can be depicted by the following reaction:



The voltammogram of the system with five times higher excess of TOAB (Figure 4.4-7c) is similar to that one in Figure 4.4-7a but the peak with the onset at about 0.6 V is more significant than the band with the onset at 1 V assigned to the oxidation of Cl^- anions. Since the peak at 0.6 V scales with the TOAB content, it can be assigned to the oxidation of Br^- anions. These ions can originate from the “free” TOAB which is not in the complex with Au(III) and/or from Br^- ions “bound” in complex with Au(III) ($[\text{AuBr}_4]^-$). The exchange reaction of Cl^- for Br^- in complex with Au(III) was early described¹⁸³:



The reduction peak with the onset at 0.2 V (Figure 4.4-7a) could originate in the reduction of Au(III) to Au(0) in complex with the phase transfer reagent. The value of redox potential of the $\text{AuCl}_4^-/\text{TOAB}$ complex is substantially lower compared with the standard potentials of $[\text{AuCl}_4]^-$ or $[\text{AuBr}_4]^-$ (if we consider the exchange of halogen ions) complex ions in aqueous solution. The values of redox potentials corresponding to the reduction of $[\text{AuCl}_4]^-$ and $[\text{AuBr}_4]^-$ complex ions are 0.68 V and 0.61 V vs. SCE (ref.), respectively. This shift of redox potential of $\text{AuCl}_4^-/\text{TOAB}$ complex compared to those of $[\text{AuCl}_4]^-$ or $[\text{AuBr}_4]^-$ complex ions could be assigned to the presence of

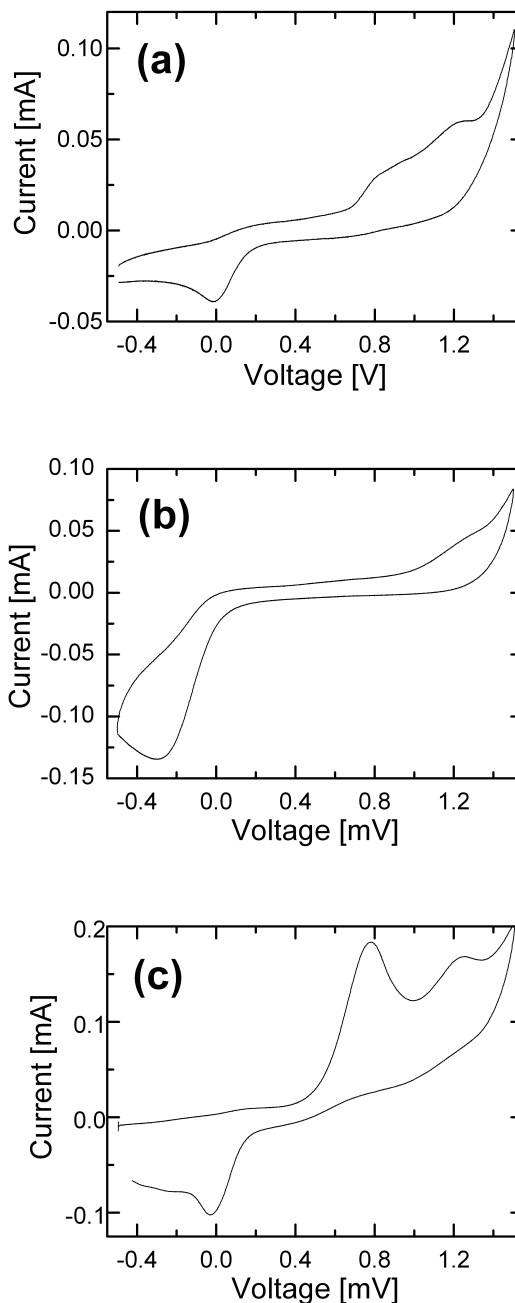


Figure 4.4-7. Cyclic voltammograms of (a) $\text{AuCl}_4^-/\text{TOAB}$ complex, (b) $\text{AuCl}_4^-/\text{TBAPC}$ complex and (c) $\text{AuCl}_4^-/\text{TOAB}$ complex with five times higher excess of TOAB. All the measurements were performed in TBAPC/DCM supporting electrolyte.

tetraoctylammonium cation. Since the respective oxidation peak is less pronounced, the process is considered to be poorly reversible.

CVs of the MEH-PPV solution in DCM and P3OT film in acetonitrile were also measured (Figure 4.4-8). Both polymers show broad oxidation as well as reduction peaks. Nevertheless, the onset of oxidation peak of MEH-PPV (0.15 V, Figure 4.4-8a) is lower than that of P3OT (0.4 V, Figure 4.4-8b) and similar to the onset of reduction of Au^{3+} . Therefore, MEH-PPV can be oxidized by the $\text{AuCl}_4^-/\text{TOAB}$ complex whereas P3OT shows the stability against oxidation by the $\text{AuCl}_4^-/\text{TOAB}$ complex.

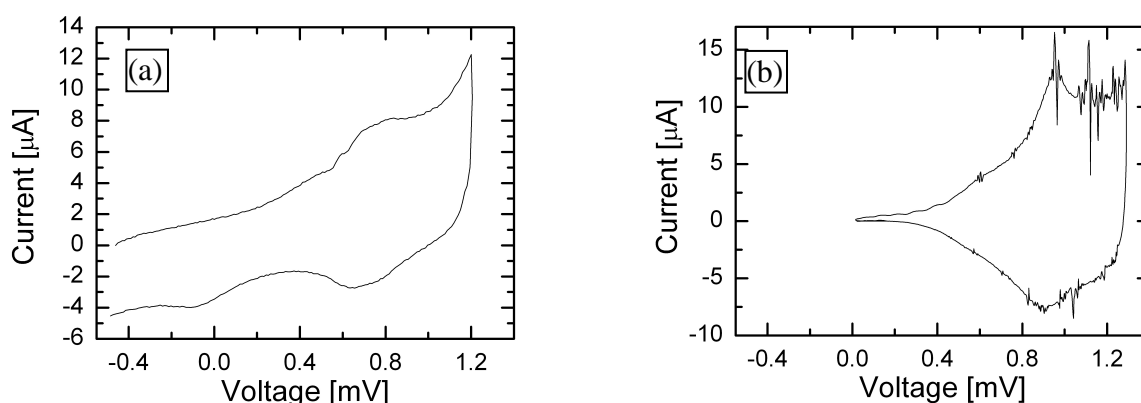


Figure 4.4-8. Cyclic voltamograms of (a) MEH-PPV solution in DCM, (b) P3OT film in acetonitrile.

4.4.3.4. Relation between molecular weight and UV-Vis spectra of MEH-PPV during reaction with the $\text{AuCl}_4^-/\text{TOAB}$ complex.

The measurement of molecular weights (MWs) of MEH-PPV in reference system during exposure to $\text{TOAB}/\text{AuCl}_4^-$ complex has shown that the observed blue-shifts in UV-Vis spectra (Figure 4.4-6) result in the lowering of molecular weight. In particular, the MW of MEH-PPV in reference system decreased from 450 000 for the pristine polymer to 319 000 after 90 min exposure to $\text{AuCl}_4^-/\text{TOAB}$ complex. 24 h exposure of the polymer to $\text{AuCl}_4^-/\text{TOAB}$ complex caused the decrease of molecular weight to 186 000. The original deep orange-red color of the pristine polymer turned to yellow after the treatment. It indicates that the $\text{AuCl}_4^-/\text{TOAB}$ complex treatment resulted into a disruption of the π -electron system accompanied by a significant decrease of molecular weight. MWs of the polymer after the exposure of MEH-PPV to the $\text{AuCl}_4^-/\text{TOAB}$ complex for 1 min and 30 min could not be determined because of the insolubility after precipitation.

The observed decrease in the polymer molecular weight caused by its interaction with the $\text{AuCl}_4^-/\text{TOAB}$ complex is relatively low and does not explain the observed decrease in the

extent of π -conjugation (blue shifts in UV-Vis spectra). To elucidate the nature of the blue shift in the UV-Vis spectra of the polymer in composite samples, optical spectra of various fractions of the polymer were taken using SEC equipped with DAD detection. No blue shift of the absorption band for the fractions with MW above 30 000 was observed and a maximal blue shift ca. 10 - 15 nm was detected only for low-MW fractions ($\sim 10^3$), which is only 1/10 of the spectral shift observed for the reference system after 24 h exposure to $\text{AuCl}_4^-/\text{TOAB}$ complex. This is in agreement with the published spectroscopic studies on PPV oligomers that showed that the dependence of the position of the π - π^* optical absorption peak on the conjugated chain length tends to saturate already for short oligomers as hexamers¹⁸⁴. Furthermore, we have examined a possible effect of the polymer oxidation with air oxygen using the approach employed earlier for the investigation of the stability of substituted polyacetylenes¹⁸⁵⁻¹⁸⁷: a dilute THF solution of MEH-PPV was exposed to air in daylight and the solution was periodically analyzed by SEC-DAD for one month. A partial oxidation of MEH-PPV achieved after one month was found to cause an additional blue shift of ca. 10 nm only. If we consider the synergy of both effects, the sum of both shifts would be 20 - 25 nm, which is fairly below the shift caused by the decrease in the effective conjugation length of the polymer caused by the $\text{AuCl}_4^-/\text{TOAB}$ complex after 24 h treatment. Therefore, a better insight into the nature of the changes which have occurred in the polymer during the composite type **R** preparation had to be obtained through the employment of vibrational spectroscopy.

4.4.4. Molecular spectra of MEH-PPV and its composites

4.4.4.1. FT-IR spectra

FT-IR spectra of neat MEH-PPV, MEH-PPV after the treatment with $\text{AuCl}_4^-/\text{TOAB}$ complex and of the composites **R**₁ and **R**₇ are compared in Figure 4.4-9. IR spectra of composites **M** are not shown since they were found to be identical with that of neat MEH-PPV. All IR-active bands characteristic of MEH-PPV, as reported by Scott et al.¹⁸⁸, are clearly seen in the spectra of all samples. After the treatment with $\text{AuCl}_4^-/\text{TOAB}$ complex, the changes are mainly observed in the regions 850 - 970 cm^{-1} and 1240 - 1350 cm^{-1} . Namely, the peak intensity at 966 cm^{-1} (vinylene -C-H out-of-plane bending) decreased, the peak at 854 cm^{-1} (aromatic C-H out of plane bending vibrations) shifted towards higher wavenumbers by 12 cm^{-1} , the peaks at 1252 cm^{-1} and 1350 cm^{-1} shifted towards lower wavenumbers by 14 cm^{-1} and 8 cm^{-1} , respectively, and new peaks at 1096, 1608 and 1732 cm^{-1} appeared.

Similar spectral changes are observed for composites \mathbf{R}_1 and \mathbf{R}_7 , only with smaller extent due to the shorter time period for which the polymer has been exposed to $\text{AuCl}_4^-/\text{TOAB}$ complex prior to reduction. During the preparation of composites type \mathbf{R} , the exposure time was much shorter (10 min) compared to 24 h for the reaction of MEH-PPV with $\text{AuCl}_4^-/\text{TOAB}$ complex shown in the discussion of FT-IR spectra.

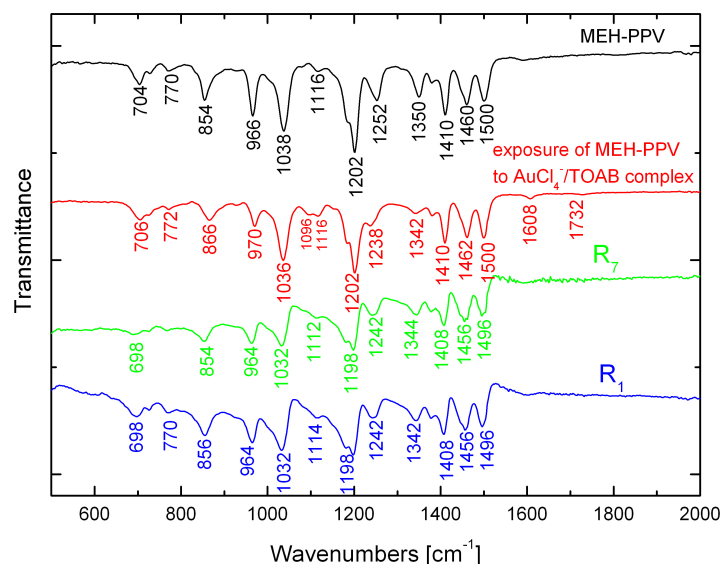


Figure 4.4-9. FT-IR spectra of neat MEH-PPV, MEH-PPV after 24 h treatment with $\text{AuCl}_4^-/\text{TOAB}$ complex and MEH-PPV in composites \mathbf{R}_7 and \mathbf{R}_1 with the Au/MEH-PPV ratio 7/1 and 1/1, respectively. Measured from powders.

One of the possible reactions that could occur in MEH-PPV upon the addition of the $\text{AuCl}_4^-/\text{TOAB}$ complex is the chlorination of the vinylene double bond. In such case, the change in the characteristic stretching vibration of C-Cl groups observed around 770 cm^{-1} should accompany the changes assigned to the deformation modes of phenyl ring. Although the C-Cl vibration, which probably originates from the polymer precursor used in the synthesis¹⁸⁹, is observed in the spectrum of neat polymer, its intensity remains unchanged. Hence, the observed changes in IR spectra do not provide a decisive evidence for the proposed chlorination of polymer chains.

Better explanation of the IR spectral changes caused by the reaction of π -conjugated polymer with AuCl_4^- would be the formation of the addition charge-transfer complex involving the polymer vinylene double-bond. Such mechanism can explain the pronounced decrease in the effective conjugation length observed in the UV-Vis spectra while simultaneously only a small decrease in molecular weight was detected. Furthermore, an

oxidative degradation also takes place via a well-known mechanism through the formation of peroxidic dioxyethan groups that, in the next step, can partially result in a chain scission forming carbonyl or aldehyde end-groups. In particular, evidence of such process is provided by the presence of weak 1608 cm^{-1} and 1732 cm^{-1} bands in the FT-IR spectrum of MEH-PPV treated by the $\text{AuCl}_4^-/\text{TOAB}$ complex (Figure 4.4-9). In accord with ref.¹⁹⁰ the 1608 cm^{-1} band is attributed to the asymmetric phenyl semicircular stretch due to the formation of carbonyls and the 1732 cm^{-1} band to carbonyl stretch of an ester or carboxylic acid.

4.4.4.2. Raman and fluorescence spectra

Raman spectra of neat MEH-PPV, MEH-PPV treated by the $\text{AuCl}_4^-/\text{TOAB}$ complex and of nanocomposites **R₁** and **R₇** (Figure 4.4-10) were recorded using the 632.8 nm excitation wavelength. Employment of this wavelength enabled to compare band intensities of the studied samples without any interference of resonance effects. All spectra show the bands characteristic of para(phenylene vinylene), PPV, as reported e.g. by Lefrant et al.^{191, 192} (see Table 4.4-1). The spectra of nanocomposites **M** are not shown in Figure 4.4-10 since they are identical with that of MEH-PPV showing neither band shifts nor changes in relative intensities of the bands.

$\nu\text{ [cm}^{-1}\text{]}^a$	$\nu\text{ [cm}^{-1}\text{]}^b$	Assignment
1174	1110	C-C stretching + C-H bending of the phenyl ring
1330	1308	C=C stretching + C-H bending of the vinyl group
1550	1550	C=C stretching of the phenyl ring
1586	1582	C-C stretching of the phenyl ring
1625	1622	C=C stretching of the vinyl group

Table 4.4-1. Wavenumbers (cm^{-1}) and assignment of the most intense Raman modes of PPV.

^a obtained for para(phenylene vinylene) from the work of Lefrant et al.¹⁹²

^b obtained for MEH-PPV from this study

Raman spectrum of the polymer after the treatment with the $\text{AuCl}_4^-/\text{TOAB}$ complex (Figure 4.4-10, red spectrum) shows a significant shift of the triplet to higher wavenumbers, in particular the most intense band of the triplet found at 1597 cm^{-1} is shifted by 15 cm^{-1} compared with the neat polymer. According to the previously reported studies^{191, 192}, the changes in the dominant triplet can be related to the changes in conjugation length of MEH-PPV: when the conjugation length is reduced, the band at 1622 cm^{-1} increases in intensity with respect to that at 1550 cm^{-1} , and both bands are shifted to higher wavenumbers

with the decreasing length of the effective conjugation. It was reported that the shift of the most intense band of the triplet for an oligomer containing one phenyl ring is 11 cm^{-1} compared to the position of this band in the spectrum of neat polymer¹⁹³. Thus, the observed shifts of triplet bands in the spectrum of the polymer after exposure to the $\text{AuCl}_4^-/\text{TOAB}$ complex can be related to a decrease in conjugation length of the polymer.

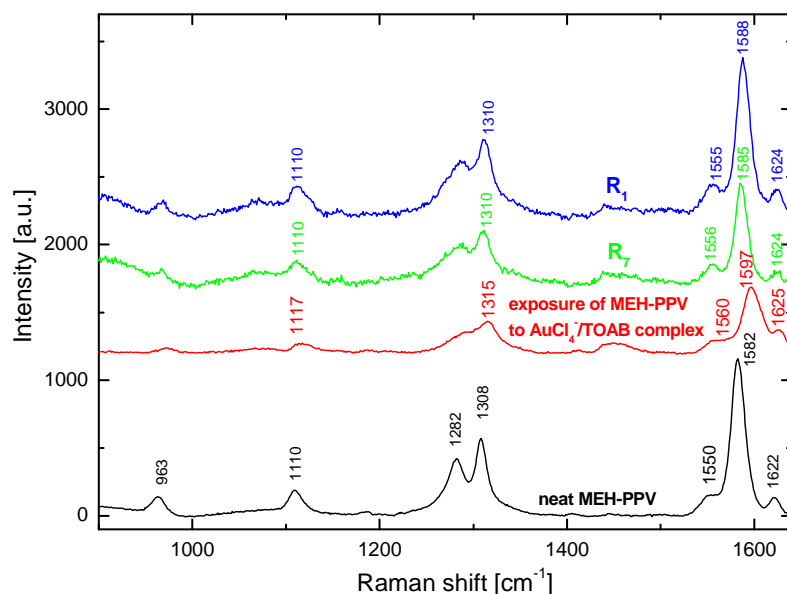


Figure 4.4-10. Raman spectra of neat MEH-PPV (black line), MEH-PPV after 24 h exposure to $\text{AuCl}_4^-/\text{TOAB}$ complex (red line) and composites \mathbf{R}_7 (green line) and \mathbf{R}_1 (blue line) with the Au/MEH-PPV ratio 7/1 and 1/1, respectively.

Similarly to the spectrum of the polymer after the treatment with the $\text{AuCl}_4^-/\text{TOAB}$ complex, the triplet bands of nanocomposites \mathbf{R} are also shifted to higher wavenumbers; however, the shifts are less pronounced ($1550\text{ (MEH-PPV)} \rightarrow 1556\text{ (}\mathbf{R}_7\text{)} \rightarrow 1555\text{ cm}^{-1}\text{ (}\mathbf{R}_1\text{)}$; $1582\text{ (MEH-PPV)} \rightarrow 1585\text{ (}\mathbf{R}_7\text{)} \rightarrow 1588\text{ cm}^{-1}\text{ (}\mathbf{R}_1\text{)}$; $1622\text{ (MEH-PPV)} \rightarrow 1624\text{ (}\mathbf{R}_7\text{)} \rightarrow 1624\text{ cm}^{-1}\text{ (}\mathbf{R}_1\text{)}$). Several factors have to be taken into consideration for the explanation of the observed changes in Raman spectra of nanocomposites \mathbf{R} since, besides the chemical changes introduced during the NP preparation, the spectra might be affected by the presence of Au NPs or NPs aggregates. The shortening of the conjugation length which has been detected also by UV-Vis spectroscopy (in chapter 4.4.2.) could lead to the observed shifts of Raman bands. Moreover, the interaction of Au NPs or NP aggregates with the polymer chains could also cause the shifts of the bands characteristic for conjugated system. Finally, the changes in the packing of the polymer chains can be also taken into account for the explanation of the observed shift. For example, Sáfar et al.¹⁹⁴ described a similar shift of the main triplet band in

freeze- and heat-dried samples of MEH-PPV/SiO₂ core/shell nanocomposites. This shift was assigned to denser packing conditions inside the nanostructured silica shells which induce a higher interchain interaction via aggregate sites.

The photoluminescence measurement could provide better information about the chain packing since the emission spectrum of polymer aggregates is expected to be red shifted. Therefore, we have measured fluorescence spectra of composite samples **R**₁ and **R**₇ and we have compared them with the spectrum of the neat polymer. However, we had observed just opposite: small blue shifts in the emission spectra (excitation at 500 nm) for the composite samples were detected. It appears that the observed changes in Raman spectra actually reflect the shortening of the effective conjugation length of the polymer during the composite preparation. A meaningful comparison of the neat polymer emission spectra with those of the composites with respect to the polymer chain packing effects is thus biased by the (far stronger) effect of the polymer degradation in the composite. Therefore, it is difficult to evaluate the chain packing effects in composite samples from the interpretation of the Raman and fluorescence spectra.

It can be concluded from the molecular spectroscopic study that the AuCl₄⁻/TOAB complex causes molecular structure changes of MEH-PPV resulting in lowering the extent of conjugation in polymer chains. As far as the preparation pathway to nanocomposites **R** is concerned, these changes take place mainly at the initial stage of the preparation until the reducing agent is added to the reaction mixture. Therefore, to avoid polymer degradation in composite type **R** preparation, it is necessary to add reductant as soon as possible in order to minimize the time for which the polymer is in contact with the AuCl₄⁻/TOAB complex.

4.4.5. Size-exclusion chromatography (SEC) analyses of dissolved Au/MEH-PPV nanocomposites

To obtain information on the intensity of interactions between Au NPs and polymer chains and eventual changes in the molecular weight and in the extent of conjugation of polymer chains we carried out SEC analyses of the dissolved composites using an instrument equipped with a diode-array UV-Vis detector.

The SEC records of composites **M**₇ (with a low polymer content) and **M**₁ (with a high polymer content) are shown in Figure 4.4-11. The analyses have revealed a separation of the nanocomposites **M** on SEC columns into two fractions. The first fractions were eluted (retention time ca 17 min) before the upper exclusion limit of used columns (MW ≈ 2 × 10⁶)

while the second fractions were eluted at longer retention time of about 29 min. UV-Vis spectra of these two fractions differ as shown in Figure 4.4-12. UV-Vis spectrum of the fraction at shorter retention time for composite **M**₇ (Figure 4.4-12a) resembles the spectrum of the unfractionalized Au organosol while for composite **M**₁ (Figure 4.4-12c) the spectrum is almost identical with that of the composite **M**₇ (Figure 4.4-5a, red line). UV-Vis spectra of fractions at longer retention time for both composites **M** (Figure 4.4-12b,d) are similar and resemble the spectrum of the neat polymer. Therefore, we can conclude that the first fractions contain mixed assemblies of Au NPs while the second fractions contain practically intact MeH-PPV macromolecules.

It should be mentioned here that relative contents of the Au-rich (shorter retention time) and neat polymer (longer retention time) fractions depend on the time for which the nanocomposite is in contact with THF. If the nanocomposite was injected to SEC system from DCM solution, relative content of the first fraction was high, up to 25 %, and its UV-Vis spectrum showed higher content of MeH-PPV. If the DCM solution was diluted with five times excess of THF and allowed to stay for some time, relative content of the Au rich first fraction was lower and its spectrum showed decreased content of the polymer and increased relative content of Au nanoparticles. When the nanocomposites were dried, then redissolved in THF and injected from this solution, the first fraction included practically only Au nanoparticles. This behavior can be explained by better solubility of MEH-PPV in THF than in DCM.

Surprisingly, the SEC measured molecular weights of the composites **M** are lower than that for neat MEH-PPV. For nanocomposite **M**₇, more pronounced decrease in MW of the second fraction from 390 000 to 220 000 was observed in contrast with a decrease to 365 000 only for nanocomposite **M**₁. The observed small decrease in MW of the free polymer fraction compared to the parent polymer can be explained as a result of partial fractionation of polymer due to formation of joint assemblies with Au NPs: longer chains are more strongly anchored in the assemblies. Composite with higher Au content (**M**₇) showed more pronounced decrease in MW of the second fraction because more polymer chains are in contact with Au NPs compared to **M**₁ with lower Au content. Also a partial oxidative degradation by air oxygen comes into consideration, however, the rate of degradation is negligible, about at least two orders of magnitude lower than that of substituted polyacetylenes¹⁸⁵⁻¹⁸⁷ so that an effect of the polymer degradation on the results of its SEC analysis can be neglected in the case of MEH-PPV.

The molecular weights of purified nanocomposites **R** could not be determined because of their limited solubility, especially at high polymer concentration. It can be explained by crosslinking of the polymer chains which was also observed in the early stages of reaction of $\text{AuCl}_4^-/\text{TOAB}$ complex and the polymer.

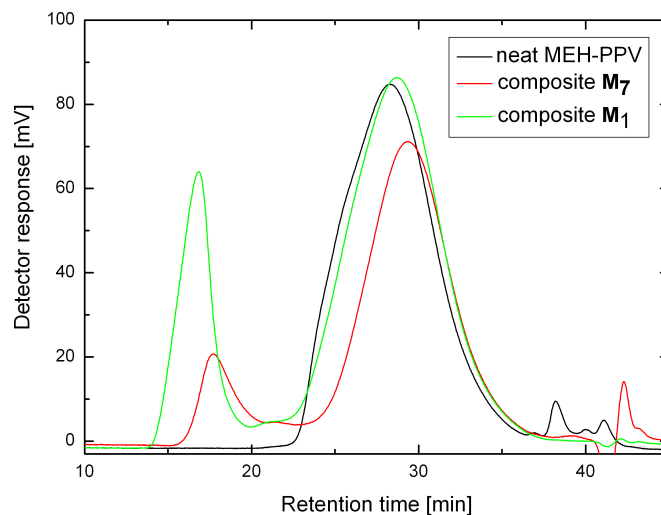


Figure 4.4-11. Chromatograms of composites **M₇** and **M₁** as well as neat MEH-PPV dissolved in DCM.

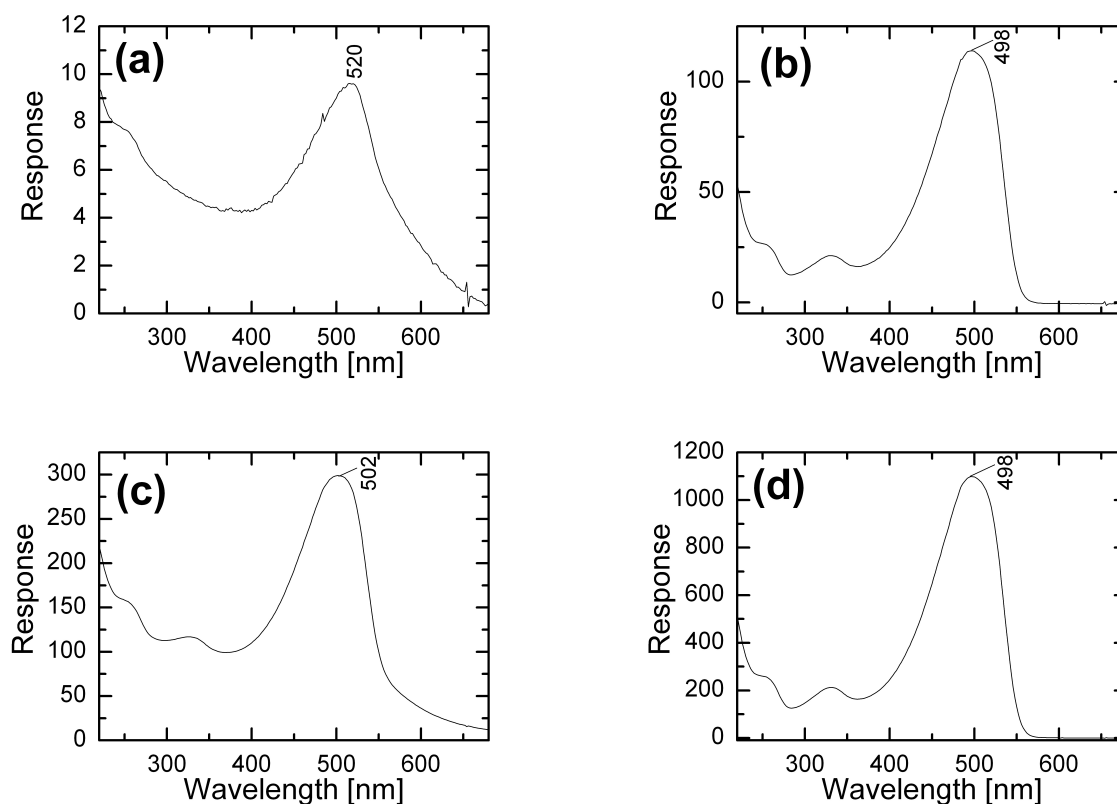


Figure 4.4-12. UV-Vis spectra of composite **M₇** (a,b) and **M₁** (c,d) obtained by HPLC instrument equipped with a diode array UV-Vis detector. The spectra (a,c) and (b,d) correspond to the fractions characterized by short and longer retention time, respectively (see chromatograms in **Figure 4.4-11**).

4.4.6. Mechanism of assembling Au NPs in MEH-PPV matrix

4.4.6.1. Assembling of Au NPs in nanocomposites M

In the parent Au organosol Au NPs are stabilized with TOAB. A quick replacement of TOAB species with a polymer shell upon mixing the Au organosol with a DCM solution of MEH-PPV is improbable because of the strong interaction of Au NPs with Br⁻ anions¹⁷¹. This possibility was examined by the analysis of surface of Au NPs embedded in the polymer matrix using the EDAX method. The EDAX spectrum of as-prepared, i.e. not precipitated composite **M**₇, is shown in Figure 4.4-13a. As can be seen, the surface of Au NPs contains a significant amount of Br atoms, which indicates stabilization of the NPs by the phase-transfer reagent TOAB (the N peak is not seen because of a too low atomic number of nitrogen). The EDAX spectrum of the same nanocomposite after precipitation and washing with methanol (Figure 4.4-13b) shows absence of Br atoms on the surface of Au NPs. This indicates that TOAB has been successfully removed during the precipitation due to its good solubility in methanol and has been replaced by MEH-PPV which took over the role of stabilizer. As mentioned in the discussion of the TEM images (Figure 4.4-2), Au NPs remain almost unchanged in the final, polymer-rich nanocomposite **M**₁ while they undergo aggregation and/or fusion into small compact assemblies in the final, polymer-poor nanocomposite **M**₇.

4.4.6.2. Discussion of Au NPs aggregates formation in nanocomposites R

In this preparative procedure, Au NPs are formed in the presence of polymer which also reacts with the AuCl₄⁻/TOAB complex. This means that Au nanoparticle seeds are formed not only in the domains occupied by neat solvent (polymer-free domains) but also in domains occupied by polymer chains, in which seeds of Au NPs are created on account of the oxidation of polymer. The observation that Au NPs form large compact aggregates in the polymer-rich systems while Au NPs in polymer-poor systems are small (Figure 4.4-3) proves that large or fused NP aggregates grow in the polymer-chain domains while the small NPs in the polymer-free domains.

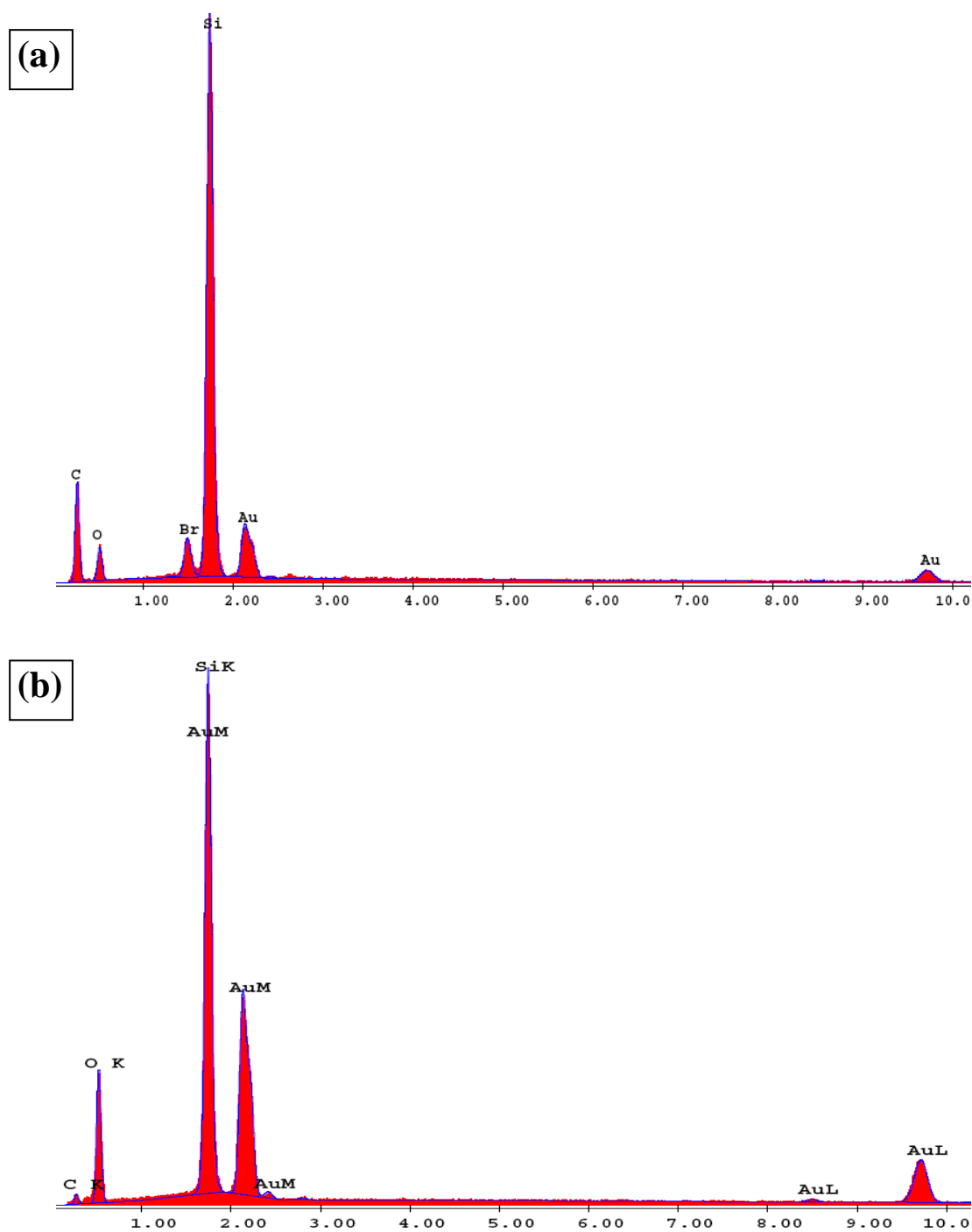


Figure 4.4-13. EDAX spectra of an Au NP aggregate in the M_7 composite determined (a) before the precipitation in methanol and (b) after the precipitation and redissolution in toluene.

4.4.7. Conclusions - Comparison of nanoparticle morphology and optical properties of Au/MEH-PPV and Au/P3OT nanocomposites

Au/ π -conjugated polymer composites type M. Mixing of Au NPs prepared in a separate procedure with a solution of π -conjugated polymer provides nanocomposites type **M** in which the parent polymer remains almost intact as to its molecular weight and structure, and forms a matrix in which Au NPs are distributed depending on the polymer concentration. Au NPs in nanocomposites with P3OT and MEH-PPV having Au/polymer ratio 1/1 are nearly identical with those in the parent Au organosols. The particles are isolated and large aggregates do not form (Figure 4.4-2b and 4.4.-9). At lower polymer concentration, larger Au NPs and small aggregates consisting of several particles were observed in the Au/MEH-PPV composite having Au/polymer ratio 7/1 (Figure 4.4-2a). Extinction spectra of these composites show an intense absorption band of the polymer with a shoulder in the long-wavelength spectral region ascribed to the presence of Au NPs (Figure 4.4-5a and 4.3-6a).

Au/ π -conjugated polymer composites type R. The *in situ* formation of Au NPs in the polymer matrix provides nanocomposites type **R** containing small isolated Au NPs in the composite with P3OT (Figure 4.3-10) while large irregular aggregates are observed in the case of composites with MEH-PPV (Figure 4.4-3d and 4.4-4d) at the same Au/polymer ratios (1/1). With decreasing polymer concentration in Au/MEH-PPV nanocomposites, the fraction of large aggregates decreases and, simultaneously, the fraction of small NPs increases (Figure 4.4-3). At the lowest polymer concentration (composite **R**₇), small Au NPs with mean size of about 5 nm are observed and only a small fraction of large compact aggregates formed by fusion of large Au NPs is present. Different morphology of Au NPs was reported in Au/P3OT composites with varying polymer concentration⁷¹. In particular, nanoparticle aggregates were not observed in Au/P3OT composites containing similar Au/polymer ratios as were used for Au/MEH-PPV composites in this study. Only the presence of larger Au NPs was reported with increasing polymer concentration.

Extinction spectrum of Au/P3OT nanocomposite type **R** resembles the spectrum of the composite type **M** (Figure 4.3-6). On the other hand, the pronounced shift of the absorption maximum of the polymer to shorter wavelengths was observed for Au/MEH-PPV composites (Figure 4.4-5b). Such blue-shift was ascribed to the shortening of conjugation length of the polymer¹⁸¹. It indicates that a partial damage of the molecular structure of the polymer occurs during the composite preparation due to an oxidation of the polymer with the AuCl₄⁻/TOAB

complex. In particular, oxidative degradation and formation of addition charge-transfer complex on the polymer vinylene bonds could lead to the shortening of the polymer conjugation length, as confirmed by spectral and cyclic voltammetry measurements (in chapters 4.4.4. and 4.4.3.3.). To avoid polymer degradation in the preparation of Au/MEH-PPV composites type **R**, it is necessary to add a reductant as soon as possible to minimize the time for which the polymer is in contact with the $\text{AuCl}_4^-/\text{TOAB}$ complex. In contrast to that, polymer degradation was not observed in the preparation of Au/P3OT composites type **R** since the redox potential of P3OT is higher than that of the $\text{AuCl}_4^-/\text{TOAB}$ complex (chapter 4.4.3.3.).

In summary, the obtained results clearly show that the morphology and optical properties of Au NPs in Au/ π -conjugated polymer (P3OT, MEH-PPV) composites are substantially influenced by the type of the polymer and its concentration as well as by the method and conditions used in the composite preparation.

5. Conclusions

Au nanoparticles can be selectively fragmented by high energy nanosecond laser pulses of various wavelengths, depending on the amount of energy absorbed by a nanoparticle. Irradiation of Au hydrosols containing nanoparticles of the mean sizes above 10 nm by laser pulses of 532 and 355 nm wavelengths causes their size-reduction. The mean size of the resulting particles is independent on the initial NP size, but it depends on the wavelength of laser pulses and energy absorbed in the hydrosols.

All particles in the parent sols (sizes above 10 nm) absorb both pulses of 355 and 532 nm wavelengths; however, already formed small Au NPs absorb effectively pulses of 355 nm wavelength, but not 532 nm. Indeed, the hydrosol containing 5 nm particles is fragmented by laser pulses of 355 nm wavelength, but the size-reduction does not occur when the hydrosol is irradiated by laser pulses of 532 nm wavelength. At the latter wavelength the particles have even a tendency to a very little but still observable growth during the fragmentation.

The process of laser-induced fragmentation is cumulative with increasing number of subsequent laser pulses: for longer time of the fragmentation the threshold of laser fluence, for which the shift in SPE maximum position is observable, appears at lower laser fluence.

Fragmentation seems to be a possible pathway to preparation of monodisperse sols of small nanoparticles. These nanoparticles can be useful for formation of 2D-assemblies. However, the small size of nanoparticles prepared by this pathway does not lead to observation of strong plasmonic phenomena.

The morphology and the related optical responses of metal (Ag, Au) NPs in the composites with π -conjugated polymers can be tuned by the choice of the π -conjugated polymer and its concentration as well as by the method and conditions used in the composite preparation.

In Ag/PEEP-I composites, fractal aggregates with their average fractal dimension $D = 1.9 \pm 0.1$ were formed at low polymer concentrations while at high polymer concentrations loosely packed aggregates with large interparticle distances were observed. The novelty of these results lies in the point that fractal aggregates can be formed also by an action of the polymer which is unique for polymeric species. Polymer chains of the used

PEEP-I are thus analogous to several monomeric adsorbates since the charges of the polymer reduce the electrostatic repulsion barrier between adjacent NPs by similar way as monomers.

Localization of polymer chains in hot spots of fractal aggregates was documented by very strong SERS signal which contributes to unusual “inverse” dependence of SERS signal on polymer concentration.

A significant difference between morphology of Au and Ag NPs was found in composites with P3OT. While small spherical Au NPs were homogeneously dispersed in these composites, Ag NPs formed large intergrown aggregates. The difference in nanoparticle morphology was explained by higher adsorption affinity of bromide ions originating from the phase transfer agent used in the composite preparations to Ag NP surface compared with that to Au NP surface.

In situ procedure (interfacial reduction of metal salt with NaBH₄ in the presence of polymer, nanocomposites type **R**) as well as *mixing* procedure (mixing metal organosols with polymer solution, nanocomposites type **M**) can be used for Au/P3OT composites preparation because both procedures lead to the same nanoparticle morphology. In the case of Ag/P3OT composites, it is more suitable to use *in situ* procedure since it provides smaller NP aggregates and small isolated Ag NPs compared to large intergrown aggregates in the composites type **M**.

SERS/SERRS spectral probing of Ag/P3OT composites type **M** and **R** enabled to pinpoint the mutual difference in the polymer structures encountered within each of them, in particular the dominance of the disordered structure in the composite type **R**.

The morphology of Au NPs in composites type **R** with MEH-PPV differs from that in Au/P3OT composites. In particular, large irregular Au nanoparticle aggregates are present in Au/MEH-PPV composite type **R** while small spherical particles are observed in Au/P3OT composites at the same Au/polymer ratio. On the other hand, in the Au/MEH-PPV composite type **M** small spherical Au NPs were observed similarly as in Au/P3OT composites of that type. The difference between the two composites **R** originating from Au NPs and two different π -conjugated polymers was attributed to the effect of the polymer on Au NP growth. Au NPs in composites **R** grow in the presence of particular polymer while pre-prepared Au NPs are employed for composite type **M** preparation.

In the *in situ* preparative procedure of nanocomposite type **R** with MEH-PPV, Au NPs are formed in the presence of the polymer which also reacts with the AuCl₄⁻/TOAB complex.

It is predicted that Au NP seeds are formed not only in the domains occupied by neat solvent (polymer-free domains) but also in domains occupied by polymer chains, in which seeds of Au NPs are created on account of the oxidation of polymer. Large or fused NP aggregates grow in polymer-chain domains while the small NPs in polymer-free domains.

In situ procedure causes a partial damage of the molecular structure of MEH-PPV. It occurs due to polymer oxidation with the $\text{AuCl}_4^-/\text{TOAB}$ complex since the onset of oxidation peak of MEH-PPV is similar to the onset of reduction of Au^{3+} in the complex with TOAB. Therefore, MEH-PPV can be easily oxidized with the $\text{AuCl}_4^-/\text{TOAB}$ complex. On the other hand, P3OT exhibits the stability against oxidation with the complex since the onset of oxidation peak of P3OT is higher than that for MEH-PPV. To avoid polymer degradation in the preparation of Au/MEH-PPV composites type **R**, it is necessary to add a reductant as soon as possible to minimize the time for which the polymer is in contact with the $\text{AuCl}_4^-/\text{TOAB}$ complex.

6. Abbreviations

BDMT	1,4-bis(mercaptomethyl)benzene
cHBDT	disodium 1,4-cyclohexane-bis(dithiocarbamate)
CP(s)	conjugated polymer(s)
CV	cyclic voltamogram
DCM	dichloromethane
DDA	discrete dipole approximation
DLS	dynamic light scattering
DMAAB	1,4-bis(mercaptoacetamido)benzene
DMF	dimethylformamid
DMSO	dimethylsulfoxide
EDAX	energy dispersive analysis of X-rays
EDOT	3,4-ethylenedioxythiophene
EM	electromagnetic
FDTD	finite difference time domain methods
FRET	fluorescence (Förster) resonance energy transfer
LSPR	localized surface plasmon resonance
MEH-PPV	poly[2-methoxy-5-(2-ethylhexyloxy)-1,4-phenylenevinylene]
MLWA	modified long wavelength approximation
NP(s)	nanoparticle(s)
NC(s)	nanocomposite(s)
(O)FET	(organic) field effect transistors
(O)LEDs	(organic) light emitting displays
OPV	oligo(<i>p</i> -phenylene vinylene)
PBDT	disodium 1,4-phenylene-bis(dithiocarbamate)
PEDOT	poly(3,4-ethylenedioxythiophene)
PEEP-I	poly(N-ethyl-2-ethynylpyridinium iodide)
PT(s)	polythiophene(s)
PVP3T	terthiophene-functionalized poly(4-vinylpyridine)
P3OT	poly(3-octylthiophene-2,5-diyl)
P2EPH	poly(2-pyridinium hydrochloride-2-pyridylacetylene)
SEC	size-exclusion chromatography

SE(R)RS	surface enhanced (resonance) Raman scattering
SP(s)	surface plasmon(s)
SPE	surface plasmon extinction
SPPs	surface plasmon polaritons
TBAPC	tetrabutylammonium perchlorate
TEM	transmission electron microscopy
TDAB	tetradodecylammonium bromide
THF	tetrahydrofuran
TOAB	tetraoctylammonium bromide
2(3)-D	2(3)-dimensional

Notations of sols and nanocomposites

Au1	Au nanoparticle hydrosol containing 5 nm particles in diameter
Au2	Au nanoparticle hydrosol containing 11 nm particles in diameter
Au3	Au nanoparticle hydrosol containing 35 nm particles in diameter
Au4	Au nanoparticle hydrosol containing 104 nm particles in diameter
Ag/PEEP-I	nanocomposite system consisting of Ag NPs and π -conjugated PEEP-I
Ag/P3OT	nanocomposite system consisting of Ag NPs and P3OT
Au/P3OT	nanocomposite system consisting of Au NPs and P3OT
Au/MEH-PPV	nanocomposite system consisting of Au NPs and MEH-PPV
composite type M	prepared by mixing nanoparticle organosol with polymer solution
composite type R	prepared by <i>in situ</i> reduction of metal salt with NaBH ₄ in the presence of a polymer
AuCl ₄ ⁻ /TOAB complex	Au ³⁺ ions transferred into the organic phase (toluene, DCM) due to TOAB

7. References

1. C. F. Bohren and D. F. Huffman, *Absorption and Scattering of Light by Small Particles*, Wiley, New York, 1983.
2. P. V. Kamat, *J. Phys. Chem. B*, 2002, **106**, 7729-7744.
3. S. Link and M. A. El-Sayed, *J. Phys. Chem. B*, 1999, **103**, 8410-8426.
4. K. L. Kelly, E. Coronado, L. L. Zhao and G. C. Schatz, *J. Phys. Chem. B*, 2003, **107**, 668-677.
5. Z. S. Pillai and P. V. Kamat, *J. Phys. Chem. B*, 2004, **108**, 945-951.
6. M. E. Stewart, C. R. Anderton, L. B. Thompson, J. Maria, S. K. Gray, J. A. Rogers and R. G. Nuzzo, *Chem. Rev.*, 2008, **108**, 494-521.
7. A. Wei, *Plasmonic Nanomaterials*, Kluwer Academic/Plenum Publishers, New York, 2004.
8. K. A. Willets and R. P. Van Duyne, *Ann. Rev. Phys. Chem.*, 2007, **58**, 267-297.
9. J. A. Creighton and D. G. Eadon, *J. Chem. Soc. Faraday Trans.*, 1991, **87**, 3881-3891.
10. S. Link and M. A. El-Sayed, *J. Phys. Chem. B*, 1999, **103**, 4212-4217.
11. G. Mie, *Ann. Phys.*, 1908, **25**, 377.
12. C. Burda, X. Chen, R. Narayanan and M. A. El-Sayed, *Chem. Rev.*, 2005, **105**, 1025-1102.
13. E. Hao, G. C. Schatz and J. T. Hupp, *J. Fluoresc.*, 2004, **14**, 331-341.
14. G. C. Schatz, *J. Mol. Struct.*, 2001, **573**, 73-80.
15. I. O. Sosa, C. Noguez and R. G. Barrera, *J. Phys. Chem. B*, 2003, **107**, 6269-6275.
16. E. Hao, S. Li, R. C. Bailey, S. Zou, G. C. Schatz and J. T. Hupp, *J. Phys. Chem. B*, 2004, **108**, 1224-1229.
17. S. Link, M. B. Mohamed and M. A. El-Sayed, *J. Phys. Chem. B*, 1999, **103**, 3073-3077.
18. K. G. Thomas, J. Zajicek and P. V. Kamat, *Langmuir*, 2002, **18**, 3722-3727.
19. C. L. Haynes, A. D. McFarland, L. L. Zhao, R. P. Van Duyne, G. C. Schatz, L. Gunnarsson, J. Prikulis, B. Kasemo and M. Käll, *J. Phys. Chem. B*, 2003, **107**, 7337-7342.
20. M. D. Malinsky, K. L. Kelly, G. C. Schatz and R. P. Van Duyne, *J. Phys. Chem. B*, 2001, **105**, 2343-2350.
21. T. R. Jensen, G. C. Schatz and R. P. Van Duyne, *J. Phys. Chem. B*, 1999, **103**, 2394-2401.
22. L. L. Zhao, K. L. Kelly and G. C. Schatz, *J. Phys. Chem. B*, 2003, **107**, 7343-7350.
23. A. J. Haes, S. Zou, G. C. Schatz and R. P. Van Duyne, *J. Phys. Chem. B*, 2004, **108**, 109-116.
24. M. Moskovits, *Rev. Mod. Phys.*, 1985, **57**, 783-826.
25. D. A. Weitz, M. Y. Lin and C. J. Sandroff, *Surf. Sci.*, 1985, **158**, 147-164.
26. V. A. Markel, V. M. Shalaev, E. B. Stechel, W. Kim and R. L. Armstrong, *Phys. Rev. B*, 1996, **53**, 2425-2436.
27. B. D. Gates, Q. Xu, M. Stewart, D. Ryan, C. G. Willson and G. M. Whitesides, *Chem. Rev.*, 2005, **105**, 1171-1196.
28. J. Turkevitch, P. C. Stevenson and J. Hillier, *Discuss. Faraday Soc.*, 1951, **11**, 55-75.
29. B. Vlčková, P. Matějka, J. Šimonová, K. Čermáková, P. Pančoška and V. Baumruk, *J. Phys. Chem.*, 1993, **97**, 9719-9729.
30. B. Wiley, T. Herricks, Y. Sun and Y. Xia, *Nano Lett.*, 2004, **4**, 1733-1739.
31. I. Srnova-Sloufova, B. Vlckova and Z. Bastl, *Langmuir*, 2004, **20**, 3407-3415.

32. J. H. Youk, M. K. Park, J. Locklin, R. Advincula, J. Yang and J. Mays, *Langmuir*, 2002, **18**, 2455-2458.
33. C. J. Huang, P. H. Chiu, Y. H. Wang, C. F. Yang and S. W. Feng, *J. Colloid Interface Sci.*, 2007, **306**, 56-65.
34. Y. Y. Yu, S. S. Chang, C. L. Lee and C. R. C. Wang, *J. Phys. Chem. B*, 1997, **101**, 6661-6664.
35. F. Kim, J. H. Song and P. Yang, *J. Am. Chem. Soc.*, 2002, **124**, 14316-14317.
36. J. Zhu, Y. Shen, A. Xie, L. Qiu, Q. Zhang and S. Zhang, *J. Phys. Chem. C*, 2007, **111**, 7629-7633.
37. A. Sánchez-Iglesias, I. Pastoriza-Santos, J. Pérez-Juste, B. Rodríguez-González, F. J. G. de Abajo and L. M. Liz-Marzán, *Adv. Mater.*, 2006, **18**, 2529-2534.
38. C. H. Su, P. L. Wu and C. S. Yeh, *J. Phys. Chem. B*, 2003, **107**, 14240-14243.
39. M.-C. Daniel and D. Astruc, *Chem. Rev.*, 2004, **104**, 293-346.
40. R. B. Grubbs, *Polym. Rev.*, 2007, **47**, 197-215.
41. M. Brust, M. Walker, D. Bethell, D. J. Schiffrin and R. Whyman, *J. Chem. Soc., Chem. Commun.*, 1994, 801-802.
42. N. R. Jana and X. Peng, *J. Am. Chem. Soc.*, 2003, **125**, 14280-14281.
43. L. Lu, A. Kobayashi, K. Tawa and Y. Ozaki, *Chem. Mater.*, 2006, **18**, 4894-4901.
44. H. Yuan, W. Ma, C. Chen, J. Zhao and J. Liu, *Chem. Mater.*, 2007, **19**, 1592-1600.
45. N. R. Jana, L. Gearheart and C. J. Murphy, *Adv. Mater.*, 2001, **13**, 1389-1393.
46. A. Fojtik and A. Henglein, *Ber. Buns. Gesellsch. Phys. Chem. Chem. Phys.*, 1993, **97**, 252-254.
47. P. Smejkal, K. Siskova, B. Vlckova, J. Pflieger, I. Sloufova, M. Slouf and P. Mojzes, *Spectrochim. Acta A*, 2003, **59**, 2321-2329.
48. A. Takami, H. Kurita and S. Koda, *J. Phys. Chem. B*, 1999, **103**, 1226-1232.
49. P. V. Kamat, M. Flumiani and G. V. Hartland, *J. Phys. Chem. B*, 1998, **102**, 3123-3128.
50. S. Inasawa, M. Sugiyama and Y. Yamaguchi, *J. Phys. Chem. B*, 2005, **109**, 9404-9410.
51. S. Inasawa, M. Sugiyama, S. Noda and Y. Yamaguchi, *J. Phys. Chem. B*, 2006, **110**, 3114-3119.
52. M. Kawasaki and M. Hori, *J. Phys. Chem. B*, 2003, **107**, 6750-6765.
53. S. Link, C. Burda, B. Nikoobakht and M. A. El-Sayed, *J. Phys. Chem. B*, 2000, **104**, 6152-6163.
54. P. Smejkal, J. Pflieger, K. Siskova, B. Vlckova, O. Dammer and M. Slouf, *Appl. Phys. A*, 2004, **79**, 1307-1309.
55. Z. Peng, T. Walther and K. Kleinermanns, *J. Phys. Chem. B*, 2005, **109**, 15735-15740.
56. H. Fujiwara, S. Yanagida and P. V. Kamat, *J. Phys. Chem. B*, 1999, **103**, 2589-2591.
57. S. Link, C. Burda, B. Nikoobakht and M. A. El-Sayed, *Chem. Phys. Lett.*, 1999, **315**, 12-18.
58. S. S. Chang, C. W. Shih, C. D. Chen, W. C. Lai and C. R. C. Wang, *Langmuir*, 1999, **15**, 701-709.
59. F. Mafuné, J. Kohno, Y. Takeda and T. Kondow, *J. Phys. Chem. B*, 2003, **107**, 12589-12596.
60. K. Šišková, PhD Thesis, Charles University, Prague, 2007.
61. S. Link, Z. L. Wang and M. A. El-Sayed, *J. Phys. Chem. B*, 2000, **104**, 7867-7870.
62. P. W. J. G. Wijnen, T. P. M. Beelen, K. P. J. Rummens, H. C. P. L. Saeijs and R. A. van Santen, *J. Appl. Cryst.*, 1991, **24**, 759-764.
63. I. Sloufova, K. Siskova, B. Vlckova and J. Stepanek, *Phys. Chem. Chem. Phys.*, 2008, **10**, 2233-2242.

64. M. Michl, B. Vlckova, I. Sloufova and P. Mojzes, *Can. J. Anal. Sci. Spectrosc.*, 2003, **48**, 46-54.
65. J. Pyun, *Polym. Rev.*, 2007, **47**, 231-263.
66. C. M. Homenick, G. Lawson and A. Adronov, *Polym. Rev.*, 2007, **47**, 265-290.
67. P. K. Sudeep and T. Emrick, *Polym. Rev.*, 2007, **47**, 155-163.
68. A. J. Crosby and J. Y. Lee, *Polym. Rev.*, 2007, **47**, 217-229.
69. L. A. Goettler, K. Y. Lee and H. Thakkar, *Polym. Rev.*, 2007, **47**, 291-317.
70. T. A. Skotheim and J. R. Reynolds, *Conjugated Polymers*, CRC Press, Taylor & Francis Group, Boca Raton, 2007.
71. L. Zhai and R. D. McCullough, *J. Mater. Chem.*, 2004, **14**, 141-143.
72. J. H. Youk, J. Locklin, C. Xia, M. K. Park and R. Advincula, *Langmuir*, 2001, **17**, 4681-4683.
73. D. Patton, J. Locklin, M. Meredith, Y. Xin and R. Advincula, *Chem. Mater.*, 2004, **16**, 5063-5070.
74. X. Li, Y. Li, Y. Tan, C. Yang and Y. Li, *J. Phys. Chem. B*, 2004, **108**, 5192-5199.
75. X. Li, Y. Li, C. Yang and Y. Li, *Langmuir*, 2004, **20**, 3734-3739.
76. S. S. Kumar, C. S. Kumar, J. Mathiyarasu and K. L. Phani, *Langmuir*, 2007, **23**, 3401-3408.
77. Y. Zhou, H. Itoh, T. Uemura, K. Naka and Y. Chujo, *Langmuir*, 2002, **18**, 277-283.
78. Y. Zhou, H. Itoh, T. Uemura, K. Naka and Y. Chujo, *Chem. Commun.*, 2001, 613-614.
79. M. A. Breimer, G. Yevgeny, S. Sy and O. A. Sadik, *Nano Lett.*, 2001, **1**, 305-308.
80. H. S. Zhou, T. Wada, H. Sasabe and H. Komiyama, *Synth. Met.*, 1996, **81**, 129-132.
81. D. W. Chang and L. Dai, *Nanotechnology*, 2007, **18**, 365605/365601-365605/365607.
82. M. M. Oliveira, D. Zanchet, D. Ugarte and A. J. G. Zarbin, *Prog. Colloid Polym. Sci.*, 2004, **128**, 126-130.
83. M. M. Oliveira, E. G. Castro, C. D. Canestraro, D. Zanchet, D. Ugarte, L. S. Roman and A. J. G. Zarbin, *J. Phys. Chem. B*, 2006, **110**, 17063-17069.
84. Z. Zhang, F. Wang, F. Chen and G. Shi, *Mater. Lett.*, 2006, **60**, 1039-1042.
85. S. M. Marinakos, L. C. Brousseau III, A. Jones and D. L. Feldheim, *Chem. Mater.*, 1998, **10**, 1214-1219.
86. L. C. Brousseau III, J. P. Novak, S. M. Marinakos and D. L. Feldheim, *Adv. Mater.*, 1999, **11**, 447-449.
87. J. P. Novak and D. L. Feldheim, *J. Am. Chem. Soc.*, 2000, **122**, 3979-3980.
88. M. J. Hostetler, A. C. Templeton and R. W. Murray, *Langmuir*, 1999, **15**, 3782-3789.
89. J. van Herrikhuyzen, R. A. J. Janssen, E. W. Meijer, S. C. J. Meskers and A. P. H. J. Schenning, *J. Am. Chem. Soc.*, 2006, **128**, 686-687.
90. K. M. Kost, D. E. Bartak, B. Kazee and T. Kuwana, *Anal. Chem.*, 1988, **60**, 2379-2384.
91. Z. Peng, E. Wang and S. Dong, *Electrochem. Commun.*, 2002, **4**, 210-213.
92. B. C. Sih, A. Teichert and M. O. Wolf, *Chem. Mater.*, 2004, **16**, 2712-2718.
93. D. W. Hatchett, M. Josowicz, J. Janata and D. R. Baer, *Chem. Mater.*, 1999, **11**, 2989-2994.
94. J. M. Wessels, H. G. Nothofer, W. E. Ford, F. Wrochem, F. Scholz, T. Vossmeier, A. Schroedter, H. Weller and A. Yasuda, *J. Am. Chem. Soc.*, 2004, **126**, 3349-3356.
95. H. S. Kim, S. J. Lee, N. H. Kim, J. K. Yoon, H. K. Park and K. Kim, *Langmuir*, 2003, **19**, 6701-6710.
96. J. M. Tour, L. Jones, D. L. Pearson, J. J. S. Lamba, T. P. Burgin, G. M. Whitesides, D. L. Allara, A. N. Parikh and S. V. Atre, *J. Am. Chem. Soc.*, 1995, **117**, 9529-9534.
97. G. Zotti, B. Vercelli, M. Battagliarin, A. Berlin, V. Hernandez and J. T. L. Navarrete, *J. Phys. Chem. C*, 2007, **111**, 5886-5892.

98. H. S. Zhou, T. Wada, H. Sasabe and H. Komiyama, *Appl. Phys. Lett.*, 1996, **68**, 1288-1290.
99. L. A. Cury, L. O. Ladeira and A. Righi, *Synth. Met.*, 2003, **139**, 283-286.
100. L. Armelao, D. Barreca, G. Bottaro, A. Gasparotto, E. Tondello, M. Ferroni and S. Polizzi, *Chem. Mater.*, 2004, **16**, 3331-3338.
101. N. K. Chaki, M. Aslam, T. G. Gopakumar, J. Sharma, R. Pasricha, I. S. Mulla and K. Vijayamohanan, *J. Phys. Chem. B*, 2003, **107**, 13567-13574.
102. J. P. Bourgoin, C. Kergueris, E. Lefevre and S. Palacina, *Thin Solid Films*, 1998, **327-329**, 515-519.
103. R. H. Terrill, T. A. Postlethwaite, C. H. Chen, C. D. Poon, A. Terzis, A. Chen, J. E. Hutchison, M. R. Clark, G. Wignall, J. D. Londono, R. Superfine, M. Falvo, C. S. Johnson, E. T. Samulski and R. W. Murray, *J. Am. Chem. Soc.*, 1995, **117**, 12537-12548.
104. V. Ruiz, P. G. Nicholson, S. Jollands, P. A. Thomas, J. V. Macpherson and P. R. Unwin, *J. Phys. Chem. B*, 2005, **109**, 19335-19344.
105. W. P. Wuelfing, S. J. Green, J. J. Pietron, D. E. Cliffler and R. W. Murray, *J. Am. Chem. Soc.*, 2000, **122**, 11465-11472.
106. V. Torma, O. Vidoni, U. Simon and G. Schmid, *Eur. J. Inorg. Chem.*, 2003, 1121-1127.
107. T. K. Sarma, D. Chowdhury, A. Paul and A. Chattopadhyay, *Chem. Commun.*, 2002, 1048-1049.
108. T. K. Sarma and A. Chattopadhyay, *J. Phys. Chem. A*, 2004, **108**, 7837-7842.
109. M. Moskovits, *J. Chem. Phys.*, 1978, **69**, 4159-4161.
110. D. L. Jeanmaire and R. P. van Duyne, *J. Electroanal. Chem.*, 1977, **84**, 1-20.
111. K. Kneipp, Y. Wang, H. Kneipp, L. T. Perelman, I. Itzkan, R. Dasari and M. S. Feld, *Phys. Rev. Lett.*, 1997, **78**, 1667-1670.
112. M. Käll, H. Xu and P. Johansson, *J. Raman Spectrosc.*, 2005, **36**, 510-514.
113. P. Johansson, H. Xu and M. Käll, *Phys. Rev. B*, 2005, **72**, 035427.
114. J. Xue, S. Uchida, B. P. Rand and S. R. Forrest, *Appl. Phys. Lett.*, 2004, **85**, 5757.
115. M. Moskovits, L. L. Tay, J. Yang and T. Haslett, *Top. Appl. Phys.*, 2002, **82**, 215-226.
116. M. Moskovits, *J. Raman Spectrosc.*, 2005, **36**, 485-496.
117. B. Vlckova, I. Pavel, M. Sladkova, K. Siskova and M. Slouf, *J. Mol. Struct.*, 2007, **834-836**, 42-47.
118. D. A. Weitz, S. Garoff, J. I. Gersten and A. Nitzan, *J. Chem. Phys.*, 1983, **78**, 5324-5338.
119. M. Prochazka, B. Vlckova, J. Stepanek and P. Y. Turpin, *Langmuir*, 2005, **21**, 2956-2962.
120. A. Campion and P. Kambhampati, *Chem. Soc. Rev.*, 1998, **27**, 241-250.
121. I. Srnova-Sloufova, B. Vlckova, T. L. Snoeck, D. J. Stufkens and P. Matejka, *Inorg. Chem.*, 2000, **39**, 3551-3559.
122. K. Liu, S. Y. Shen and H. J. Xu, *Acta Phys.-Chim. Sin.*, 2000, **16**, 1103-1109.
123. S. Lefrant, I. Baltog, M. Lamy de la Chapelle, M. Baibarac, G. Louarn, C. Journet and P. Bernier, *Synth. Met.*, 1999, **100**, 13-27.
124. E. A. Bazzaoui, J. Aubard, N. Felidj, G. Laurent and G. Levi, *J. Raman Spectrosc.*, 2005, **36**, 817-823.
125. K. Mukherjee, D. Bhattacharjee and T. N. Misra, *J. Colloid Interface Sci.*, 1999, **213**, 46-52.
126. E. A. Bazzaoui, M. Bazzaoui, J. Aubard, J. S. Lomas, N. Felidj and G. Levi, *Synth. Met.*, 2001, **123**, 299-309.

127. R. P. Millen, M. L. A. Temperini, D. L. A. de Faria and D. N. Batchelder, *J. Raman Spectrosc.*, 1999, **30**, 1027-1033.
128. R. P. Millen, D. L. A. de Faria and M. L. A. Temperini, *Synth. Met.*, 2006, **156**, 459-465.
129. E. M. Goldys, A. Barbett, F. Xie, K. Drozdowicz-Tomsia, I. Gryczynski, E. G. Matveeva, Z. Gryczynski and T. Shtoyko, *Appl. Phys. A: Mater. Sci. Process.*, 2007, **89**, 265-271.
130. K. Aslan, M. Wu, J. R. Lakowicz and C. D. Geddes, *J. Fluoresc.*, 2007, **17**, 127-131.
131. J. R. Lakowicz, C. D. Geddes, I. Gryczynski, J. Malicka, Z. Gryczynski, K. Aslan, J. Lukomska, E. Matveeva, J. Zhang, R. Badugu and J. Huang, *J. Fluoresc.*, 2004, **14**, 425-441.
132. J. R. Lakowicz, *Plasmonics*, 2006, **1**, 5-33.
133. T. Uemura, M. Furumoto, T. Nakano, M. Akai-Kasaya, A. Saito, M. Aono and Y. Kuwahara, *Chem. Phys. Lett.*, 2007, **448**, 232-246.
134. S. K. Gray, *Plasmonics*, 2007, **2**, 143-146.
135. B. I. Ipe, K. G. Thomas, S. Barazzouk, S. Hotchandani and P. V. Kamat, *J. Phys. Chem. B*, 2002, **106**, 18-21.
136. B. I. Ipe and K. G. Thomas, *J. Phys. Chem. B*, 2004, **108**, 13265-13272.
137. S. Barazzouk, P. V. Kamat and S. Hotchandani, *J. Phys. Chem. B*, 2005, **109**, 716-723.
138. P. V. Kamat, S. Barazzouk and S. Hotchandani, *Angew. Chem. Int. Ed.*, 2002, **41**, 2764-2767.
139. B. N. J. Persson and N. D. Lang, *Phys. Rev. B*, 1982, **26**, 5409-5415.
140. J. Gersten and A. Nitzan, *J. Chem. Phys.*, 1981, **75**, 1139-1152.
141. R. Ruppin, *J. Chem. Phys.*, 1982, **76**, 1681-1684.
142. C. S. Yun, A. Javier, T. Jennings, M. Fisher, S. Hira, S. Peterson, B. Hopkins, N. O. Reich and G. F. Strouse, *J. Am. Chem. Soc.*, 2005, **127**, 3115-3119.
143. P. V. Kamat, *J. Phys. Chem. C*, 2007, **111**, 2834.
144. S. Saini, S. Bhowmick, V. B. Shenoy and B. Bagchi, *J. Photochem. Photobiol., A*, 2007, **190**, 335-341.
145. S. Chen and R. W. Murray, *J. Phys. Chem. B*, 1999, **103**, 9996-10000.
146. C. Fan, S. Wang, J. W. Hong, G. C. Bazan, K. W. Plaxco and A. J. Heeger, *Proc. Natl. Acad. Sci. U. S. A.*, 2003, **100**, 6297-6301.
147. C. Wu, C. Szymanski and J. McNeill, *Langmuir*, 2006, **22**, 2956-2960.
148. P. G. Zhou and A. Blumstein, *Polymer*, 1996, **37**, 1477-1485.
149. S. Subramanyan, A. Blumstein and K. P. Li, *Macromolecules*, 1992, **25**, 2065-2069.
150. A. M. Ahern and R. L. Garrell, *Anal. Chem.*, 1987, **59**, 2813-2816.
151. O. Siiman and H. Feilchenfeld, *J. Phys. Chem.*, 1988, **92**, 453-464.
152. U. Kreibig and M. Vollmer, *Optical Properties of Metal Clusters*, Springer, Berlin, 1995.
153. S. Inasawa, M. Sugiyama and Y. Yamaguchi, *J. Phys. Chem. B*, 2005, **109**, 3104-3111.
154. S. Link and M. A. El-Sayed, *J. Chem. Phys.*, 2001, **114**, 2362-2368.
155. S. Inasawa, M. Sugiyama and S. Koda, *Jpn. J. Appl. Phys.*, 2003, **42**, 6705-6712.
156. K. Koga, T. Ikeshoji and K. Sugawara, *Phys. Rev. Lett.*, 2004, **92**, 115507.
157. M. Hu and G. V. Hartland, *J. Phys. Chem. B*, 2002, **106**, 7029-7033.
158. S. Subramanyam and A. Blumstein, *Macromolecules*, 1991, **24**, 2668-2674.
159. K. Solecká, Charles University, Prague, 1997.
160. J. J. Storhoff, A. A. Lazarides, R. C. Mucic, C. A. Mirkin, R. L. Letsinger and G. C. Schatz, *J. Am. Chem. Soc.*, 2000, **122**, 4640-4650.

161. N. G. Khlebtsov, *J. Quant. Spectrosc. Radiat. Transfer*, 2004, **89**, 143-153.
162. R. P. Millen, D. L. A. de Faria and M. L. A. Temperini, *Vib. Spectrosc.*, 2001, **27**, 89-96.
163. M. I. Stockman, V. M. Shalaev, M. Moskovits, R. Botet and T. F. George, *Phys. Rev. B*, 1992, **46**, 2821-2830.
164. D. P. Tsai, J. Kovacs, Z. Wang, M. Moskovits, V. M. Shalaev, J. S. Suh and R. Botet, *Phys. Rev. Lett.*, 1994, **72**, 4149-4152.
165. A. Parfenov, I. Gryczynski, J. Malicka, C. D. Geddes and J. R. Lakowicz, *J. Phys. Chem. B*, 2003, **107**, 8829-8833.
166. E. Dulkeith, M. Ringle, T. A. Klar, J. Feldmann, A. Munoz Javier and W. J. Parak, *Nano Lett.*, 2005, **5**, 585-589.
167. P. Anger, P. Bharadwaj and L. Novotny, *Phys. Rev. Lett.*, 2006, **96**, 113002.
168. M. M. Oliveira, D. Ugarte, D. Zanchet and A. J. G. Zarbina, *J. Colloid Interface Sci.*, 2005, **292**, 429-435.
169. G. Li, Y. Yao, H. Yang, V. Shrotriya, G. Yang and Y. Yang, *Adv. Funct. Mater.*, 2007, **17**, 1636-1644.
170. K. V. Sarathy, K. S. Narayan, J. Kim and J. O. White, *Chem. Phys. Lett.*, 2000, **318**, 543-548.
171. J. Fink, C. J. Kiely, D. Bethell and D. J. Schiffrin, *Chem. Mater.*, 1998, **10**, 922-926.
172. S. Sánchez-Cortés, J. V. García-Ramos, G. Morcillo and A. Tinti, *J. Colloid Interface Sci.*, 1995, **175**, 358-368.
173. M. Baibarac, M. Lapkowski, A. Pron, S. Lefrant and I. Baltog, *J. Raman Spectrosc.*, 1998, **29**, 825-832.
174. E. A. Bazzaoui, G. Levi, S. Aeiya, J. Aubard, J. P. Marsault and P. C. Lacaze, *J. Phys. Chem.*, 1995, **99**, 6628-6634.
175. J. M. Verilhac, G. LeBlevenec, D. Djurado, F. Rieutord, M. Chouiki, J. P. Travers and A. Pron, *Synth. Met.*, 2006, **156**, 815-823.
176. T. Danno, J. Kurti and H. Kuzmani, *Phys. Rev. B*, 1991, **43**, 4809-4819.
177. K. Iwasaki, H. Fujimoto and S. Matsuzaki, *Synth. Met.*, 1994, **63**, 101-108.
178. M. Trznadel, M. Zagorska, M. Lapkowski, G. Louarn, S. Lefrant and A. Pron, *J. Chem. Soc., Faraday Trans.*, 1996, **92**, 1387-1393.
179. S. G. C., *J. Mol. Struct.*, 2001, **573**, 73-80.
180. A. A. Lazarides, K. Lance Kelly, T. R. Jensen and G. C. Schatz, *J. Mol. Struct.*, 2000, **529**, 59-63.
181. G. Padmanaban and S. Ramakrishnan, *J. Am. Chem. Soc.*, 2000, **122**, 2244-2251.
182. O. Dammer, B. Vlčková, K. Podhájecká, M. Procházka and J. Pflieger, *Macromol. Symp.*, 2008, **268**, 91-95.
183. L. I. Elding and A.-B. Gröning, *Acta Chem. Scan. A*, 1978, **32**, 867-877.
184. J. Cornil, D. Beljonne, R. H. Friend and J. L. Bredas, *Chem. Phys. Lett.*, 1994, **223**, 82-88.
185. J. Vohlídal, D. Rádová, M. Pacovská and J. Sedláček, *Collect. Czech. Chem. Commun.*, 1993, **58**, 2651-2662.
186. J. Vohlídal, Z. Kabátek, M. Pacovská, J. Sedláček and Z. Grubišic-Gallot, *Collect. Czech. Chem. Commun.*, 1996, **61**, 120-125.
187. J. Sedláček, M. Pacovská, J. Vohlídal, Z. Grubišic-Gallot and M. Žigon, *Macromol. Chem. Phys.*, 1995, **166**, 1705-1712.
188. J. C. Scott, J. K. Kaufman, P. J. Brock, R. Di Pietro, J. Salem and J. A. Goitia, *J. Appl. Phys.*, 1996, **79**, 2745-2751.
189. H. Becker, H. Spreitzer, K. Ibrom and W. Kreuder, *Macromolecules*, 1999, **32**, 4925-4932.

190. M. Atreya, S. Lia, E. T. Kang, K. G. Neoh, Z. H. Ma, K. L. Tan and W. Huang, *Polym. Degrad. Stab.*, 1999, **65**, 287-296.
191. I. Orion, J. P. Buisson and S. Lefrant, *Phys. Rev. B*, 1998, **57**, 7050-7065.
192. E. Mulazzi, A. Ripamonti, J. Wery, B. Dulieu and S. Lefrant, *Phys. Rev. B*, 1999, **60**, 16519-16525.
193. T. P. Nguyen, V. H. Tran, P. Destruel and D. Oelkrug, *Synth. Met.*, 1999, **101**, 633-634.
194. G. A. M. Sáfar, F. A. C. Oliveira, L. A. Cury, A. Righi, P. L. M. Barbosa, P. Dieudonné and F. S. Lameiras, *J. Appl. Polym. Sci.*, 2006, **102**, 5620-5626.

8. Publications

Results presented in this thesis have been published in the following journals:

1. O. Dammer, B. Vlčková, M. Šlouf, J. Pflieger: Interaction of high-power laser pulses with monodisperse gold particles, *Mat. Sci. Eng. B* 2007, **140**, 138 – 146.
2. P. Šmejkal, J. Pflieger, B. Vlčková and O. Dammer: Laser ablation of silver in aqueous ambient: effect of laser pulse wavelength and energy on efficiency of the process, *J. Phys. Conf. Ser.* 2007, **59**, 185 – 188.
3. O. Dammer, B. Vlčková, K. Podhájecká, M. Procházka and J. Pflieger: Polymer Composites with Plasmonic Metal Nanoparticles, *Macromol. Symp.*, 2008, **268**, 91 – 95.
4. K. Podhájecká, O. Dammer and J. Pflieger: Electrical Conductivity of Poly(3-octylthiophene)/Au Nanocomposites, *Macromol. Symp.*, 2008, **268**, 72 – 76.
5. O. Dammer, B. Vlčková, M. Procházka, D. Bondarev, J. Vohlídal and J. Pflieger: Effect of preparation procedure on the structure, morphology, and optical properties of nanocomposites of poly[2-methoxy-5-(2-ethylhexyloxy)-1,4-phenylenevinylene] with gold nanoparticles, *Mat. Chem. Phys.*, 2009, **115**, 352 – 360.
6. O. Dammer, B. Vlčková, M. Procházka, J. Sedláček, J. Vohlídal and J. Pflieger: Morphology and optical responses of SERS active π -conjugated poly(N-ethyl-2-ethynylpyridinium iodide)/Ag nanocomposite system, *Phys. Chem. Chem. Phys.*, 2009, **11**, 5455 – 5461.

Acknowledgment

At first, I would like to thank my tutors *Prof. RNDr. Blanka Vlčková, CSc* and *RNDr. Jiří Pfleger, CSc.* for their personal supervising and constant support during my PhD thesis.

Furthermore, I would like to express my gratitude to following people:

Mgr. Klára Podhájecká, Ph.D. for her help and advices during all my studies,

Doc. RNDr. Marek Procházka, Ph.D. for lending me during measurements of Raman spectra and worthwhile discussions,

Jiřina Hromádková for measurements of TEM, SEM images and EDAX analysis,

Mgr. Ivan Němec, Ph.D. for his help with measurement of FT-Raman spectra,

Mgr. Dmitrij Bondarev for measurement of size-exclusion chromatography,

Prof. RNDr. Jiří Vohlídal, CSc. for useful consultations and help with elucidation of polymer degradation,

RNDr. Jan Sedláček, Dr. for providing of poly(N-ethyl-2-ethynylpyridinium iodide), PEEP-I,

Doc. RNDr. Čestmír Koňák, DrSc. for enabling of DLS measurement.

I thank my family for support during my studies.